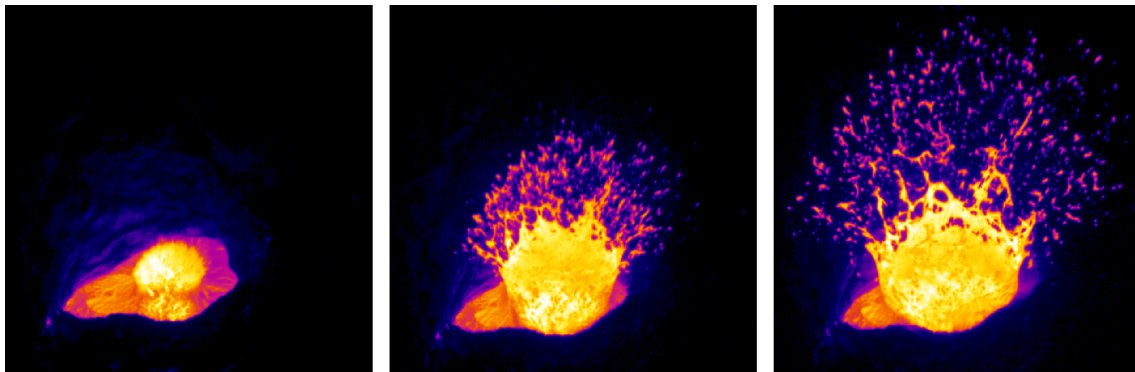


Monitoring Erebus Volcano's Active Lava Lake; Tools, Techniques and Observations.

Nial John Peters
St Catharine's College

April 2014



A dissertation presented for the degree of Doctor of Philosophy



UNIVERSITY OF
CAMBRIDGE



Aaron, this is all your fault...

Cover Image: A sequence of false-colour images captured with a thermal infra-red camera in December 2010 showing a large gas bubble arriving in the Erebus lava lake.

Declaration

This dissertation is the result of my own work and includes nothing which is the outcome of work done in collaboration except where specifically indicated in the text. I confirm that it does not exceed the word limit required by the degree committee of Earth Sciences and Geography and does not contain work that has been submitted for a degree, diploma or other qualification at any other university.

A handwritten signature in black ink, appearing to read 'Nial Peters', written in a cursive style.

Nial Peters

Foreword

No one ever stays for the ending credits, so I felt impelled to write something meaningful at the beginning instead. Having had whatever little literary flair I might once have possessed crushed from me by too much scientific-style writing (or was it too little? I'm not sure any more), it will be neither fluent nor eloquent, but anyway here goes...

I cannot say that I have researched this thoroughly, but it seems a safe assumption to make that not many caving accidents result in PhDs being awarded*. However, had it not been for that unfortunate event in the Austrian Alps several years ago, I suspect that I would never have been invited to Antarctica as “caving support”, would therefore never have met my supervisor, and probably would never have embarked on a PhD at all. A series of unfortunate and regrettable events perhaps? Well, I leave that for my examiners to determine. Just a few months into my PhD, I found myself playing on the swings in the Christchurch botanic gardens with my supervisor. “You know, this is exactly what I imagined doing a PhD would be like” I said†. Admittedly, my initial ideas about what was involved were somewhat wide of the mark, the remainder of the PhD certainly involved far fewer toys designed for young children. However, toys or no toys, the whole experience (with just a few notable exceptions) has been hugely enjoyable and, truthfully, I have absolutely no regrets. For fear of sounding vindictive, I will refrain from wishing you as much fun reading this dissertation as I had writing it, but you should at least glance-over the acknowledgements section at the end. To me at least, it is the most meaningful part of this thesis and accredits the greatest things that I take away from this – the experiences shared with my friends and colleagues in some of the most spectacular places on Earth.

*The “awarded” part is obviously somewhat unclear at the time of writing.

†His reply was: “Yeah, it’s pretty much how I imagined supervising would be too!”

Summary

Active lava lakes present a rare opportunity to observe directly the complex processes occurring within a magma body. Situated on Ross Island, Antarctica, the 3794-m-high crater of Erebus volcano has hosted a phonolite lava lake for decades. Previous studies have shown that many of the lake's characteristics, such as surface velocity, gas flux and gas composition, exhibit a pronounced pulsatory behaviour on a time-scale of ~ 10 min. Focusing primarily on the analysis of infra-red (IR) imagery acquired from the crater rim, this dissertation considers how the periodic behaviour of the Erebus lava lake evolves over decadal time periods, how the cyclic fluctuations of the different properties are interrelated and what can be inferred about the mechanisms occurring beneath the surface of the lake from these observations. Creation of new hardware, software and methodologies to facilitate these types of observations is a strong focus of this work.

Chapter 1 introduces the nature of active lava lakes, reviews previous studies of Erebus and presents in detail the research objectives that are addressed by the subsequent chapters. In Chapter 2, a new thermal camera system that was developed as part of this study is described. Designed to run autonomously at the crater-rim of Erebus, this system was installed in December 2012 and has enabled, for the first time, extended time-series of images to be acquired. Chapter 3 briefly describes some of the other hardware and software that was developed as part of this study and outlines how it has been utilised for volcano monitoring. In Chapter 4, a dataset of IR images collected between 2004–2011 is used to assess inter-annual variability in the pulsatory behaviour of the surface motion of the Erebus lava lake. The cyclic behaviour is found to be a sustained feature of the lake, and no obvious changes are observed across the time period analysed. Data collected with the camera system described in Chapter 2 are analysed in Chapter 5 and combined with measurements from other instruments to assess the correlation between the cyclic behaviours of different lake properties. Cycles in surface speed, surface elevation, gas flux and gas composition are found to be highly correlated with each other. In Chapter 6, the surface velocities calculated in the preceding chapters are revisited, and the two-dimensional structure of the flow field is analysed. Chapter 7 demonstrates how the motion tracking methodologies developed for studying the Erebus lava lake can be used to improve high time resolution sulphur dioxide flux estimates - a significant challenge faced in the study presented in Chapter 5. Finally, Chapter 8 presents a synthesis of the key findings and conclusions from the preceding chapters.

Contents

1	Introduction	1
1.1	Open-Vent Volcanism	2
1.2	Active Lava Lakes	2
1.3	Erebus Volcano	3
1.4	Degassing Mechanisms	6
1.4.1	Gas Pistoning	6
1.4.2	Pressurisation Changes	7
1.4.3	Bi-Directional Flow Instability	8
1.4.4	Bubble Wakes	9
1.5	Fieldwork	9
1.6	Summary of Activity	10
1.7	Research Objectives	12
1.7.1	Objective 1 – Improved Monitoring	12
1.7.2	Objective 2 – Assessment of Annual Variability of the Lava Lake Cycles	13
1.7.3	Objective 3 – Multi-parameter Observations of Cyclic Behaviour	13
1.7.4	Thesis Overview	13
1.8	Published and Submitted Materials	14
2	Development of an Autonomous Thermal Camera System for Mon- itoring the Lava Lake at Erebus Volcano	16
2.1	Introduction	17
2.2	Hardware	18
2.2.1	Camera	21
2.2.2	Control system	22
2.2.3	Power supply	22
2.2.4	Time synchronisation	23
2.2.5	Sensors	23
2.2.6	Data storage	24

2.2.7	Telemetry	25
2.2.8	Enclosure	26
2.3	Software	27
2.3.1	Overview	27
2.3.2	Implementation and architecture	27
2.3.3	Reuse potential	29
2.4	Results and discussion	29
2.4.1	The camera system	29
2.4.2	The dataset	30
2.4.3	Applications	31
3	Other Volcanic Monitoring Hardware and Software	33
3.1	Data Visualisation Software - AvoPlot	34
3.1.1	Introduction	34
3.1.2	Implementation and architecture	35
3.1.3	Reuse potential	35
3.1.4	Volcanological Applications	37
3.2	Portable Spectrometer Scanners	39
3.2.1	Introduction	39
3.2.2	Hardware and Software	40
3.2.3	Measuring SO ₂ Flux	43
3.2.4	Results	44
4	Decadal Persistence of Cycles in Lava Lake Motion	46
4.1	Introduction	47
4.2	Methodology	48
4.2.1	Camera Hardware	48
4.2.2	Data Selection	49
4.2.3	Motion Tracking	51
4.2.4	Time-Series Analysis	53
4.2.5	Bubbles	54
4.3	Results	61
4.3.1	Spectrograms	68
4.4	Discussion	70
4.5	Conclusions	74
5	Multi-parameter Observations of Cyclic Lava Lake Behaviour	75
5.1	Introduction	76

5.2	Methodology	77
5.2.1	Lava Lake Surface Velocity	77
5.2.2	SO ₂ Flux	78
5.2.3	Gas Composition	81
5.2.4	Lava Lake Surface Elevation	82
5.3	Results	82
5.4	Discussion	88
5.5	Conclusions	93
6	Analysis of the 2D Surface Velocity of the Erebus Lava Lake	95
6.1	Introduction	96
6.2	Methodology	96
6.2.1	Data Selection	96
6.2.2	Divergence	97
6.3	Results	98
6.4	Discussion	102
6.5	Conclusions	103
7	Use of Motion Estimation Algorithms for Improved SO₂ Measurements Using UV Cameras	104
7.1	Introduction	105
7.2	Methodology	107
7.2.1	Motion Estimation Algorithms	107
7.2.2	Algorithm Parameters	109
7.2.3	Using ATHAM as a Validation Tool	110
7.2.4	Villarrica Dataset	113
7.2.5	Image Registration	114
7.3	Results	115
7.4	Discussion	122
7.5	Conclusions	125
8	Conclusions	127
8.1	Improved Monitoring	128
8.2	Assessment of Annual Variability of the Lava Lake Cycles	129
8.3	Multi-parameter Observations of Cyclic Behaviour	129
8.4	The Future	130
	Acknowledgments	131

Appendix A Data Availability	132
Bibliography	135

Chapter 1

Introduction

“I can’t see any possible reason why this won’t work.”

– Bill McIntosh, Erebus, December 2010.

1.1 Open-Vent Volcanism

Broadly speaking, “open-vent” volcanoes are those that persistently expose magma at the Earth’s surface. In this respect, they encompass many of the popular stereotypes of volcanic activity, exhibiting sustained passive degassing, which is often accompanied sporadically by varying degrees of low-level explosive, active-degassing, activity [Tamburello et al., 2012]. At many open-vent volcanoes, the magma-atmosphere interface is very shallow, often with visible incandescence at the surface. Well-known examples of such systems include Villarrica in Chile, and Stromboli in the Aeolian Islands, both of which attract many thousands of tourists per year due to their impressive, but relatively benign, activity. The persistent activity also attracts volcanologists, in particular those interested in degassing processes [e.g. Witter et al., 2004, Shinohara and Witter, 2005, Mather et al., 2004a,b, Sawyer et al., 2011] and also those wishing to test new monitoring technologies [e.g. McGonigle et al., 2009, Mori and Burton, 2009, Bluth et al., 2007].

1.2 Active Lava Lakes

Persistently active lava lakes are a spectacular but rare form of open-vent volcanism found at only a handful of volcanoes around the world. Notable examples include Erta 'Ale in Ethiopia, Kilauea in Hawaii (since 2008), Nyiragongo in the Democratic Republic of the Congo and, the focus of this study, Erebus in Antarctica. An active lava lake is the exposed top of a volcano’s magmatic plumbing system. It is important to draw the distinction between active lava lakes, which maintain a link with the deeper magmatic system, and passive lava lakes which do not [Tilling, 1987]. The latter are formed due to ponding of erupted lava in a topographical depression, which then rapidly cools and solidifies giving the lake a lifespan of hours to days. Active lava lakes however, may have lifespans of many decades.

Longevity of a lava lake has been argued to reflect either effective transfer of magma between the lake and the deeper system [e.g. Oppenheimer et al., 2004, Francis et al., 1993], or a supply of gas bubbles from depth [Witham and Llewellyn, 2006, Bouche et al., 2010]. It can be shown experimentally that processes occurring at depth will manifest themselves at the surface as changes in the lake’s behaviour, for example its surface level [Witham et al., 2006] or gas flux [Divoux et al., 2009]. It follows therefore, that observations of lake properties can yield valuable insights into the processes occurring at depth in the magmatic system, where direct measurements

are not possible. This link with the deeper magmatic system makes the study of active lava lakes of particular importance.

1.3 Erebus Volcano

Erebus is a 3794-m-high stratovolcano located on Ross Island, Antarctica (Fig. 1.1). It is often claimed to be the southernmost active volcano in the world and is known to have hosted an active phonolite lava lake since at least 1972 [Giggenbach et al., 1973]. Although other small lakes have appeared intermittently over this period, the main, “Ray” lake (Fig. 1.2), has been a permanent feature of the crater throughout (with the notable exception of 1984–1985 when it was buried following sustained explosive eruptions) [Kyle et al., 1990].

Often described as an “ideal laboratory volcano”, the persistent, low-level activity of Erebus, does indeed make it particularly amenable to detailed close-range study. Ground-based measurements can be made from the rim of its main crater, which commands a direct view of the active lava lake. As one of only a handful of active lava lakes in the world [Tazieff, 1994], and being unique in its phonolitic composition [Kelly et al., 2008], it has received significant attention from the volcanological community, and a wide range of studies have been conducted to understand the magmatic processes responsible for its decadal persistence.

A high degree of thermal structure in the crust, which covers the lake, has enabled feature tracking algorithms to be applied to time series of infrared images so as to investigate the lake’s surface motion [Oppenheimer et al., 2009]. The same thermal images have also been used to study the thermal radiance of the lake [Calkins et al., 2008]. The continuity of thermal radiation from the lake also enables it to be used as a source for open-path Fourier Transform Infra-Red (FTIR) spectroscopy, allowing detailed analysis of the plume composition at a high temporal resolution [Oppenheimer and Kyle, 2008]. The extremely dry atmosphere of Antarctica is highly advantageous for FTIR measurements and has also enabled terrestrial laser scanning (TLS) observations to be made of the lake surface [Jones, 2013, Jones et al., 2014] during periods of particularly low humidity inside the crater.

As with all open-vent volcanoes, Erebus’s volcanic plume is a sustained feature. During favourable weather conditions it is often coherent and vertically rising over

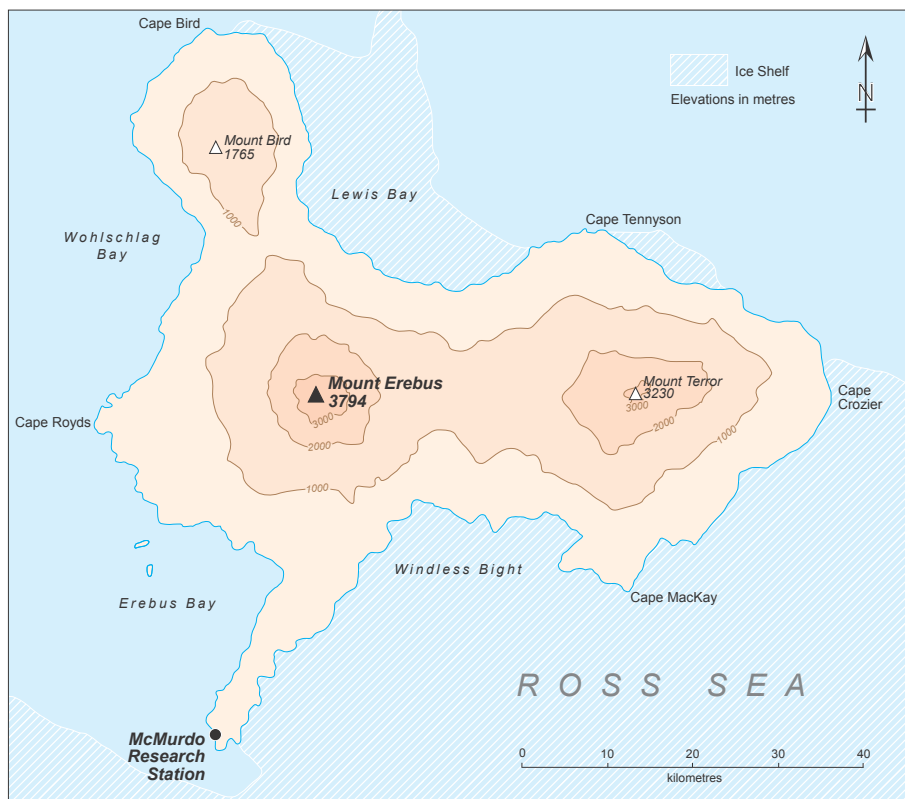
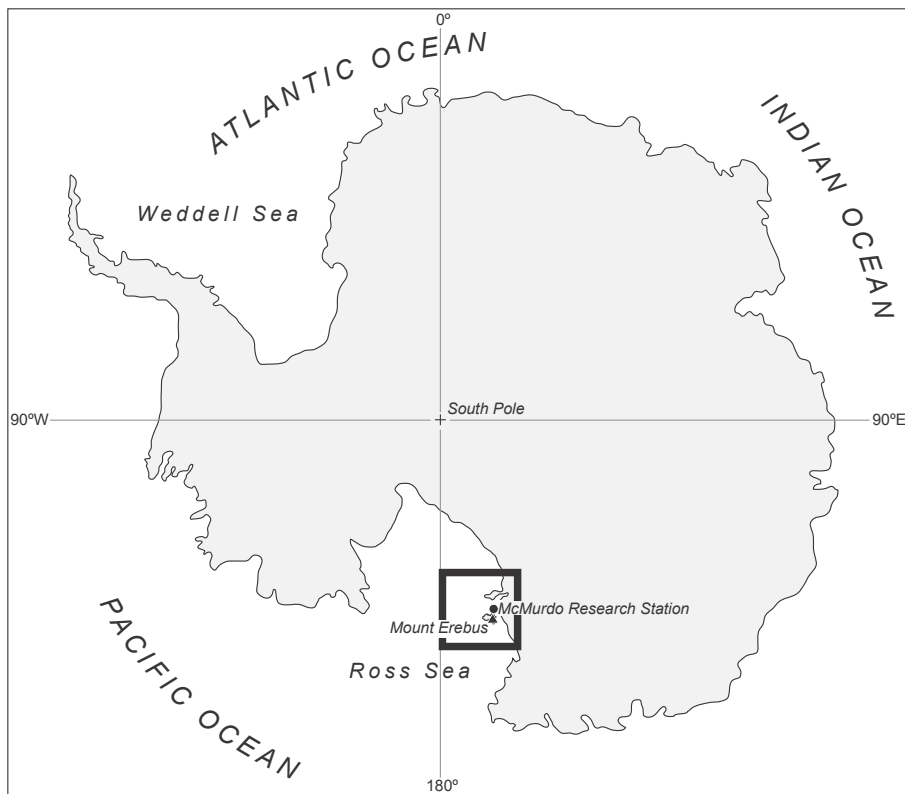


Figure 1.1: Map showing the location of Ross Island and Erebus volcano. Graphic created by the cartography section of the Cambridge University Geography Department.



Figure 1.2: The active lava lake at Erebus volcano as it appeared in December 2010. The lake is ~ 40 m across its long axis. Photo: Clive Oppenheimer

a sufficient distance to allow UV spectroscopy to be used to ascertain SO_2 flux [Kyle et al., 1990, Sweeney et al., 2008]. The use of a Dual Wide Field of View (DW-FOV) instrument has allowed rapid variations in flux to be studied [Boichu et al., 2010]. During less favourable weather conditions, the plume is often grounded across the northern side of the crater allowing direct measurements using “multi-gas” instruments [Shinohara, 2005, Aiuppa et al., 2005] to be made. In addition to complementing the FTIR measurements, these have also enabled the measurement of hydrogen emissions [Moussallam et al., 2012].

A common finding of the aforementioned studies is that many of the lava lake’s properties (SO_2 flux, gas composition, radiant heat, surface velocity) demonstrate pseudo-periodic fluctuations with a period of 5–18 min. In light of the observed behaviour of lab-based flow experiments [Huppert and Hallworth, 2007], it was proposed by Oppenheimer et al. [2009] that these fluctuations may be due to instability in bi-directional flow in the lake’s feeder conduit causing a pulsatory flow of hot, volatile-rich magma from the conduit into the lake. Pseudo-periodic behaviour has also been observed at Kīlauea, where it has been attributed to gas pistoning [Patrick et al., 2011, Orr and Rea, 2012], and at Erta 'Ale, where it has been explained by the regular arrival of large bubbles [Bouche et al., 2010]. Experiments conducted by Witham et al. [2006] have also suggested that bubble driven pressurisation changes could account for pulsatory behaviour. These mechanisms are discussed in greater detail and in the context of Erebus in Section 4.4.

The stable convective behaviour of the Erebus lava lake is punctuated by intermittent [De Lauro et al., 2009] Strombolian eruptions associated with the rupture of large (decametric) gas bubbles at the lake surface [Dibble et al., 2008, Gerst et al.,

2013]. Phases of increased and more intense Strombolian activity (several explosions per day, with ejecta escaping the main crater) recur, lasting 1–10 months and are followed by more extended intervals during which gas bubble bursts are less frequent and of a smaller size (a few explosions per week, with all ejecta being confined to the crater – see for example Jones et al. [2008]). The chemical and mineralogical composition of erupted lavas has remained constant for approximately 17 ka and the abundance of unusually large anorthoclase crystals is indicative of sustained shallow magma convection throughout this period [Kelly et al., 2008]. Indeed, the presence of such large crystals may be a significant influence on the behaviour of the shallow convection at Erebus [Molina et al., 2012]. Other properties of the lake also demonstrate remarkably consistent long-term behaviour, for example SO₂ flux [Sweeney et al., 2008] and radiant heat output [Wright and Pilger, 2008].

1.4 Degassing Mechanisms

As mentioned above, several different mechanisms have been proposed to explain the degassing behaviours observed at different lava lakes around the world. These are summarised in the following sections. Distinguishing between these mechanisms as being the process responsible for the behaviour of the Erebus lava lake is a major motivation behind the study of the surface velocity of the lake presented in this thesis.

1.4.1 Gas Pistoning

Gas pistoning has been proposed as a mechanism to explain observed surface level fluctuations both in the Pu'u 'Ō'ō lava lake at Kīlauea [Orr and Rea, 2012] and also in a perched lava channel on the flanks of Kīlauea during 2007 [Patrick et al., 2011]. Figure 1.3 shows the different stages of gas pistoning activity which, collectively, lead to cyclic variations in the surface level of the lava lake. The “filling” stage of the cycle is gradual, as small gas bubbles rising through the lake are trapped either beneath a solidified surface crust or a foam layer close to the surface. The increasing gas volume in the lake causes a rise in surface level. At a critical thickness, the layer of bubbles collapses, forming large gas slugs which escape from the lake causing a very rapid reduction in surface level. As small bubbles continue to rise through the lake, the process begins again.

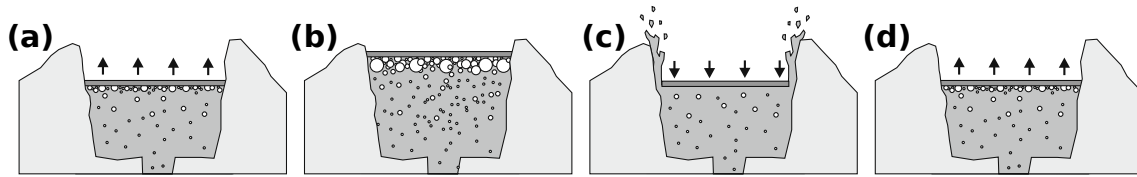


Figure 1.3: Cartoon of the gas pistoning mechanism (this is a modified version of the figure in Patrick et al. [2011]). **(a)** gas bubbles are trapped near the surface of the lake, either beneath a cooled crust or in a foam layer. **(b)** Gas accumulation in the lake causes an increase in surface level. **(c)** The foam layer collapses into a few large gas slugs which break the surface, sometimes explosively. **(d)** With the loss of gas, the lake surface returns to its normal level, and the process begins again.

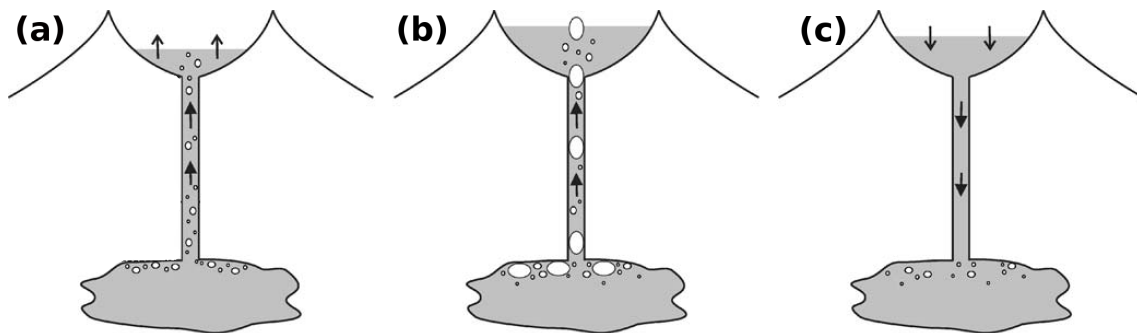


Figure 1.4: Cartoon of the bubble-driven pressurisation changes mechanism (figure taken from Witham et al. [2006]). **(a)** A regular supply of bubbles from depth drives upflow of magma into the lake. **(b)** The upflow of magma is impeded by the hydrostatic pressure in the lake, allowing bubbles to coalesce into large slugs. **(c)** The release of large gas slugs decreases the hydrostatic pressure at the base of the conduit relative to the lake, triggering a downflow of magma.

1.4.2 Pressurisation Changes

The bubble-driven pressurisation changes mechanism was proposed by Witham et al. [2006] based on laboratory based analogue models of lava lake systems. In their experiments, gas was injected into a vertical pipe (the conduit) filled with water, with a tank on the top (the lake) and connected to a large reservoir of water (such that the volume of water in the lake-conduit system could change). When the gas supply was first turned on, bubbles rising through the conduit drove an upflow of liquid from the conduit into the lake. As the lake filled, the increase in hydrostatic head stalled this upflow, allowing the bubbles to coalesce into large gas slugs. Release of these slugs causes fluctuations in the pressure at base of the conduit, and when these are sufficiently large the pressure in the lake exceeds that at the bottom of the conduit resulting in downflow of liquid. Downflow continues until hydrostatic equilibrium is regained at which point the cycle repeats.

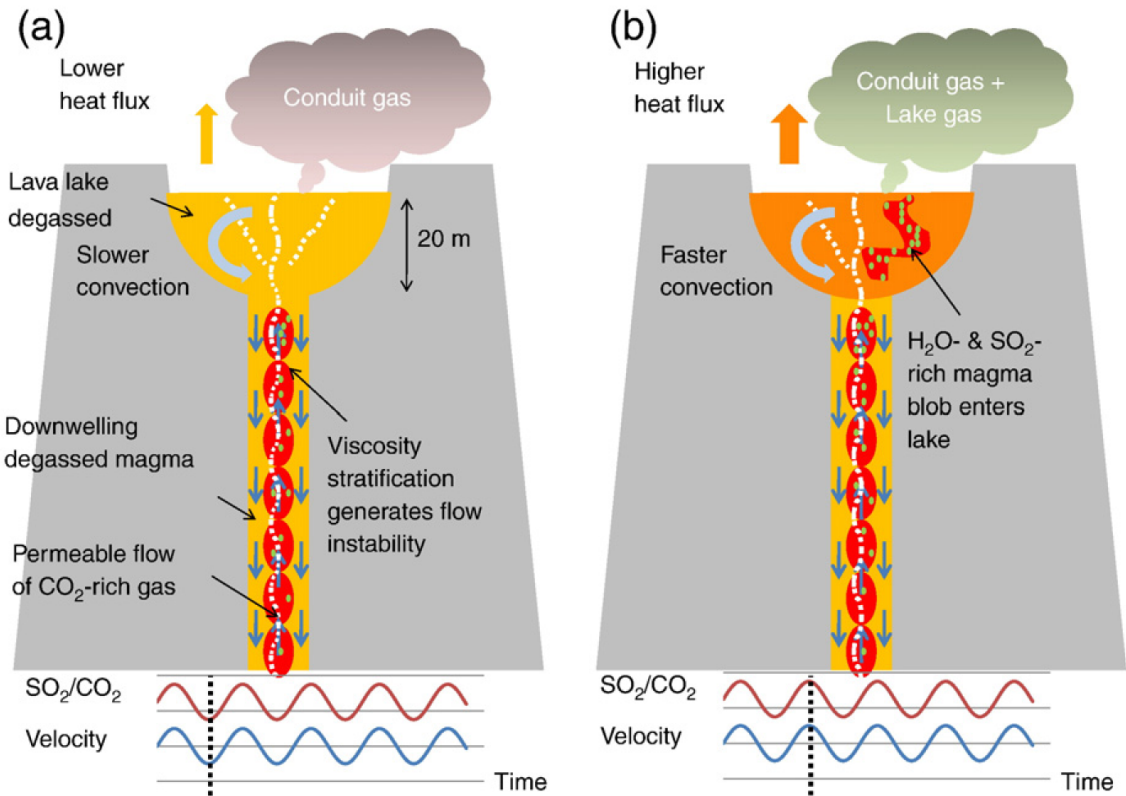


Figure 1.5: Cartoon of the bi-directional flow mechanism (figure taken from Oppenheimer et al. [2009]). Flow instability associated with bi-directional flow of magma in the conduit results in a pulsatory supply of bubble-rich magma from depth into the lake. **(a)** In between arrival of pulses of magma, convection in the lake is sluggish and the gas emissions are dominated by gas evolved at depth which is able to rise to the surface independent of the melt. **(b)** Pulses of magma result in increased convection speeds and a change in gas signature due to increased shallow exsolution.

1.4.3 Bi-Directional Flow Instability

Huppert and Hallworth [2007] demonstrated that, at certain Reynolds numbers, two fluids of different densities flowing in opposite directions in a vertical pipe develop a flow instability that leads to a highly periodic pulsed flow. Oppenheimer et al. [2009] proposed that such a mechanism may be applicable to volcanic conduit-lake systems. In this case, the density disparity between upflow and downflow is due to gas loss from magma in the lake. Hence, the upflow consists of bubble rich, low density magma from depth whereas the downflow consists of denser, degassed magma from the lake. The pulsatory arrival of fresh batches of magma into the lake gives rise to cyclic variations in the chemistry of the gas emissions, the surface velocity of the lake and its surface level.

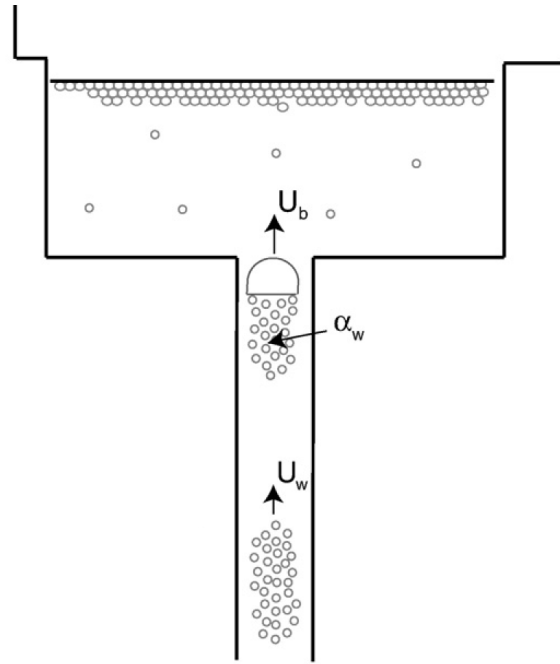


Figure 1.6: Sketch of the bubble wake mechanism (figure taken from Bouche et al. [2010]). Large bubbles rising through the conduit entrain small bubbles in their turbulent wake. The wake rises with the large bubble but can become unstable and detach. In this case the wake rises more slowly and independently of the large bubble, behaving as a bubble cluster.

1.4.4 Bubble Wakes

Although not directly related to cyclic behaviour of lava lakes, the degassing mechanism proposed by Bouche et al. [2010] is also of interest. Based on observations of the Erta 'Ale lava lake, the principal idea is that large bubbles whose buoyancy is sufficient to allow them to rise through the conduit independently of the melt create a turbulent wake behind them. Small bubbles which are largely static with respect to the melt, become entrained in the wake of the large bubbles and rise with them. If the wake grows beyond a critical size (proportional to the size of the leading bubble) it will detach from the bubble and rise independently through the melt, behaving as a bubble cluster. At Erta 'Ale, such bubble clusters are attributed with the sporadic fire-fountaining activity that is sometimes observed.

1.5 Fieldwork

All data relating to Erebus presented in this thesis have been collected as part of the Mount Erebus Volcano Observatory's field campaigns. Fieldwork on Erebus volcano is limited to the austral summer, and typically takes place between late-November



Figure 1.7: The Lower Erebus Hut (just visible in the bottom right) with the main Erebus crater clearly visible in the background.

and early-January. Where I refer to a field season by year, I am referring to the year in which it began.

Field operations are based at LEH, the Lower Erebus Hut, (Fig.1.7), which sits ~ 2 km from the crater rim on the north-west side of the caldera. Logistical support for the field campaigns is provided by the United States Antarctic Program, whose McMurdo station is a short helicopter flight from LEH. From LEH, the crater rim is reachable by first driving by snowmobile to Nausea Knob (NKB) and then walking the final 0.5 km.

I have participated in five consecutive field seasons at LEH, from 2009–2013. However, the 2009 field season was prior to my involvement in the study being presented here, and I worked primarily in the ice caves during this season.

1.6 Summary of Activity

In the following analyses, data from field campaigns between 2004 and 2013 have been used. Although the general behaviour of the lava lake at Erebus is fairly consistent from year to year, there are some observable variations. It is therefore important to set the results presented within the context of the state of activity of the lake during each of the respective field campaigns.

During the 2004 field season, there were two separate lava lakes present in the crater



Figure 1.8: A “large” bubble burst in the Erebus lava lake during the 2012 field campaign. The lake is ~ 20 m across and there is a ~ 2 s time delay between consecutive frames. Photos: Tim Burton

[Calkins et al., 2008]. By the 2005 field season, only the “Ray” lake remained [Davies et al., 2008], and no additional lakes have since been observed. All data presented here are from the “Ray” lake, and henceforth, I refer to it simply as the lava lake.

Since 2004, the visible surface area of the lake has reduced by a factor of approximately four. Possible reasons for this change are discussed in detail in Section 4.3. Despite the reduction in visible surface area, there have been no observable changes in the behaviour of the lava lake. Stable convective behaviour has been maintained throughout. The convective behaviour is characterised by the lateral migration of cracks in the lake’s crust across surface. These typically move radially outwards from the approximate centre of the lake, but more complex flow patterns with several “convection cells” and abrupt reversals of motion direction are also common. Lobes of fresh lava are occasionally observed to flow across the surface of the lake from upwelling regions, and there is visible subduction of the surface crust at the downwelling regions.

Bubbles of a variety of sizes are observed to surface in the lake. I describe bubbles as “large” if they result in significant ejection of material from the lake. Such bubbles (e.g. Fig. 1.8) are typically 10–30 m in diameter and cause a visible emptying of the lake. I classify such events as being distinct from the far more frequently occurring “small”, metre and sub-metre scale bubbles (e.g. panel (d) in Fig. 4.9) which arrive at the surface of the lake, but do not result in explosive activity.

A study of explosive events (due to large bubbles) between 2003–2011 using seismic data [Knox, 2012] shows that, with the notable exception of the period from late 2005 to early 2007, the frequency of explosive events has remained fairly constant

at a few per week, with ejecta being entirely confined to the crater. During 2005–2006, however, there were several explosions per day, often of sufficient magnitude to propel ejecta out of the crater, the frequency of these events then gradually declined and by the 2007 field season the lake had returned to its usual level of activity.

In 2013, Erebus once again entered a particularly active phase, with two or three explosions each day that were large enough for ejecta to exit the crater completely. Bombs several metres in length were observed to land up to ~ 400 m down-slope from the crater rim. At the time of writing in 2014, data from the seismic network deployed around Erebus [Aster et al., 2004] shows that large explosions continue to occur several times a day (although with a brief period in early March where activity subsided).

1.7 Research Objectives

The following sections outline the three key research objectives which this study strives to address. Section 1.7.4 then summarises how these fit together and how they have been structured within the context of this thesis. It will be seen that this work has involved the development of an imaging system and of data analysis techniques, coupled with detailed spatial and temporal analysis of image data and their interpretation.

1.7.1 Objective 1 – Improved Monitoring

Although field campaigns on Erebus typically last up to two months, the complex logistics involved in reaching LEH mean that typically data are only collected for a few weeks. The crater rim of Erebus is a formidable environment in which to conduct scientific measurements. High winds, corrosive gases and extremely low temperatures (< -50 °C during the winter) pose serious technical challenges for personnel and instruments alike, compounding the problem of short time series as frequent equipment failures lead to fragmented datasets. Gaps in the data make extended time series analysis problematic at best, and often impossible.

The first objective therefore, is to improve the data collection capabilities of the Mount Erebus Volcano Observatory.

1.7.2 Objective 2 – Assessment of Annual Variability of the Lava Lake Cycles

The first ground-based infra-red images of the Erebus lava lake were collected in 2004 [Calkins et al., 2008] and the dataset has been extended during each subsequent field campaign (except for the 2005 season, for which the data have not been made available to the author). While the data are far from continuous, they do provide suitable resolution and range for a multi-year analysis of the lava lake’s cyclic behaviour. Despite this, previous studies have only analysed very short time series (a few hours), and little is known about the persistence and/or evolution of the pulsatory behaviour on longer timescales.

The second objective therefore, is to characterise and evaluate the behaviour of lake on a decadal time scale.

1.7.3 Objective 3 – Multi-parameter Observations of Cyclic Behaviour

As noted in Section 1.3, cyclic behaviour has been observed in many different properties of the lake. However, due to the many problems associated with obtaining continuous datasets outlined above, the relationships between the cycles in different properties is largely unknown. These relationships are key in understanding the mechanism(s) responsible for the pulsatory behaviour of the lake. Furthermore, since the observed behaviour at the surface is likely controlled by processes occurring at depth, this presents a valuable opportunity to better understand the dynamics of the subsurface magmatic system at both Erebus and other open-vent volcanoes around the world.

The final objective therefore, is to definitively link the cycles in surface motion, gas composition, gas flux and lake surface level.

1.7.4 Thesis Overview

Each of the research objectives detailed above is addressed in a separate chapter of this thesis. The hardware and software that I have developed to facilitate improved data collection at Erebus (and other volcanoes around the world) is detailed in Chapters 2 and 3. In Chapter 4, I use the dataset of IR images collected between 2004–2011 to evaluate the pulsatory behaviour of the lava lake on an inter-annual

timescale. More recent data, collected using the camera system described in Chapter 2, is analysed in Chapter 5 and combined with data from other instruments to show the remarkable correlation between cycles in different properties of the lake (surface motion, gas composition, gas flux, and surface elevation). Chapter 7 demonstrates how some of the methods developed for analysing the IR images from Erebus may be used to address problems encountered in other fields of volcanic monitoring, specifically sulphur dioxide measurements using UV cameras. Finally, Chapter 8 gives an overview of the key findings in each chapter and discusses what constraints can be placed on the subsurface magmatic system of Erebus given the results presented in Chapters 4 and 5.

1.8 Published and Submitted Materials

A significant portion of this thesis is based on articles that have been published in peer-reviewed journals. As is the nature of modern science, parts of these studies have involved collaborative work and contributions from co-authors. A statement of co-author involvement is included at the beginning of each chapter, detailing the specifics of any collaborations involved. A summary of the publications arising from this study is given below, along with references to their positions within the body of this thesis.

Chapter 2 has been published as:

Peters, N., C. Oppenheimer, and P. Kyle. “Autonomous Thermal Camera System for Monitoring the Active Lava Lake at Erebus Volcano, Antarctica”. *Geoscientific Instrumentation, Methods and Data Systems* 3, no. 1 (February 5, 2014): 13–20.

Section 3.1 has been published as:

Peters, Nial. “AvoPlot: An Extensible Scientific Plotting Tool Based on Matplotlib”. *Journal of Open Research Software* 2, no. 1 (February 10, 2014).

Chapter 4 has been published as:

Peters, Nial, Clive Oppenheimer, Philip Kyle, and Nick Kingsbury. “Decadal Persistence of Cycles in Lava Lake Motion at Erebus Volcano, Antarctica”. *Earth and Planetary Science Letters* 395 (June 1, 2014): 1–12.

Chapter 5 has been published as:

Peters, N., C. Oppenheimer, D. R. Killingsworth, J. Frechette, and P. Kyle,

“Correlation of cycles in Lava Lake motion and degassing at Erebus Volcano, Antarctica”, *Geochemistry, Geophysics, Geosystems*, 2014

Chapter 7 has been published as:

Peters, N., A. Hoffmann, T. Barnie, M. Herzog, C. Oppenheimer, “Use of Motion Estimation Algorithms for Improved Flux Measurements Using SO₂ Cameras”, *Journal of Volcanology and Geothermal Research*, in press 2014.

These articles have not been reproduced verbatim within the thesis. In addition to the necessary changes to combine them into a single cohesive document, where appropriate they have also been extended to cover greater detail than was possible within the word- and figure-counts of the journals.

Chapter 2

Development of an Autonomous Thermal Camera System for Monitoring the Lava Lake at Erebus Volcano

The work presented in this chapter was undertaken in order to meet the “Improved Monitoring” research objective of this study (Section 1.7.1). In order to obtain longer continuous time series of IR images of the Erebus lava lake, a new thermal camera system has been developed and installed at the crater rim. The new system is designed to be autonomous, and capable of capturing images of the lava lake continuously throughout the year. This represents a significant improvement over previous systems which required the frequent attention of observatory researchers and could therefore only be operated during a few weeks of the annual field campaigns. The extreme environmental conditions at the summit of Erebus pose significant challenges for continuous monitoring equipment, and a custom made system was the only viable solution. In this chapter the hardware and software of the new system is described in detail.

The majority of content from this chapter has been published as: Peters, N., C. Openheimer, and P. Kyle. “Autonomous Thermal Camera System for Monitoring the Active Lava Lake at Erebus Volcano, Antarctica”. *Geoscientific Instrumentation, Methods and Data Systems* 3, no. 1 (February 5, 2014): 13–20.

All text and figures presented in this chapter were created by me, and the role of the co-authors did not extend beyond that of normal supervision. All design, construction, assembly and on-site installation of the camera system, telemetry system and power system was undertaken by me, with the notable exceptions of: (i) the most recent load-controller installed at the Nausea Knob “power station”, which was designed and installed by Nick Salava from the US Antarctic Program, (ii) the tripod mount for the camera, which was constructed by Kostas Milonidis. All the computer codes used for the camera system were written by me.

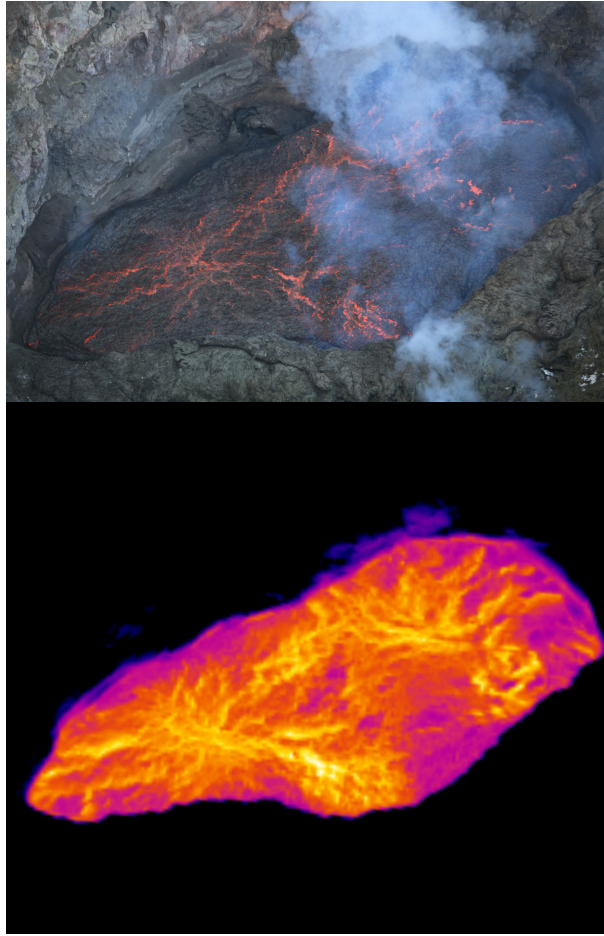


Figure 2.1: Simultaneous images from a digital SLR camera (note that the visibility of the lake in this image is exceptional) and the IR camera. The high degree of thermal structure in the lake's crust is clearly visible in the IR image and can be used in time-series of such data to estimate the surface motion of the lake (see Chapter 4). The ability of the IR camera to image through the volcanic plume is also clearly demonstrated. The lake is ~ 40 m across in these images.

2.1 Introduction

Thermal infrared (IR) cameras are an important tool in the study of lava lakes and have been used extensively in a number of lake studies around the world, ranging from quantification of radiative heat output [e.g. Calkins et al., 2008, Oppenheimer et al., 2004] to studying surface velocity [Oppenheimer et al., 2009]. They are also used more widely as an operational tool in volcano monitoring [e.g. Spampinato et al., 2011]. Although absorption of infrared radiation by volcanic gases makes accurate temperature measurements difficult to achieve [Sawyer and Burton, 2006], the ability to image through optically opaque volcanic plumes (Fig. 2.1) gives IR cameras a significant advantage over conventional cameras for monitoring lava lakes.

The Mount Erebus Volcano Observatory (MEVO) has been operating a thermal camera on Erebus during annual field campaigns (typically from late November to early January) since 2004. However, due to the many challenges of working in such an extreme environment, the time series of IR images tend to be very short and fragmented. In 2010, the decision was made to upgrade the thermal camera to a system that could potentially (contingent on a reliable power supply) run autonomously and continuously year-round. After two years of development and testing, the new system was installed during the 2012 field season.

Autonomous instruments have become a popular choice for researchers from a variety of disciplines working in Antarctica. Although it might seem an obvious solution to obtaining long time series measurements without the need for extended field campaigns, the technical challenges of creating such systems are numerous [see for example Bauguitte et al., 2011, Lawrence et al., 2004]. MEVO already operates several year-round seismic stations [Aster et al., 2004], however, the location of the thermal camera system and its high data rate meant that it presented many new challenges.

Autonomous thermal camera systems developed by other volcano observatories [e.g. Patrick et al., 2014] often rely on year-round telemetry to transmit data back to a centralised server in real-time. However, the power requirements of telemetry systems presently makes this approach unsuitable at Erebus. The system developed for Erebus also had to withstand far more extreme environmental conditions than are found at most other volcanoes that have year-round monitoring systems in place.

2.2 Hardware

The camera system is mostly an aggregation of off-the-shelf parts, with very little custom-made hardware involved. Although this has meant that some compromises have had to be made in terms of specifications, the reduction in cost and development time more than outweighs the disadvantages. Figures 2.2 and 2.3 show the main components used, which are discussed in detail in the following sections. The approximate cost of the components are outlined in Table 2.1. It should be noted however, that the control system could be used with any (possibly cheaper) camera unit, provided that it supports the GenICam interface.

Component	Approximate Cost
Thermal Camera	£20,000
Single Board Computer	£300
GPS	£80
Solid-state Hard-disc	£300
Sensors, SSR and Interface	£200
Enclosure (inc. IR window)	£400

Table 2.1: Approximate cost breakdown of thermal camera system.

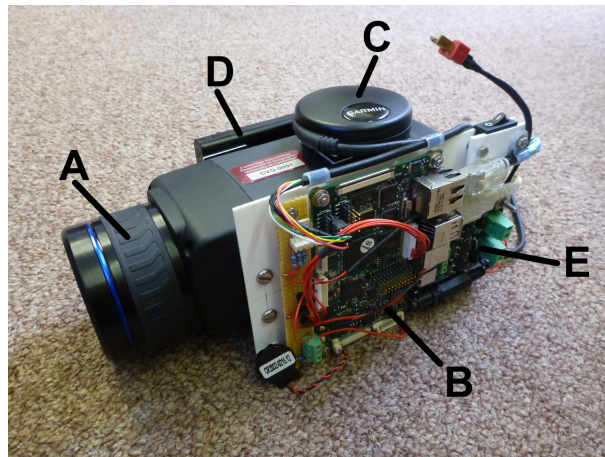


Figure 2.2: The main components of the camera system: (A) FLIR SC645 IR-camera, (B) BCT-RE2 single board computer, (C) Garmin 18 LVC GPS, (D) Intel 256 Gb solid-state hard-disc, (E) Phidgets solid-state relay.

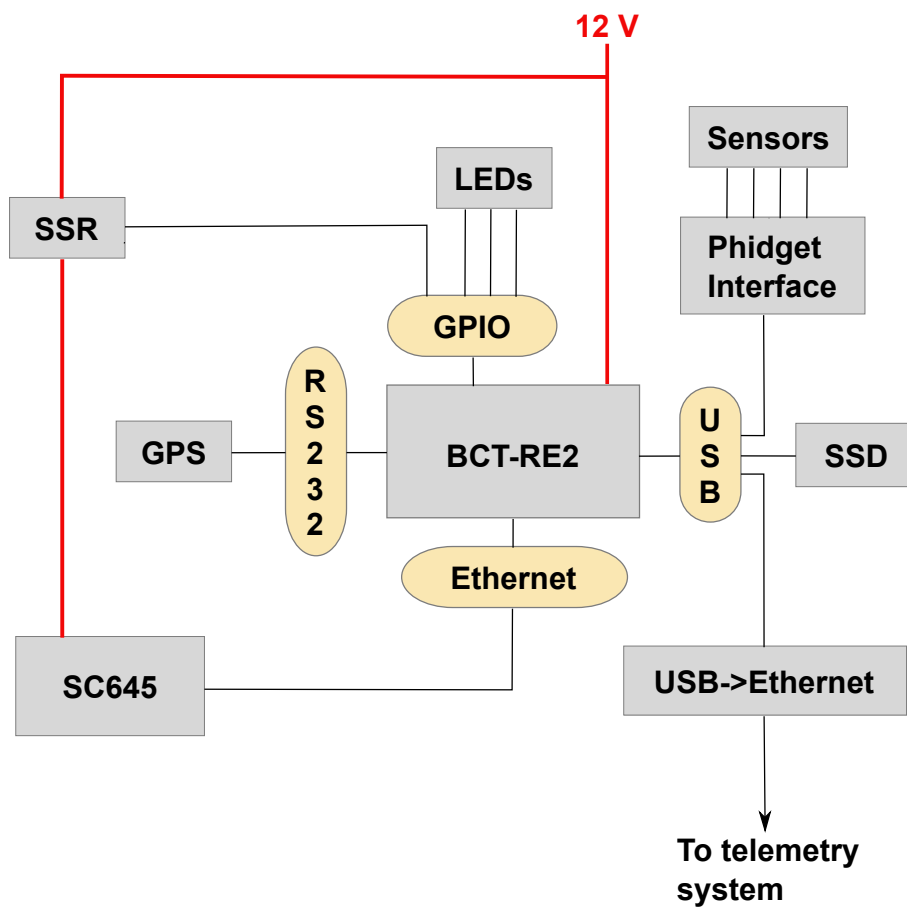


Figure 2.3: Block diagram showing the main components of the camera system.

2.2.1 Camera

The thermal camera unit itself is a FLIR SC645, with an uncooled 640×480 element detector, spectral range of $7.5\text{--}13\ \mu\text{m}$, and a spatial resolution (instantaneous field of view) of $0.69\ \text{mrad}$. This unit was chosen because, at the time of purchase, it was one of the few thermal cameras that allowed digital output of images in real-time (rather than storing them on an on-board storage medium such as a compact flash card). Furthermore, it supports the non-proprietary GenICam interface, which allows capture parameters to be set on the camera and images to be received via Ethernet.

The camera has three possible temperature ranges that it may be set to. In general we use the range $273\text{--}923\ \text{K}$, however, we have occasionally used the higher temperature range of $573\text{--}2273\ \text{K}$. The temperature range used for each image is stored in the PNG header data of the image file.

The camera has a built-in calibration source and surface temperatures could, in principle, be obtained per pixel. However, this would require parameterisation of in-band emissivity of the lava lake surface and atmospheric transmittance. While a reasonable estimate might be made for the former, the atmospheric transmittance is highly variable in space and time due to the fluctuating column amounts of volcanic gases in the optical path between the camera and the lake surface ($\sim 350\ \text{m}$ range; see Fig. 4.1). Several magmatic gas species emitted from the lake absorb in the detector’s waveband. In an instantaneous image, the transmittance will likely differ widely for each pixel due to the inhomogeneity of the volcanic plume. And from frame to frame, the plume structure may vary considerably. Thus, no unique value of transmittance would be appropriate to correct all the images to surface temperatures. Sawyer and Burton [2006] have shown how use of open-path Fourier transform spectroscopy to measure absorbing species in the optical path can provide some traction on this problem but only an imaging system would be able to constrain both the spatial and temporal variability in transmittance (and it would require a vast amount of data processing). Consequently, we have recorded images in the “radiometric” setting on the camera - in which the recorded signal is linearly proportional to in-band radiance reaching the detector. While these data are not well suited to estimating surface temperatures on the lake or radiative power outputs, they are valuable for studying lava lake motion, as discussed in Section 2.4.3.

2.2.2 Control system

The control system comprises of an ARM-based single board computer (SBC) which is connected to the camera via Ethernet. We used a Blue Chip Technology (BCT) RE2 SBC. Although there is a huge range of SBCs on the market that cover most combinations of interfaces, performance and power consumption, the choice of boards with an extended operating temperature range is considerably more limited. Due to the high computational expense of image compression, we found in testing that we needed a processor of at least 500 MHz. We also required multiple USB host ports and several GPIO (general purpose input/output) pins. With its 600 MHz ARM OMAP Cortex A8 processor, -40°C operating temperature and large range of interfaces, the BCT-RE2 met all our requirements at a power consumption of 2 W. The system runs Ubuntu Linux (version 10.10). Additional kernel modules had to be compiled to enable user-space access to the GPIO pins and also to facilitate use of a USB to Ethernet converter.

2.2.3 Power supply

Between 2011–2013 the entire power system which serves the crater rim was replaced. The old system was approaching ten years of service, and had become overly complex, and unreliable. A combination of extreme winds and corrosive gases makes the crater rim of Erebus an unsuitable site for solar panels and wind generators. Instead, power is generated 0.5 km down-slope at the Nausea Knob (NKB) seismic station site, where a 1000 Ah battery bank is charged using a ~ 0.5 kW array of photovoltaic panels, and a 100 W wind turbine. A Schaefer AEP-1500 inverter (chosen for its extended temperature range) is then used to transmit 230 V through a heavy-duty cable to the crater rim, where it is converted back to 12 V DC using an REL-185-1004 power supply (also chosen for its extended temperature range). The 230 V cable is buried beneath the surface to help protect it from UV radiation and volcanic bombs. Sufficient slack has been left in the cable that deformation of the ground where it is buried (e.g. due to a bomb impact) will not pull it taut and potentially damage it.

Based on past experience of unfamiliar researchers causing damage to equipment by connecting it to the wrong power supply, or with reversed polarity, the camera system incorporates a custom made protection circuit. Reverse polarity protection is provided by a MOSFET, and over-voltage protection is provided by a “crowbar” circuit, which short-circuits a resettable fuse (PTC) at supply voltages above 15 V.

It is our belief that all electronic field equipment should be protected in a similar way. Protection circuits are straightforward to make, cost almost nothing, and prevent simple mistakes from totally destroying equipment. We cannot stress this point enough!

Power to the camera itself is controlled via one of the SBC's GPIO pins using a Phidgets 3053 solid-state relay (SSR). This allows the control software to "hard-restart" the camera in case of problems.

Overall, the system requires ~ 11 W of power. Between 6–7 W is used by the camera itself, ~ 2 W by the SBC and the remainder by the hard disc.

2.2.4 Time synchronisation

The majority of volcanological research requires the inter-comparison of data from many different instruments, making accurate time stamping of the utmost importance. To ensure that the system time on the SBC did not drift, we linked it via its RS232 serial port to a Garmin GPS 18 LVC receiver. The system time was then synchronised with the GPS using standard Linux utilities. Initially we tried the `gpsd` program, however, we found it to consume excessive system resources and so we switched to the built-in GPS support in `ntpd`. We had hoped to use the LinuxPPS kernel module to provide very accurate time synchronisation using the PPS (pulse per second) signal output from the GPS. Unfortunately, the RS232 port on the BCT-RE2 is implemented over the I2C bus, and the driver for this does not currently support LinuxPPS. Despite this, we found that synchronisation was possible to within a few milliseconds just using the NMEA data from the GPS. The control software for the camera has been designed to allow a sufficient delay, following a reboot, for GPS time synchronisation to occur before image capture resumes.

2.2.5 Sensors

The power consumption of the camera system, together with the temperature inside and outside of its enclosure are monitored using Phidgets sensors. These are connected to the SBC via USB using a Phidgets 1018_2 interface board. Phidgets sensors were chosen for their ease of use and simple software interface.

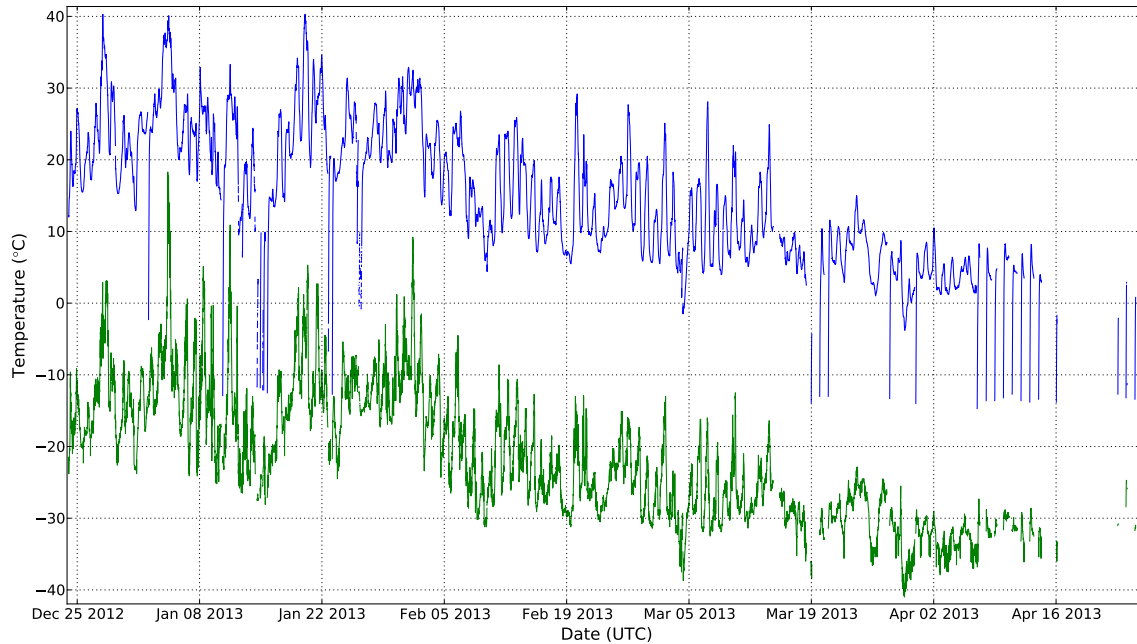


Figure 2.4: Time series of temperature readings both inside (upper series) and outside (lower series) of the camera enclosure. It should be noted that the outside temperatures reported appear to be $\sim 10^\circ\text{C}$ higher than the actual air temperature.

The data collected by the sensors between December 2012 and April 2013 show a stable power consumption of ~ 11 W throughout. Figure 2.4 shows the recorded temperatures. The sharp drops in internal temperature are caused by power outages, and the subsequent rapid heating clearly demonstrates the ability of the system to keep itself warm simply using waste heat from the SBC and hard disc. It should be noted that the external temperature sensor seems to over-read by $\sim 10^\circ\text{C}$ compared to measurements made with a handheld thermocouple. This is likely caused by heat leakage from the camera enclosure into the external temperature sensor enclosure.

2.2.6 Data storage

The low temperature performance of hard disc drives (HDDs) seems to be poorly researched and/or documented. When choosing a data storage solution for the camera system we were unable to find any high-capacity discs with an extended temperature range. In the end we chose a 250 Gb Intel solid state drive (SSD). While it was not rated for low operating temperatures, it did have a lower power consumption than conventional HDDs. Some consideration was given to the idea of storing batches of images on the SBC's internal flash memory and then periodically transferring them to the SSD. Although this would have reduced the power consumption of the

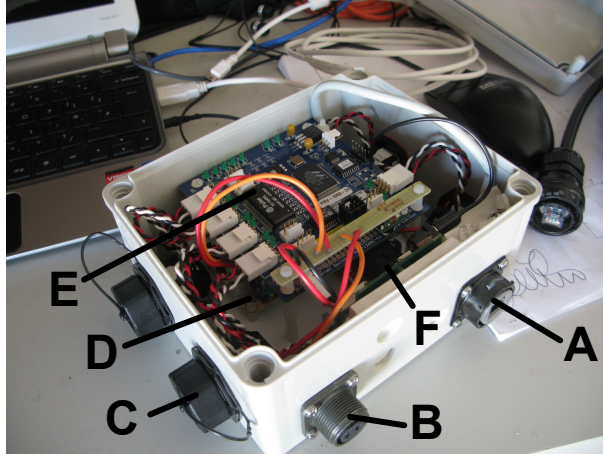


Figure 2.5: The main components of the new network switch installed at the crater rim in 2011: (A) Power-over-Ethernet (POE) port for TL-45, (B) 12 V power input, (C) weather-proof Ethernet ports, (D) 12 V to 24 V DC/DC converter to power TL-45, (E) Parvus PRV-1059 Ethernet switch, (F) POE power injector.

system, since the SSD would only need to be powered up occasionally, we decided that the risk of data loss due to the increased complexity outweighed the potential benefits.

2.2.7 Telemetry

During the annual MEVO field campaign, a Trango TL-45 5 GHz wireless Ethernet link is used to telemeter data from instruments at the crater rim back to servers at our field camp. Following numerous failures of the system due to cold-damage of cables and connectors, the whole network system surrounding the TL-45 was replaced in 2011. In the new system, instruments are connected to the TL-45 via a low-power, low-temperature Parvus PRV-1059 Ethernet switch using low-temperature ethernet cable and Amphenol™ weather-proof connectors (Fig. 2.5). The high power consumption of the telemetry system (~ 12 W) means that it is only operated during the field campaign (when there is ample solar charging). The thermal camera system incorporates a USB to Ethernet converter to provide it with a second Ethernet interface and allow connection to the telemetry system during this period. Images can then be streamed to the field camp in addition to being stored on the SSD, providing some redundancy in data storage and the ability to monitor the lava lake in real-time.



Figure 2.6: The new thermal camera system installed at the crater rim of Erebus volcano. Photo: Clive Oppenheimer

2.2.8 Enclosure

Previous thermal cameras operated by MEVO were simply wrapped in bubble-wrap to protect them from the cold. Somewhat surprisingly this proved to be very effective. However, the corrosive gases emitted from the volcano rapidly took their toll, and metal parts (including electrical contacts) soon degraded and became unusable. An additional problem with previous systems was that standard tripod mounts were not rigid enough to prevent considerable camera shake caused by the high winds which frequent the summit of Erebus. An air-tight plastic Peli™ case was used as the enclosure for the new system, to which a rigid aluminium frame was bolted. The frame was attached to a tripod comprised of scaffolding bars to form a solid mounting which does not vibrate in the wind (Fig. 2.6). The IR window used in the camera enclosure is 3 mm thick Germanium with a 8-12 μm anti-reflective coating.

All external fixtures are either aluminium or stainless steel to reduce corrosion. The camera casing has been insulated with expanded polystyrene and all internal fixings are made of plastic to reduce conductive heat loss. Combined with the heat generated by the enclosed electronics, this meant that the temperature inside the enclosure remained above $-5\text{ }^{\circ}\text{C}$ throughout its operation in 2013 (except during power outages), despite external temperatures of less than $-50\text{ }^{\circ}\text{C}$ (Fig. 2.4).

2.3 Software

2.3.1 Overview

The control software for the camera system is comprised of several small programs which are managed by an initialisation script. All programs share a single configuration file, which can be edited to change the operational parameters of the system. The main capture program is responsible for setting the capture parameters of the camera, and then entering an infinite loop of capturing images, performing some basic pre-processing on them and then compressing them as PNG files. During the field campaigns when the telemetry system is in place, two separate server programs are used to send images and sensor data to a viewer program which runs on a computer at the field camp. This allows real-time monitoring of the lava lake and of the thermal camera system itself.

2.3.2 Implementation and architecture

The initialisation script is written in Bash. It is launched automatically on system boot by `upstart` (a replacement for the System V `init` daemon) once the networking and GPIO services have been started. The script performs a series of system checks such as ensuring that the SSD is mounted correctly, initialises GPS time synchronisation and then starts the capture and server programs. If errors are encountered that would prevent the capture of images, then the whole system is restarted. An error handling safety net is provided by the kernel `watchdog` module, which will restart the system if the capture software crashes for some reason or if the system “freezes” (runs out of memory, or has excessive CPU usage). As a final layer of fault tolerance, a `crontab` entry is used to restart the whole system once a week.

The main capture program is written in C++ and uses `libconfig++` for reading the configuration file, `libpng` for compressing and storing the images, and `libaravis` [Pacaud, 2011] for interfacing with the camera. The images output from the camera have a bit depth of 16. To reduce the size of the PNG files produced, they are scaled to a bit depth of 8 before being compressed. In order to preserve as much dynamic range in the pixels representing the lava lake as possible, the images are first thresholded to set all low valued pixels to zero. They are then linearly scaled

to 8 bit values as follows:

$$x_8 = (x_{16} - \min_{16}) \times \frac{255}{\max_{16} - \min_{16}} \quad (2.1)$$

where x_8 is the 8 bit pixel value, x_{16} is the 16 bit pixel value and \min_{16} and \max_{16} are the minimum and maximum pixel values in the 16 bit image respectively.

Converting the images to 8 bit using this algorithm is sensitive to dead or hot pixels, since these will skew the minimum and maximum pixel values. This is potentially disastrous, as the dynamic range of pixels within the lake in the resulting 8 bit images could be severely impacted. To prevent this from happening, a simple dead/hot pixel detection algorithm is applied to each image before conversion to 8 bit. This works by comparing each pixel to its neighbours and looking for very strong contrasts in value. In order to implement this algorithm efficiently, it ignores the edge pixels of the image, meaning that every pixel analysed has eight neighbours. Edge pixels are simply set to zero. Image files are written to disc using incremental numbers as file names. This method was chosen as it will not result in images being overwritten in the event of unexpected system restarts (e.g. due to power cuts) or loss of system time.

The server programs are written in C. The server for the sensor data uses libphidgets to interface with the sensors. Values read are recorded in a log file and also passed to any connected clients via a socket. The server program for the images works by using inotify to monitor the output directory for the images from the capture program (which is read from the capture program's configuration file). Each new image detected is transmitted to any connected clients as a string of raw PNG data, and the user-gpio kernel module is used to flash a status LED connected to one of the GPIO pins of the SBC. The server programs were written as separate programs from the capture program in order to keep the latter as simple, and therefore reliable, as possible.

The viewer program is written in Python and connects to the server programs via a standard socket. Multiple instances of the viewer can connect to the server programs simultaneously.

2.3.3 Reuse potential

All the software created for this project is freely available under the terms of the Gnu Public License from <http://dx.doi.org/10.6084/m9.figshare.784942>. Although the image acquisition software is specific to the SC645 camera, fairly minor modifications would enable it to work with any camera that supports the GenICam interface. It is not however, suitable for applications that need capture rates above a few frames per second. The image server and viewer programs could be reused “as is” for any image capture application that outputs PNG files, provided that the server side system has inotify.

2.4 Results and discussion

2.4.1 The camera system

The system was installed at the crater rim of Erebus in November 2012 and, other than a few minor issues with the camera being unable to focus to infinity when it was first mounted in the enclosure, it operated without any problems up until the end of the 2012 field season. It was then left running with the intention that it continue to acquire images continuously until the following field season. On returning to the volcano in November 2013, we discovered that the battery bank which serves the camera system had failed. Several of the batteries had cracked casings and all registered ~ 6 V. The exact cause for this failure was never determined, however, we suspect that it was caused by a faulty wind turbine system which allowed the batteries to over-discharge and subsequently freeze. As a result, power was never restored to the camera after the winter, and therefore images were only acquired up until 26 April 2013. It is worth noting however, that when power was restored, the system resumed acquisition without any further intervention. The wind turbine and associated controller have now been replaced with a new, redundant system which we hope will provide a greater degree of protection for the battery bank.

A further failure of the system was that the stainless-steel mounting bolt which secures the camera enclosure to the tripod had bent, allowing the enclosure to rotate such that the camera was no longer pointing at the lake. Fortunately, this had happened after the power had failed, and so no additional data were lost. It is somewhat surprising that such a small enclosure can provide enough wind-resistance to bend a 5 mm diameter bolt. We have replaced the bolt with a much larger one, and plans

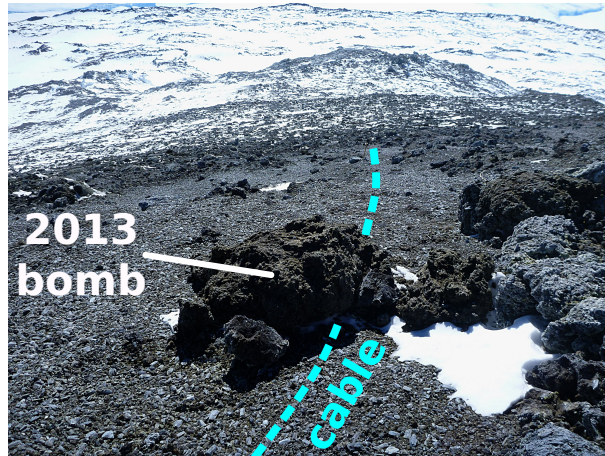


Figure 2.7: Photograph showing the landing site of a large (~ 1.5 m diameter) volcanic bomb which was erupted in 2013 and landed directly on top of the 230 V cable which takes power from Nausea Knob to the crater rim. Luckily the cable seemed to be undamaged.

are underway to replace the entire tripod setup with a more substantial mounting system during the 2014 field campaign.

Despite the problems outlined above, the camera system worked well until late April when the sun stopped rising and solar charging ended. Almost four million images were acquired; the largest thermal infrared dataset ever recorded on Erebus. The system was left running again after the 2013 field season and, with the improved power system in place, we are hopeful of achieving year-round data acquisition during 2014. However, the increased level of explosive activity which began in 2013 and continued until late-February 2014 (Section 1.6) has added significantly to the risk of terminal failure of the system. During this period, large bombs, up to 4 m in length, were being erupted from the crater two to three times a day. One of these landed within a few metres of the camera system itself, and several had struck the cable that carries power to the crater rim (Fig. 2.7). Fortunately, the cable appeared undamaged by the impacts – rewarding the huge efforts that were taken to bury it! We have no way to tell if the camera system is still operational until we return to Erebus in November 2014.

2.4.2 The dataset

Figure 2.8 shows a short sequence of images captured by the camera system during testing in 2010, which document a large gas slug arriving in the lake. These

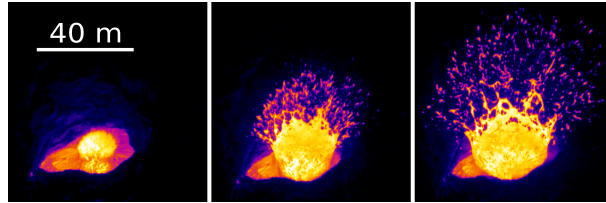


Figure 2.8: A sequence of three IR images recorded ~ 0.17 s apart, showing the arrival of a large gas slug into the lava lake.

images were captured at 6 Hz, whereas the camera system ordinarily operates at 0.5 Hz. The dataset from the new camera system is freely available at <http://www.usap-data.org/entry/NSF-ANT11-42083/>. All images in the archive are in PNG format, and contain important meta-data in their file headers. Information about extracting these meta-data can be found in the README file which is part of the archive. At the time of writing the archive contains all the images that were captured by the camera system during the 2012 field season. This will be expanded upon annually as new data are recovered from the camera. Older datasets from previous camera systems will also be made available once the images have been converted into a suitable archive format. It should be noted that the images are obtained with an oblique viewing geometry, and require orthorectification before they are used. This has not been applied to the images in the archive. Techniques for correcting the images are discussed in Section 4.2.3.

2.4.3 Applications

As discussed in detail in Chapter 4, the Erebus lava lake is covered by a thin crust of cooler material. As the lake convects, this crust cracks and the cracks migrate across the surface driven by the motion of the underlying lava. Figure 2.1 shows a comparison between the visible appearance of the lake and an IR image (it should be noted that such a clear view of the lake is exceptionally rare). As can be seen in the figure, the cracks are clearly visible in the IR image and, as demonstrated by Oppenheimer et al. [2009], can be tracked using a wavelets based motion estimation algorithm [Magarey and Kingsbury, 1998] to determine the surface velocity of the lake. Figure 2.9 shows a short time series of mean lake surface speed calculated in this way. The pulsatory behaviour of the surface motion is thought to be associated with a density-driven bi-directional flow of magma in the conduit feeding the lake [Oppenheimer et al., 2009]. A primary goal of the new thermal camera system is to provide long, uninterrupted observations of the pulsatory behaviour of the

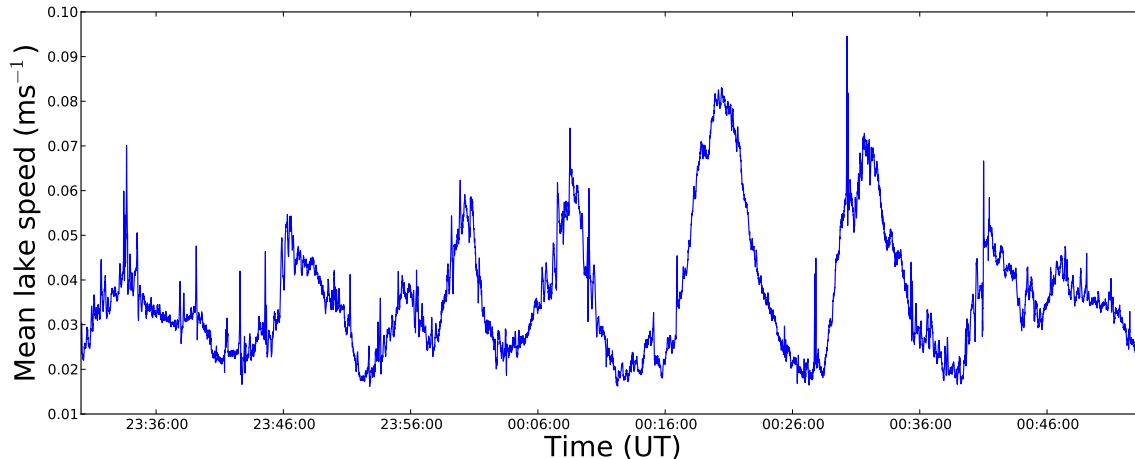


Figure 2.9: Time series of mean lake surface speed calculated from IR images captured on 22 December 2010. The pulsatory behaviour of the lake is clearly visible with a period of ~ 12 min. The sharp spikes in speed (“shot noise”) are caused by bubbles reaching the surface of the lake.

lake to facilitate a detailed comparison with numerical simulations [Molina et al., 2012], analogue experiments [Witham et al., 2006, Huppert and Hallworth, 2007] and datasets from other instruments deployed at Erebus. The latter is covered in Chapter 5.

The episodic arrival of large gas bubbles into the lake cause spectacular Strombolian eruptions (Fig. 2.8). Although detailed studies have been made of these events using other techniques [Gerst et al., 2013, Jones et al., 2008], little has yet been learnt of how they influence the pulsatory behaviour of the lake. Previous thermal camera systems on Erebus did not record the majority of the bubble events since their capture rate was too slow. However, the new system will allow explosive episodes to be recorded. Explosions can easily be identified in the data either as “shot noise” in the calculated surface motion or, for large events, as a sharp (factor of ~ 5) increase in the compressed size of the image files. Although some analysis of bubble events is presented in Chapter 4, sufficiently long datasets were not available to conduct an in-depth study at the time of writing. This is therefore left as a promising avenue of research for future studies.

Chapter 3

Other Volcanic Monitoring Hardware and Software

The work presented in this chapter was undertaken as part of the “Improved Monitoring” research objective of this study (Section 1.7.1). Although the outputs have not featured significantly in other sections of this dissertation, they do constitute a large body of work, which is relevant to the monitoring of open-vent volcanoes more generally. As such, we feel that it is necessary to present them here. However, this chapter should be viewed as a summary of the work, rather than an in-depth analysis. We present new data visualisation software, which, in addition to providing generic plotting capabilities, can be customised using plug-ins to provide very specific data processing capabilities such as real-time SO₂ measurements. We also present portable spectrometer scanning units for making spectroscopic measurements at remote field sites.

Section 3.1 of this chapter has been published as: Peters, Nial. “AvoPlot: An Extensible Scientific Plotting Tool Based on Matplotlib”. *Journal of Open Research Software* 2, no. 1 (February 10, 2014).

All the hardware and software described in the chapter was created independently, by me.

3.1 Data Visualisation Software - AvoPlot

3.1.1 Introduction

AvoPlot is a simple-to-use graphical plotting program written in Python [van Rossum, 2013] and making extensive use of the matplotlib plotting library [Hunter, 2007]. The software was originally created as a real-time visualisation program for monitoring sulphur dioxide emissions from volcanoes. However, with several different projects under way in our research group, all requiring a different set of data manipulation tools but similar user interfaces, it soon became clear that a more generic solution would be extremely useful; AvoPlot was designed to fill this role. Essentially, AvoPlot aims to achieve two things: (i) To provide a simple and intuitive graphical user interface for the matplotlib plotting library, with tools for importing common data formats. (ii) To provide an extensible platform that researchers can easily customise to suit their specific data visualisation and analysis requirements.

Although there are numerous open-source plotting programs already available, none (that the author is aware of) provide the same functionality as AvoPlot. Spreadsheet programs such as OpenOffice Calc [Apache, 2013] and Gnumeric [Gnome, 2013] cannot load arbitrary data types, and also lack good data navigation tools (panning, zooming etc.) for their plots. The plot viewer built into matplotlib, provides good data navigation tools, but has very few graphical facilities for editing plot parameters. The Veusz [Sanders, 2013] program incorporates most of the features of AvoPlot. It has a comprehensive graphical interface for creating and editing plots, as well as providing a plug-in interface to allow users to load arbitrary data types and define new analysis functions. However, Veusz implements its own plotting backend which is unlikely to be as familiar to developers as matplotlib and has a smaller community providing support. Furthermore, the scope for writing complex plug-ins is far more limited than in AvoPlot, which allows developers the freedom to use any wxPython [Dunn, 2003, Rappin and Dunn, 2006] constructs when writing their plug-in interfaces.

At the time of writing, AvoPlot is still at an early stage of development. Although two stable versions have been released, the available functionality is somewhat limited. Despite this, it has already been used in several different volcanological projects and was used extensively by the author during the preparation of this thesis. Plug-ins for working with differential optical absorption spectroscopy (DOAS) data and Fourier transform infrared (FTIR) spectra are currently under development and will

be released in due course.

3.1.2 Implementation and architecture

AvoPlot is written in pure Python. Graphical interface elements are implemented using wxPython and plots are created and displayed using matplotlib and its wx-agg backend.

The software consists of two major components; the user interface (UI) and the plug-in system. The UI provides a generic graphical interface to much of matplotlib’s functionality, allowing users to change plot parameters (such as line styles, colours etc.) without needing to write any code. It also allows users to interact with any plug-ins that have been installed. An overview of the UI is shown in Fig. 3.1.

The plug-in system is intended to give developers a simple way both to import their specific data into the UI, and to provide tools for manipulating them. Details of how to write plug-ins are given in the AvoPlot documentation which can be found in the “doc” folder of the source distribution, or online as part of the software archive. Furthermore, example plug-ins can be found in the “examples” folder of the source distribution.

AvoPlot comes with a simple file import plug-in which will be installed automatically. Currently, this can only load text files containing columns of numerical data. However, it will be extended in future releases to support other file types such as CSV, Excel spreadsheets etc. Sample data for creating a plot with this plug-in are provided in the “spectrum_data.txt” file of the “examples” folder of the source distribution and step-by-step instructions for its use can be found in the AvoPlot documentation.

3.1.3 Reuse potential

As a standalone program, AvoPlot provides an easy to use, generic plotting tool capable of producing publication-quality figures. Although the current feature set is relatively limited, future development will focus on exposing more of matplotlib’s functionality through AvoPlot’s UI. This will give users access to matplotlib’s extensive capabilities without requiring them to write Python scripts. In this respect,

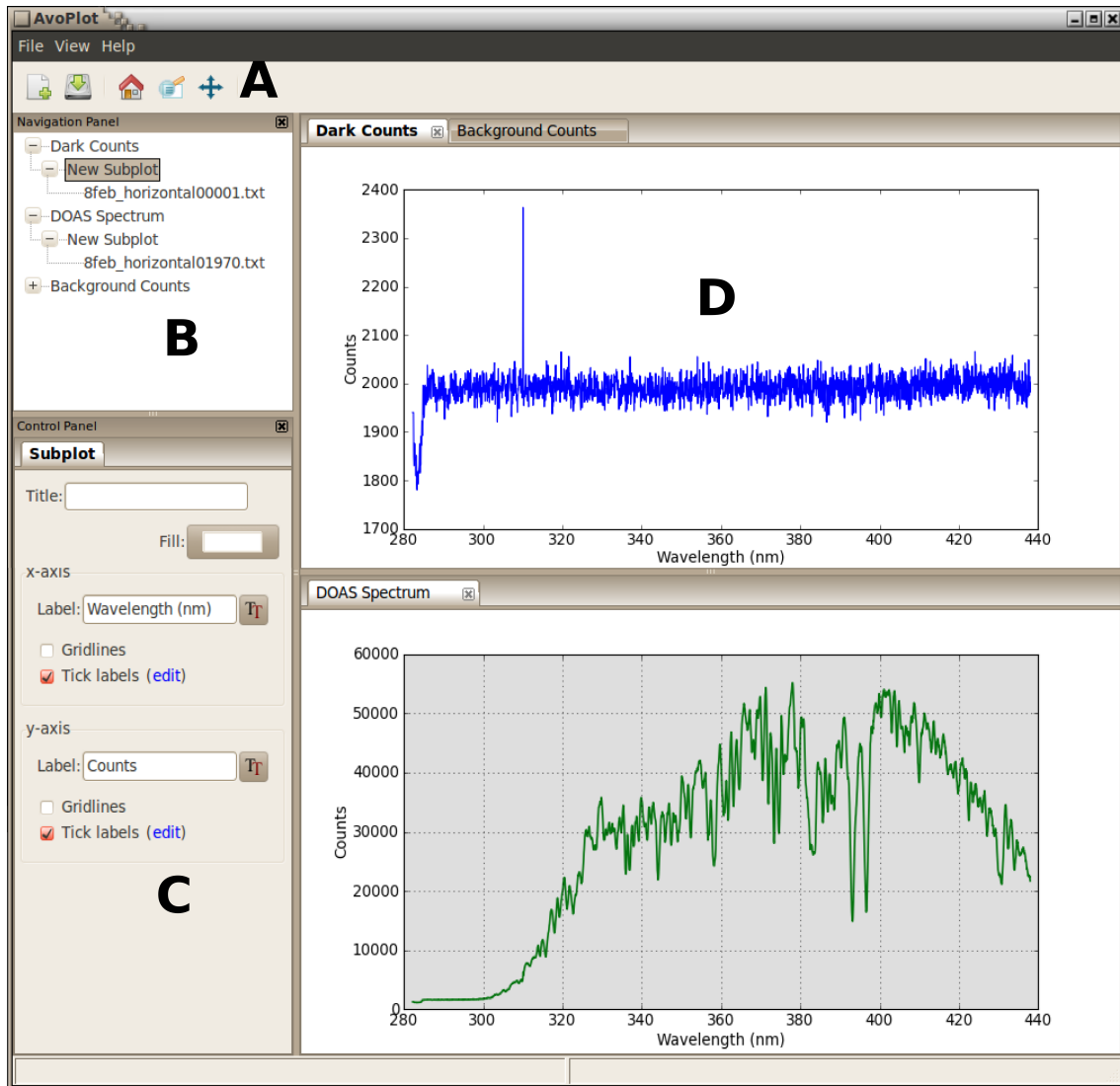


Figure 3.1: Screen-shot of the AvoPlot user interface showing its main components: **A)** Toolbar providing the “standard” matplotlib pan, zoom and save controls. **B)** Navigation panel allowing selection of different plots, axes and data series. **C)** Control panel providing controls for editing plot properties such as axis titles, line styles etc. Any tools provided by the plug-in for the currently selected plot are also displayed here under a different tab. **D)** Tabbed plot window with a variable number of panes allowing multiple plots to be viewed simultaneously.

the program has a high reuse potential “as is” for a wide spectrum of end-users regardless of coding experience.

However, the main reuse potential for AvoPlot comes from its plug-in based architecture. With just a few lines of relatively simple code, researchers can write a plug-in that will plot their specific data set (which may be in a format difficult to import with mainstream plotting programs) in the AvoPlot UI. They can then take advantage of a feature-rich plot editing environment to customise their plot without having to edit or run scripts. Furthermore, AvoPlot plug-ins are distributed using Python’s distutils system [Ward and Baxter, 2013], making it simple for other researchers (who may have no programming experience) to install plug-ins written by their peers.

In addition to data import, AvoPlot plug-ins also allow researchers to easily integrate their own data manipulation and analysis tools into the AvoPlot UI, enabling them to create a graphical data processing software without having to write extensive UI code of their own. The aim is to encourage researchers to make the analysis tools which they create user-friendly and accessible for others, who may not be programmers.

The software has been successfully tested (functional testing) on Linux (Ubuntu and OpenSUSE), Microsoft Windows (XP, 7 and 64bit 8) and MacOSX. There is no reason however, why AvoPlot cannot be installed on any system that can run Python.

3.1.4 Volcanological Applications

As already discussed, AvoPlot is designed to be a generic scientific plotting tool that can be specialised to suit particular applications through the use of plug-ins. Within a volcanological context, there are currently two such plug-ins under active development. The first is for analysing FTIR spectra, and the second is for performing real-time estimates of SO₂ emissions using UV spectrometers.

The FTIR plug-in aims to automate the background subtraction tasks which are currently performed manually. Very early versions of the plug-in were used in the study conducted by Iacovino et al. [2014] and development work continues to create a more advanced and user-friendly tool [Iacovino et al., 2013].

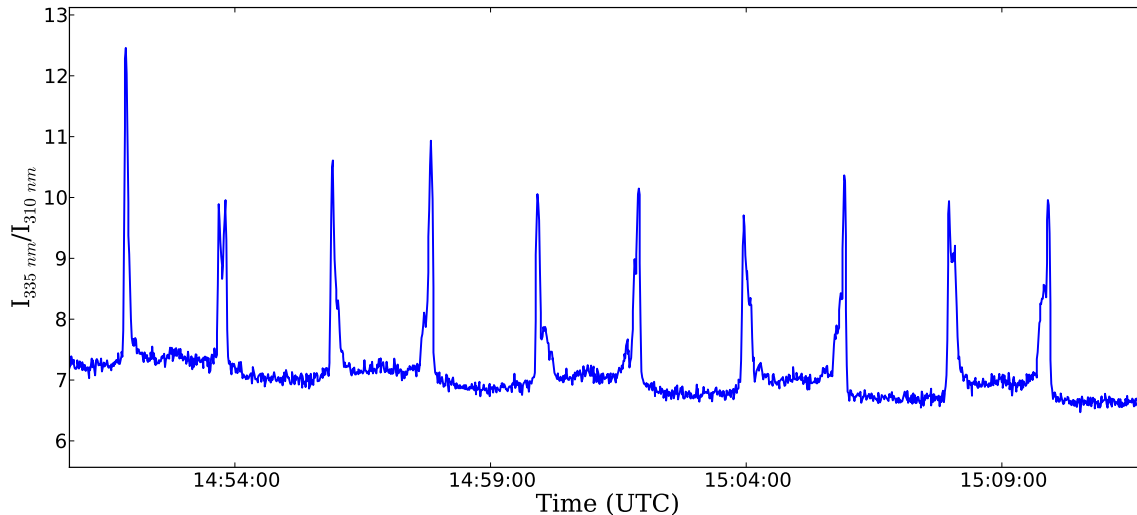


Figure 3.2: Plot produced using the AvoPlot SO₂ plug-in to visualise UV spectra collected with a scanning instrument at Villarrica volcano in February 2012. The peaks correspond to in-plume measurements as the spectrometer is scanned back and forth in a transect of the plume.

The SO₂ emission plug-in is designed to provide a faster and more advanced replacement for the Vispect software [Wright, 2008], which is currently the “standard” tool used by volcanologists for UV spectroscopy in the field. The principal of this software is to provide real-time estimations of the column amount of SO₂ in the field of view of the spectrometer, thus enabling researchers to rapidly assess the data they are collecting. Such a tool is vital for effective data collection, since it is otherwise impossible to tell if the field of view of the spectrometer is intersecting the plume. This is especially true for data collected during traverses beneath the plume [e.g. McGonigle, 2002], and for scanning units such as those described in Section 3.2. Vispect achieves this by plotting a ratio of measured intensities at wavelengths outside and inside an absorption band of SO₂ (typically 335 nm and 310 nm respectively), a peak in the ratio represents increased amounts of SO₂. Although Vispect is a useful tool and has been widely adopted by researchers around the world, it has several key limitations. The procedures it uses for loading spectral data are extremely slow, making the assessment of large data sets impossible. Furthermore, the approach used to detect newly written spectrum files is flawed, and causes the program to crash once more than a few thousand spectra have been collected. The current implementation of the AvoPlot plug-in offers the same functionality as Vispect (Fig. 3.2), but uses optimised spectrum loading routines which can run concurrently on multiple CPUs, resulting in processing times that are over fifty times faster than those of Vispect (even on a single-core CPU). System-level directory-watching utilities (in-

otify in Linux and ReadDirectoryChangesW from the native API in Windows) are used to detect newly created spectrum files, ensuring fast, efficient detection that scales to any number of spectra. The plug-in has been used extensively during field campaigns on Erebus as well as during spectroscopic studies of volcanoes in Costa Rica [Moussallam et al., 2014b], Chile (unpublished) and Mexico [Cassidy et al., 2014].

In addition to the studies making use of these specific plug-ins, the main AvoPlot program itself has also been used in several projects. Its fitting functions, have been used for performing spectrometer calibrations [Section 5.2.2, Peters et al., 2014b] and for analysing sulphur data [Iacovino, 2014], and its general plotting capabilities have been used to produce many of the figures in this dissertation.

3.2 Portable Spectrometer Scanners

3.2.1 Introduction

SO₂ flux is an important parameter in volcanic monitoring and is commonly measured using UV spectrometers. In order to calculate flux, spectra must be collected across a full transect of the plume perpendicular to its transport direction. For horizontally drifting plumes, this is often achieved by carrying the spectrometer (with its field of view at zenith) in a traverse beneath the plume [e.g. McGonigle, 2002]. However, this technique requires there to be an unobstructed path beneath the plume, and cannot be used for vertically rising plumes. In these situations scanning units are often used instead [e.g. McGonigle, 2007]. Although different designs for scanning units exist, their basic operation is the same; a stepper motor is used to rotate the the optical axis of the spectrometer's field of view such that spectra can be collected across a full transect of the plume.

Recently, much emphasis has been put on developing scanning units for permanent installation around volcanoes [e.g. Salerno et al., 2009, Edmonds et al., 2003]. As such, the scanners themselves tend to be large, heavy and require an external power supply. This makes them unsuitable for studies at inaccessible volcanoes where equipment must be carried on foot. The scanning units presented here were specifically designed with this in mind and as a result are light, cheap and low-power.

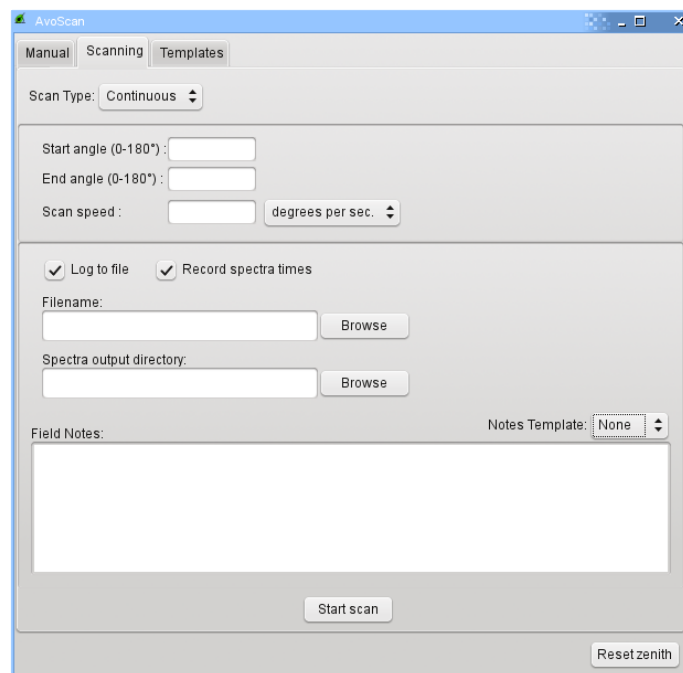


Figure 3.3: Screen-shot of the main interface window for the scanner control program.

3.2.2 Hardware and Software

The software for the scanners is written in Python, using wxPython for the user-interface. It is split into three main components: (i) the control program for the scanners, (ii) a script for assigning angles to spectrum files and (iii) `ica_inspect` – a graphical program for calculating fluxes from processed spectral data. All the software is available open-source under the terms of Gnu Public License from <http://code.google.com/p/avoscan/>.

Figure 3.3 shows a screen-shot of the main interface window of the control program for the scanners. Start- and end-angles for scanning are set relative to a user defined zenith. For vertical scans, this should usually be straight-upwards, which can be obtained accurately using a spirit-level placed on the top of the spectrometer’s telescope. Two types of scan are possible, “continuous” in which the stepper motor is always in motion and “stepped” in which the stepper pauses for a user-defined amount of time at a certain number of increments between the start- and end-angles. In both cases the stepper reverses direction at the end points of the scan. Although this introduces a significant error into the recorded angles (due to the slack in the gearbox), it does not affect the accuracy of SO_2 flux calculations (see Section 3.2.3) and is a necessary compromise to avoid having to use a mirror for scanning. In addition to setting scan parameters, the control program allows field notes to be

recorded in the header data of the angle-versus-time file, ensuring that the notes do not become separated from the data to which they refer.

The `ica.inspect` program was the original basis for the AvoPlot software [Section 3.1, Peters, 2014] and has also been used, in a slightly modified form, for processing XANES (X-ray Absorption Near Edge Structure) data [Moussallam et al., 2014a]. With respect to the scanning units, it is used to calculate fluxes from the processed spectral data. Note that it does not perform the actual SO₂ column amount retrievals, that must be done separately (see Section 5.2.2 for a description of the retrieval process). Rather, `ica.inspect` takes the retrieved SO₂ column amounts and their corresponding angles and integrates them (see Eq. 3.2 below) to give a flux for each complete scan. A key step in this process is the subtraction of the background (i.e. the out-of-plume) SO₂ column amount. The distinction between in-plume and out-of-plume regions is estimated by fitting a Gaussian to the data from each individual scan. Out-of-plume column amounts are taken to be any that are more than three standard-deviations from the mean of the Gaussian fit. Although this gives a reasonable estimate, some manual adjustment of the bounds is usually required. The background is then approximated by a linear fit through the out-of-plume data. However, it is common for these data to contain many outliers, for example caused by the ground entering the field of view of the spectrometer at the extrema of the scan, and these must be removed so as not to skew the background estimation. The background is therefore calculated using an iterative approach; an initial linear fit is made through all the data, points that could not be fitted within their associated error (where the error is determined by the retrieval software) are identified and the furthest outlier is removed from the fit, the process is then repeated until all remaining points can be fitted within error. Despite the simplicity of this approach, it has been found to produce very robust background estimates, even when the data are exceptionally noisy.

The main hardware components of the scanning units are shown in Fig. 3.4. Even at fast scanning speeds, power consumption is sufficiently low that the scanners can be powered via their USB interface. Since the majority of spectrometers used for measuring volcanic SO₂ are also USB-powered, this is a huge advantage; removing the need to carry heavy batteries into the field. The power supply board includes reverse-polarity protection (as described in Section 2.2.3), with a standard fuse providing over-current protection. The stepper-motor and controller are standard components produced by Phidgets (part numbers 3319_1 and 1063_1 respectively). It should be

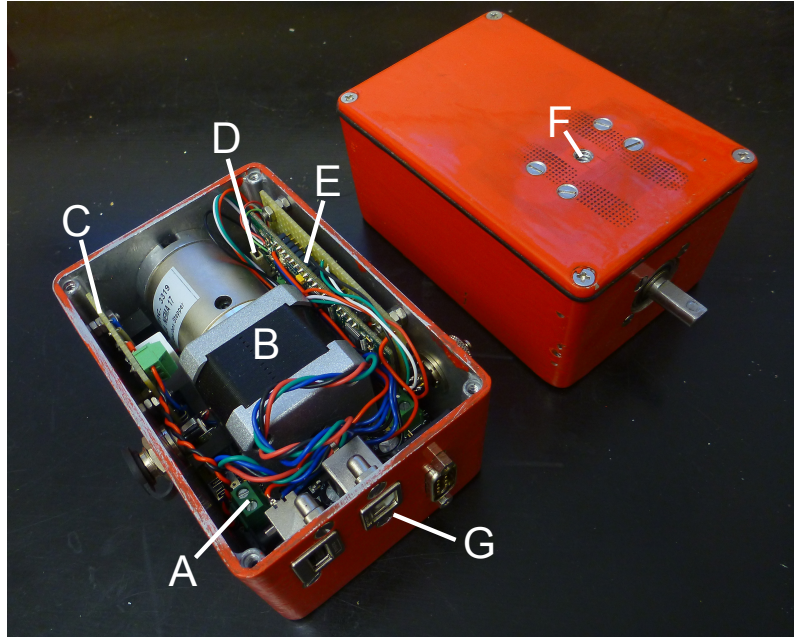


Figure 3.4: Photograph showing the key hardware components of the scanning units: (A) Phidgets 1063.1 stepper controller, (B) Phidgets 3319.1 stepper motor, (C) Power supply (5–12 V DCDC converter, reverse polarity and over-current protection), (D) CMPS10 tilt-compensated compass, (E) FT-MOD-4232HUB USB-Serial hub, (F) Tripod mount, (G) Waterproof USB ports.

noted that although these components do not have an extended operating temperature range, the scanners have been used, without fault, for many hours at -30°C during field campaigns on Erebus. The FT-MOD-4232HUB USB-Serial hub is used to provide additional USB-host ports on the scanner which can be used, for example, for connecting the spectrometer. It also provides four serial ports. One of these is exposed on the back of the scanner to allow a handheld GPS unit to be attached for accurate time-keeping and automatic location logging (although this is not yet supported by the software). Another is exposed to allow connection of a web-camera which could collect a visual record of each scan, allowing rapid assessment of plume conditions in post-processing (also not yet supported by the software). A serial port is also used to connect a three-axis, tilt-compensated CMPS10 electronic compass. This allows the software to automatically record the angle from horizontal that the scan was made at (for horizontal scans), and the bearing of the scan plane (for vertical scans). All the electronics are sealed in a waterproof box, and waterproof connectors are used to ensure that dust, ash or moisture cannot enter.

3.2.3 Measuring SO₂ Flux

Scans are made by mounting a telescope (coupled to the spectrometer by an optical-fibre) to the scanner. The spectrometer records continuously (the control software for the spectrometer is independent of that of the scanner) as the scanner rotates back and forth. Angles are assigned to each spectrum in post-processing using their timestamps and an angle-versus-time log file created by the scanning software. The angle (θ_τ) associated with a spectrum captured at time τ is given by:

$$\theta_\tau = \theta_0 + (\tau - \tau_0) \cdot \frac{d\theta}{dt} \quad (3.1)$$

where $\frac{d\theta}{dt}$ is the angular velocity of the scanner, τ_0 is the time record closest to τ in the angle-versus-time log file and θ_0 is the corresponding angle.

Using the `ica_inspect` program, processed spectra are split into individual scans based on their corresponding angles and each scan is manually divided into in-plume and out-of-plume regions. A linear fit through the out-of-plume regions is used as an estimate of the background and subtracted from the scan. SO₂ flux (Φ) is then calculated using the standard scanning DOAS integration method [e.g. Salerno et al., 2009]. For a scan containing n spectra, the flux in tonnes per day is given by:

$$\Phi = \kappa v \sum_{i=0}^{n-1} r (\theta_{i+1} - \theta_i) \cdot \frac{A_i + A_{i+1}}{2} \cos \alpha \quad (3.2)$$

where κ is the conversion factor from ppm m³ s⁻¹ to tonnes per day (2.3×10^{-4}), v is the plume transport speed perpendicular to the scan direction, r is the distance from the spectrometer to the plume, A_i is the SO₂ column amount recorded at scan angle θ_i and α is the inclination angle of the scan from horizontal.

The stepper motor in the scanners has a 99:1 planetary gearbox, giving it an accuracy of $\pm 0.01^\circ$. Note that errors due to crash-back in the gearbox are systematic for a single scan, and therefore do not affect the integrated column amount. However, the precision of the timestamps in the spectrum files (1 second) does have an effect on the accuracy of the angles. Using Equation 3.1 and the standard error propagation equation [e.g. Boas, 1983a] the error in the angle (δ_{θ_τ}) of a spectrum recorded at time τ can be calculated by:

$$\delta_{\theta_\tau} = |\theta_\tau| \cdot \sqrt{\delta_\theta^2 + \left((\tau - \tau_0) \cdot \frac{d\theta}{dt} \right)^2 \cdot \left(2\delta_\theta^2 + \frac{\delta_\tau^2}{(\tau - \tau_0)^2} \right)} \quad (3.3)$$

where $\delta_\theta = 0.01^\circ$ is the uncertainty in the angle of the stepper motor and $\delta_\tau = 1$ s is the uncertainty in the capture time of the spectrum.

Error in the retrieved SO₂ column amount is usually estimated by the retrieval software by analysing the residual from the fitting of the reference and Ring spectra. Propagating these errors along with those in the angles through Equation 3.2 gives the following as an estimate of the error in the flux (δ_Φ):

$$\delta_\Phi^2 = \Phi^2 \left[\left(\frac{\kappa v \delta_{ICA}}{\Phi} \right)^2 + \left(\frac{\delta_v}{v} \right)^2 \right] \quad (3.4)$$

where $\delta_v = 0.3 \text{ m s}^{-1}$ is the uncertainty in the plume rise speed and δ_{ICA} is the error in the integrated column amount given by:

$$\delta_{ICA}^2 = \sum_{i=0}^{n-1} A_i^2 \left[\left(\frac{\sqrt{\delta_{\theta_i}^2 + \delta_{\theta_{i+1}}^2}}{\theta_{i+1} - \theta_i} \right)^2 + \left(\frac{\sqrt{\delta_{A_i}^2 + \delta_{A_{i+1}}^2}}{A_{i+1} + A_i} \right)^2 \right] \quad (3.5)$$

As can be seen in Figure 3.5, the resulting errors are rather large (in the order of $\pm 50\%$). The error is dominated by the uncertainty in the angle for each spectrum, which is large due to the single second precision of the timestamps used in the spectrum files. Improvements in the software have since resolved this issue by using the same directory watching code as AvoPlot (Section 3.1.4) to achieve millisecond precision.

3.2.4 Results

Figure 3.5 shows a comparison of SO₂ fluxes recorded at Villarrica volcano in February 2012 using the scanning units described above, a UV camera and pedestrian traverses beneath the plume. The data shows that despite the very different time resolutions of the three techniques, the calculated fluxes are comparable. These data were collected as part of a study into using UV spectrometers to calibrate images from UV cameras. Unfortunately, the same methodology was developed independently by Lübcke et al. [2013] and so the study was abandoned. However, the scanning units have since been used during several field campaigns on Erebus and studies at Turrialba volcano in Costa Rica [Moussallam et al., 2014b] and Colima volcano in Mexico [Cassidy et al., 2014].

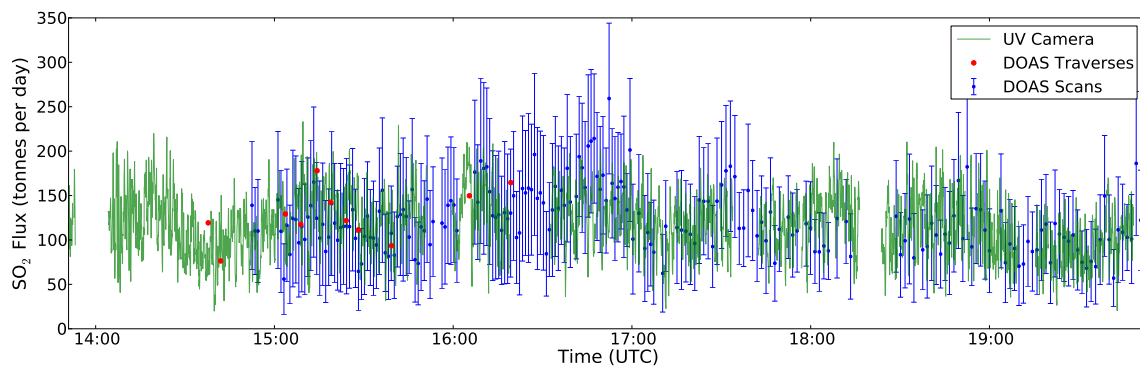


Figure 3.5: SO_2 flux data from Villarrica volcano, collected on 10 February 2012. The data show a comparison of the SO_2 fluxes calculated from UV camera images, UV spectrometer scans (DOAS scans) and UV spectrometer pedestrian traverses (DOAS traverses).

Chapter 4

Decadal Persistence of Cycles in Lava Lake Motion

The work presented in this chapter was undertaken in order to meet the “Assessment of Annual Variability of the Lava Lake Cycles” research objective of this study (Section 1.7.2). Although previous studies of Erebus volcano’s active lava lake have shown that many of its observable properties (gas composition, surface motion and radiant heat output) exhibit cyclic behaviour with a period of ~ 10 min, they have typically focused on short data sets (a few hours). Subsequently, little is known about the longer-term behaviour of these cycles. In this chapter we investigate the multi-year progression of the cycles in surface motion of the lake using an extended (but intermittent) dataset of thermal infrared images collected between 2004 and 2011. Cycles with a period of ~ 5 –18 min are found to be a persistent feature of the lake’s behaviour and no obvious long-term change is observed despite variations in lake level and surface area. The times at which gas bubbles arrive at the lake’s surface are found to be random with respect to the phase of the motion cycles, suggesting that the remarkable behaviour of the lake is governed by magma exchange rather than an intermittent flux of gases from the underlying magma reservoir.

The majority of content from this chapter has been published as: Peters, Nial, Clive Oppenheimer, Philip Kyle, and Nick Kingsbury. Decadal Persistence of Cycles in Lava Lake Motion at Erebus Volcano, Antarctica. *Earth and Planetary Science Letters* 395 (June 1, 2014): 1–12.

All content of this chapter was created by me, and the role of the co-authors did not extend beyond that of normal supervision. Terrestrial laser scan data were collected and pre-processed by Jed Frechette, Laura Jones and Drea Rae Killingsworth. However, subsequent calculation of lake surface areas were performed by me. Computer codes implementing the motion estimation algorithm were provided by Prof. Nick Kingsbury, but all other code was created by me. My implementation of the Morlet wavelet transform was, however, closely based on code provided by Marie Boichu.

4.1 Introduction

As discussed in Section 1.3, many of the properties of the Erebus lava lake exhibit a pronounced pulsatory behaviour. Oppenheimer et al. [2009] observed that the radiative heat loss, surface velocity and certain magmatic gas ratios all oscillated with a period of ~ 10 min. The cycles appeared to be phase locked with each other, suggesting a common mechanism was responsible for the oscillations in each property. Evidence of similar cyclicity has been observed in the SO_2 flux [Boichu et al., 2010] and this is explored in more detail in Chapter 5. Fluctuations in the H_2/SO_2 ratio have also been measured [Moussallam et al., 2012], but these have yet to be linked definitively to the cycles observed by Oppenheimer et al. [2009].

One possible explanation for the observed behaviour is pulsatory exchange flow of hot, degassing magma into the lake from the subjacent conduit. It has been shown experimentally that given two liquids flowing in opposite directions in a vertical pipe (for example driven by a density difference between them), under certain flow conditions an instability occurs which results in a pulsed flow [Huppert and Hallworth, 2007]. Oppenheimer et al. [2009] suggested that such behaviour may explain the cycles at Erebus volcano, with bubbly and degassing, low density magma rising up the conduit into the lake whilst degassed, denser magma sinks back down the conduit again. The resulting pulsatory flow delivers packets of fresh magma into the lake quasi-periodically, giving rise to the observed cycles in lake properties. The period of the cycles would be expected to reflect the rheological properties and velocity of the bubbly flow and geometry of the conduit.

The previous studies at Erebus have analysed only very short time-series of data (circa 1 h), and no investigation of the long-term behaviour of the cycles has yet been conducted. However, thermal infrared (IR) images of the Erebus lava lake have been collected almost every year since 2004 during the Mount Erebus Volcano Observatory's annual austral summer field campaigns. Using a similar technique to that of Oppenheimer et al. [2009], we have extracted mean surface speed estimates from the usable portions of the now substantial IR dataset. Using the mean surface speed as a proxy to assess the cyclicity of the lake motion, we present an overview of its behaviour between 2004 and 2011 and compare this to visible changes in the lake's appearance. Using a dataset recorded at higher time resolution in 2010, we identify times when bubbles arrive at the surface of the lake and compare this to the phase of the cycles.

4.2 Methodology

Fieldwork on Erebus volcano is limited to the austral summer, and typically takes place from late-November to early January. Where we refer to a field season by year, we are referring to the year in which it began. The logistics involved in reaching the crater rim, combined with frequent bad weather conspire to limit the interval of IR image data acquisition to a few weeks each year. The intervals of useful data are further reduced due to fluctuations in the IR transmission between camera and lava lake. When the gas/aerosol plume is highly condensed (high relative humidity) the IR transmission in the camera waveband is poor and the images of the lake are of unusable quality. The latest IR camera system, which was deployed in December 2012, is capable of year-round operation (dependent on power) [Chapter 2, Peters et al., 2014c]. The data from this fully automated system was not available at the time of this investigation, but is analysed in Chapter 5.

4.2.1 Camera Hardware

All IR images of the Erebus lava lake used in this chapter were recorded by tripod-mounted camera systems installed at the Shackleton's cairn site on the northern side of the Main Crater (Fig. 4.1). Three different IR camera systems have been used on Erebus since 2004 (summarised in Table 4.1). The first of these was an Agema Thermovision 550 mid-infrared (3–5 μm) camera, as described by Oppenheimer et al. [2004], which acquired images with a 4 s time-step. The second was a FLIR P25 camera equipped with a 72 mm IR lens. This camera has an uncooled 320 \times 240 element detector with a waveband of 7.5–13 μm and a spatial resolution (instantaneous field of view) of 0.31 mrad. The low temperatures at the crater rim of Erebus severely impacted the P25's ability to write images to its compact flash card, and as a result the interval between successive images varies between 8 and 20 s. The most recent IR camera model we have employed is a FLIR SC645, with an uncooled 640 \times 480 element detector, waveband of 7.5–13 μm , and a spatial resolution of 0.69 mrad. Although the SC645 is capable of frame rates of up to 25 Hz, we have typically acquired images at 2 s intervals. It was, however, operated with a 0.5 s time-step in acquisitions for a part of the 2010 field season and we have used these higher time resolution data for bubble event analysis (Section 4.2.5).

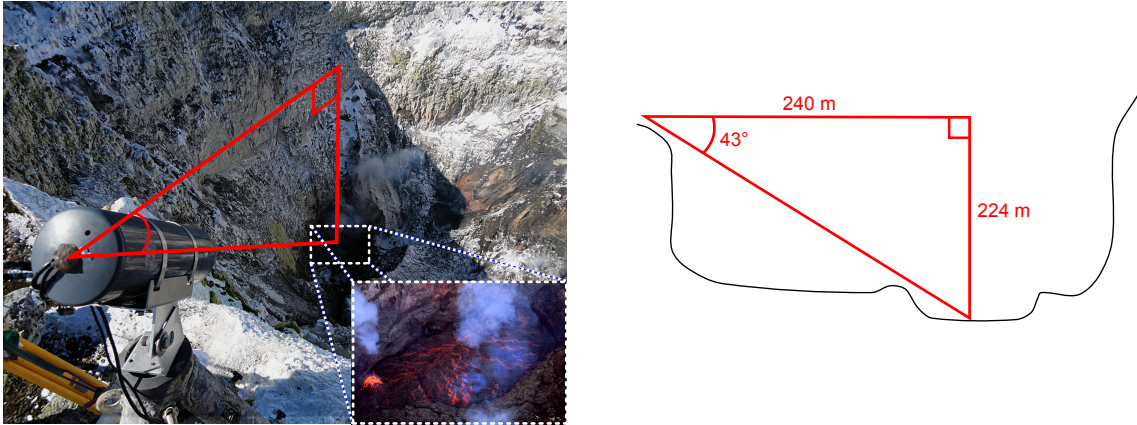


Figure 4.1: Photograph showing the IR camera setup on the crater rim of Erebus and cartoon showing the viewing geometry of the lake (calculated from TLS data).

Year	IR Camera	Waveband (μm)	Capture Rate (Hz)
2004	AGEMA	3 - 5	0.25
2005	No data collected	-	-
2006 - 2009	FLIR P25	7.5 - 13	0.125 - 0.05
2010 - 2011	FLIR P25 and FLIR SC645	7.5 - 13	0.125 - 0.05 and 0.5
2011 - 2014	FLIR SC645	7.5 - 13	0.5

Table 4.1: IR camera systems used at Erebus volcano by year.

4.2.2 Data Selection

Interruptions to the recording of IR images on Erebus are common. The Agema and P25 cameras both required their memory cards to be changed regularly and equipment failure was frequent due to the harsh operating conditions. These factors have resulted in a segmented data set with many gaps. The first step in data selection was to split the data into groups of continuous acquisition that contained no two images more than 40 s apart. Groups spanning less than one hour of acquisition were discarded. Subsequent data processing was performed on a per group basis.

High winds at the summit of Erebus cause camera shake, potentially introducing large errors into the velocity estimates calculated by the motion tracking algorithm. This problem is particularly acute in data from the Agema and P25 cameras, which did not have such stable tripod mounts as does the new SC645 system. Attempted stabilisation of the images in post-processing failed due to the lack of distinctive stationary features in the images. Instead, a simpler approach was followed, in which only periods of data with little or no camera shake were analysed. Due to the large volume of available data, an automated routine for identifying such periods was

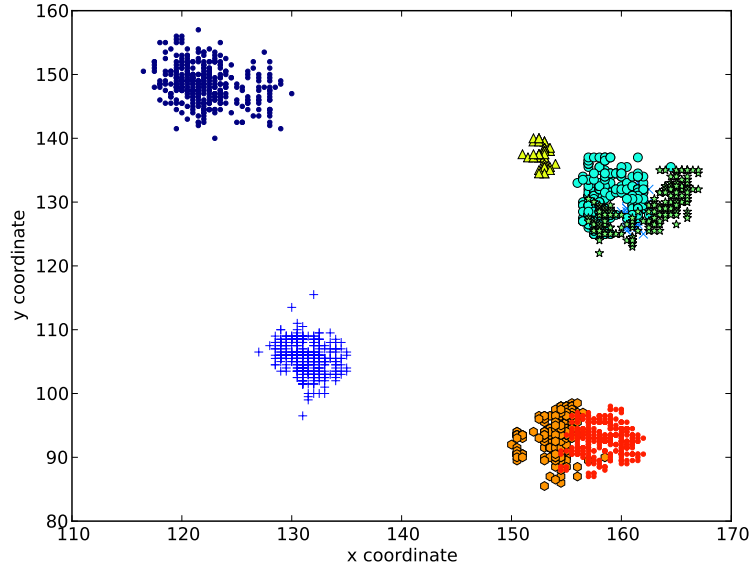


Figure 4.2: Positions (in pixels) of the lake bounding box within images from 2010 showing their assignment into clusters. The scatter (standard deviation) of points within one cluster is used as an indicator of camera shake. Only images assigned to clusters with a standard deviation of less than 1.0 were used for surface motion estimation.

developed. This involved first defining the bounding box of the lake in each image by thresholding the image at a predetermined level, and identifying the non-zero region. Images in which the bounding box could not be found, or was unusually small were rejected, as these characteristics point to poor visibility of the lake (typically caused by high relative humidity, blowing snow, or rime-ice accumulation on the lens). The centre coordinates of the bounding boxes were then assigned to clusters using SciPy’s *fclusterdata* function [Jones et al., 2001]. To reduce the run time of the clustering algorithm, duplicate bounding box positions were discarded before clusters were computed. Using the standard deviation of the bounding box coordinates in each cluster as an indicator of camera shake, the best clusters for each year (typically with a standard deviation of < 1.0 pixels) were selected (Fig. 4.2). As a final check of data quality, the images in each cluster were compiled into a video, which was then viewed to ensure good visibility of the lake and minimal camera shake throughout.

4.2.3 Motion Tracking

The steps involved in obtaining a time-series of mean lake surface speed from a set of IR images are shown in Fig. 4.3 and are described in detail below.

Since the focal plane of the thermal camera is not parallel to the surface of the lava lake, perspective effects mean that each pixel in the image represents a different distance in the plane of the lake. To correct for this distortion, each image was rectified before the motion tracking was carried out. The required transformation was calculated by matching points in the image to points in a terrestrial laser scan of the lake. OpenCV's [Bradski, 2000] *cvFindHomography* function was then used to calculate the required transformation matrix, and the *cvWarpPerspective* function used to apply it (see Bradski and Kaehler [2008]). Correcting the images in this way also accounts for any lens distortion. Terrestrial laser scan data of the lava lake were only available for 2008 onwards. For thermal images from earlier years, the homography matrix was calculated from the viewing angle of the camera and the size of the lake (which had been estimated with a handheld laser range finder). Although this method neglects lens distortion, we expect the effects to have little impact on the results obtained.

The significant temperature contrast between the lake and the surrounding crater causes problems for the feature tracking algorithm. As the strongest feature in the image, the lake boundary tends to dominate over the structure within the lake that we are actually interested in. This issue can be overcome by masking the regions outside of the lake with Gaussian-distributed white noise with a mean and variance similar to that of the pixels within the lake. Random noise is used rather than a fixed value to prevent the output of the bandpass filters used in the wavelet decomposition from being exactly zero, as this causes the algorithm to fail.

The feature tracking algorithm itself is based on the Dual-Tree Complex Wavelet Transform (DT-CWT) [Kingsbury, 2001]. Unlike the widely used Discrete Wavelet Transform (DWT) (see for example Polikar [2010]), DT-CWT is approximately shift invariant, meaning that shifts in input signal do not cause changes in energy distribution between wavelet coefficients at different scales. Instead, it is found that shifts in the input signal manifest themselves as a phase shift between the wavelet coefficients. By decomposing each frame in a series of images using the DT-CWT and comparing the phase shifts between the subimages, it is possible to estimate the displacement field that maps features in one frame to the next. The estimate

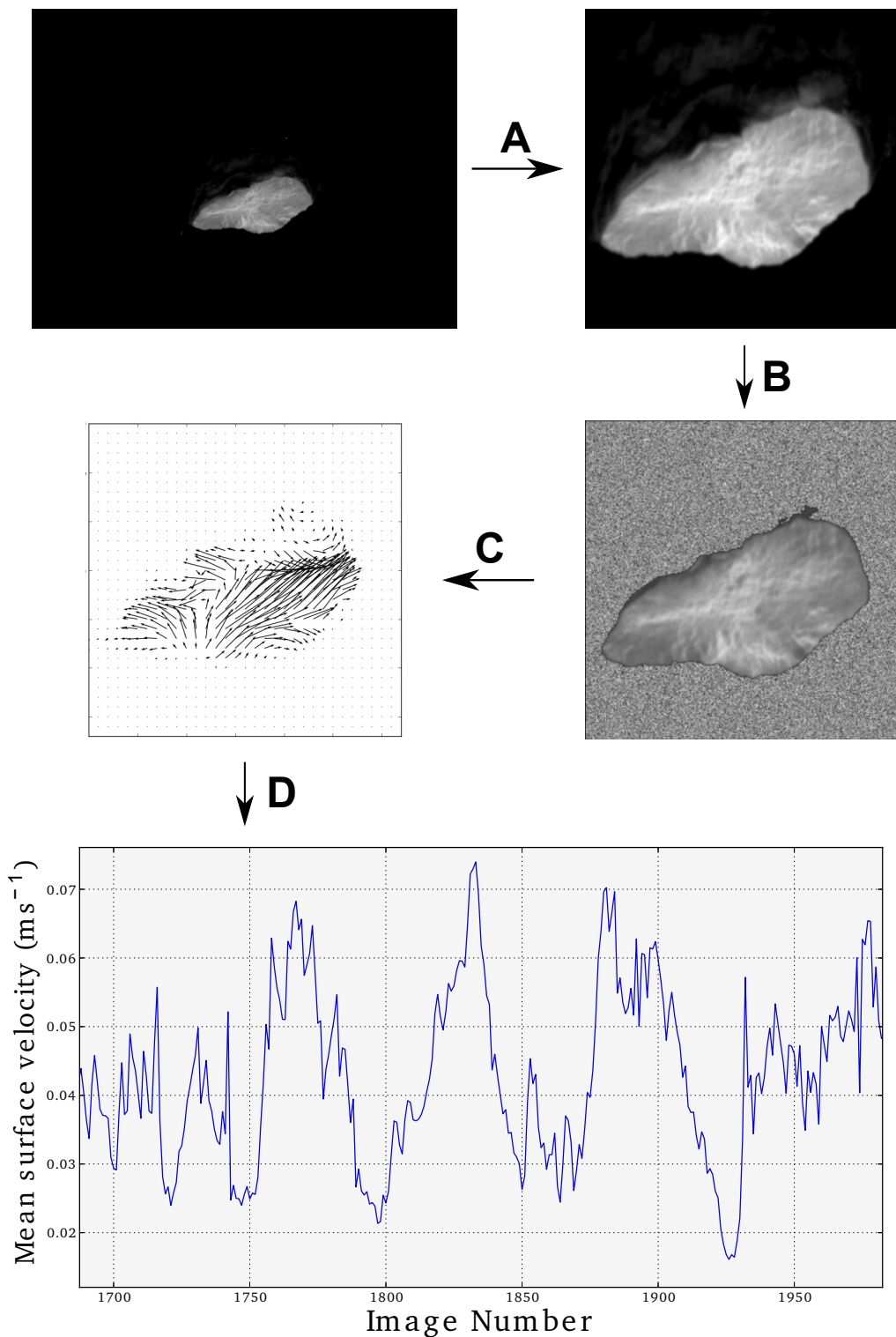


Figure 4.3: Flow diagram showing the steps in extracting mean surface velocity from IR images. A) Perspective correction to account for viewing angle of camera. B) Random noise masking to reduce contrast between lake and surroundings. C) DT-CWT feature tracking estimates motion vectors between consecutive frames by calculating phase shift between complex wavelet coefficients. D) Mean velocity found by averaging motion vectors in the central region of the lake.

is first made at a coarse level of decomposition, with subsequent estimates made at finer levels so as to refine the result [Magarey and Kingsbury, 1998]. Oppenheimer et al. [2009] tuned the method specifically for working with IR images from Erebus volcano, and we adopted the same parameters for the motion estimation reported here. The algorithm was verified by passing in sets of two identical images, one of which was shifted by a known amount and checking that the shift was correctly detected. Further verification was achieved by comparing velocity estimates obtained from the algorithm with visual estimates found by counting pixels.

Finally, the mean surface speed of the lake was found by averaging the magnitudes of the computed velocity vectors. To avoid possible edge effects, only velocity vectors from the central region (at least 3 pixels inside the lake boundary) of the lake were included in the averaging.

An animation showing results of the motion tracking methodology described above (from rectified images to mean lake speed) is provided in the supplementary material for the electronic version of Peters et al. [2014d].

4.2.4 Time-Series Analysis

The Fourier Transform is a popular tool for evaluating frequency components in time series data. Although it has perfect frequency resolution, it does not provide any time resolution and is therefore not suitable for evaluating non-stationary signals. It is possible to achieve some time resolution by splitting the signal under analysis into windows of fixed length and applying a Fourier Transform to each window. However, the choice of window length is critical since although short windows provide better time resolution, they also inhibit the frequency resolution of the Fourier Transform. Wavelet transforms partially solve this resolution problem by using a variable length window to achieve higher frequency resolution at low frequencies, and higher time resolution at high frequencies. This is desirable, since high frequency components tend to be short-lived in “real world” signals. Referred to as “Multi-Resolution Analysis”, this approach makes wavelet transforms particularly suitable for assessing the time-frequency structure of non-stationary signals. An excellent summary of wavelet transforms is given by Polikar [2010].

As can be seen in Fig. 4.4e, the mean surface speed time-series obtained are highly non-stationary. To evaluate the periodic components of the series with time, we

therefore use a Morlet wavelet transform to produce spectrograms of the data. Our implementation of the Morlet transform is the same as that of Boichu et al. [2010]. The mean speed data were interpolated to a uniform 1 s time step prior to the Morlet transform using simple linear interpolation.

As illustrated by Figs. 4.4a and 4.4b, some of the ~ 5 –18 min cycles are of much greater amplitude than others, and will result in a very high modulus in the Morlet transform. Longer time-series tend to exacerbate this problem, since they often contain at least a few very high amplitude oscillations, which then saturate the colour scale and mask much of the other detail. In this way, the cyclicity of the lake may not be apparent even if it exists. However, creating a spectrogram of just the data from the “non-cyclic” time period, reveals that there are indeed still ~ 5 –18 min period components present – they are simply of lower amplitude.

4.2.5 Bubbles

Bubbles breaking the surface of the lake manifest themselves as sharp peaks in the mean surface speed time-series. The poor time resolution of the Agema and P25 datasets mean that most bubbles are not recorded. However, much of the SC645 data from 2010 was recorded at 2 Hz, which is more than sufficient to capture the arrival of bubbles at the surface.

Bubble events were located in time by comparing the mean speed time-series to a low-pass filtered copy of itself. Bubbles were classified as events where the speed was greater than 1.2 standard deviations above the low-pass filtered value. The value of 1.2 was chosen by comparing bubble events detected by the algorithm to those located manually in a test set of data spanning three hours. The analysis was conducted on a continuous time-series of good quality data from 24 December 2010, spanning approximately 13 h. By visually inspecting the IR images corresponding to each of the bubble events, we determined that all events were small (metre-scale, with no ejection of material from the lake).

The bubble events detected are uniformly distributed in time. However, this tells us nothing of how they are related to the pulsatory behaviour of the lake. What is of real interest is how bubble events relate to the phase of the speed cycles; for example, do more bubbles surface during periods of fast surface movement? In order to evaluate a possible relationship between the cyclicity and bubble events we use

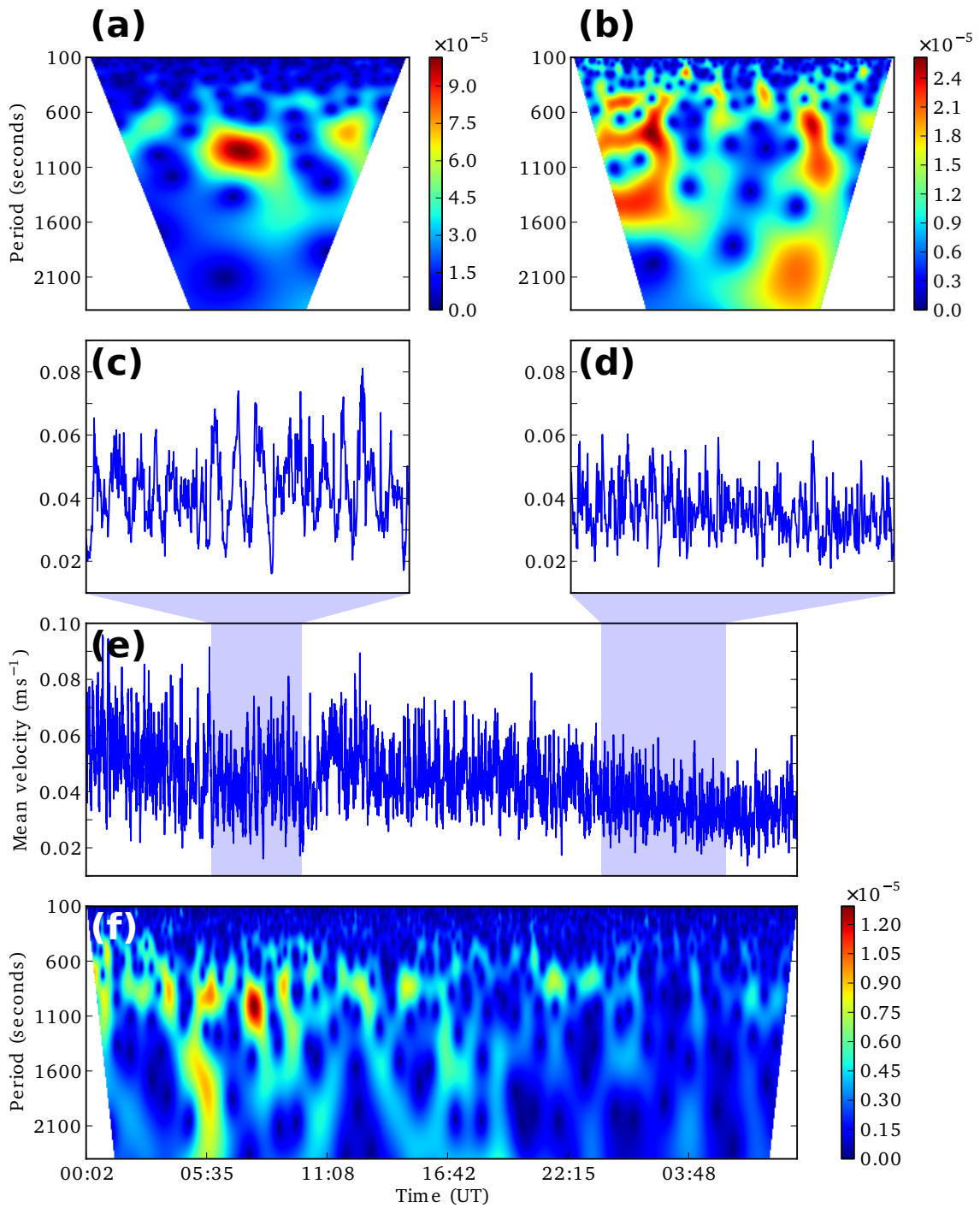


Figure 4.4: (e) Selection of mean surface velocity data from December 2010 and (f) the corresponding Morlet wavelet transform showing the periodicities present. (c, d) Expanded sections of the time series showing how an increase in period is accompanied by an increase in amplitude. (a, b) Morlet wavelet transforms of the expanded sections showing evidence of periodicity even when it is not clearly present in Morlet transform of the full time series (f). The colour scales represent the Morlet transform modulus.

the method of delays (e.g. Kantz and Schreiber [2003]) to reconstruct our time-series data into a phase space representation. If the bubble events are somehow correlated to the phase of the speed cycles then we argue that their distribution in phase space will differ from that of a random sample taken from the time-series. We can imagine this as being due to a clustering of bubble events at certain positions in phase space.

A clear description of the method of delays for phase space reconstruction is given by Kantz and Schreiber [2003] and also by Richter and Schreiber [1998]. We will therefore not attempt to describe the technique in any detail here, instead we give the specifics of how the parameters required for delay reconstruction were calculated for our time-series. Essentially, phase space reconstruction of a time-series involves mapping each sample in the series to a vector in phase space. For a scalar time-series x_1, x_2, x_3, \dots the method of delays can be used to calculate the corresponding phase space vectors $\mathbf{x}_n = (x_n, x_{n-l}, x_{n-2l}, \dots, x_{n-(d-1)l})$ where l is known as the lag, and d is the embedding dimension. Figure 4.5 shows an example of phase space reconstruction using the method of delays with an embedding dimension of 2, and demonstrates how points in the time-series are mapped into phase space.

Careful selection of both the lag and the embedding dimension is of paramount importance to obtain an effective phase space reconstruction of the original time-series. Estimation of a suitable lag for our data was performed using two different techniques. The first involved calculation of the autocorrelation function of the time-series. The time required for the autocorrelation function to decay by a factor of e is stated as being a reasonable estimate for the lag [Kantz and Schreiber, 2003]. For our data, this gave a lag of 142 s. A second technique for lag estimation, also described by Kantz and Schreiber [2003], is to find the minimum of the mutual information of the time-series. We calculated the mutual information of our time-series using the TISEAN software package [Hegger et al., 1998], and found the minimum to be at 200 s. We repeated our bubble event analysis for several different values of lag between these two estimates and found no appreciable difference in the results. The results presented here are from the analysis using a lag of 150 s.

To determine a good embedding dimension, we followed the approach proposed by Hegger and Kantz [1999], in which the false nearest neighbour method [Kennel et al., 1992] is combined with surrogate data tests. The false nearest neighbour method compares the ratio of distances between points and their nearest neighbours between an embedding dimension of n and $n+1$. If the ratio is greater than a threshold (s),

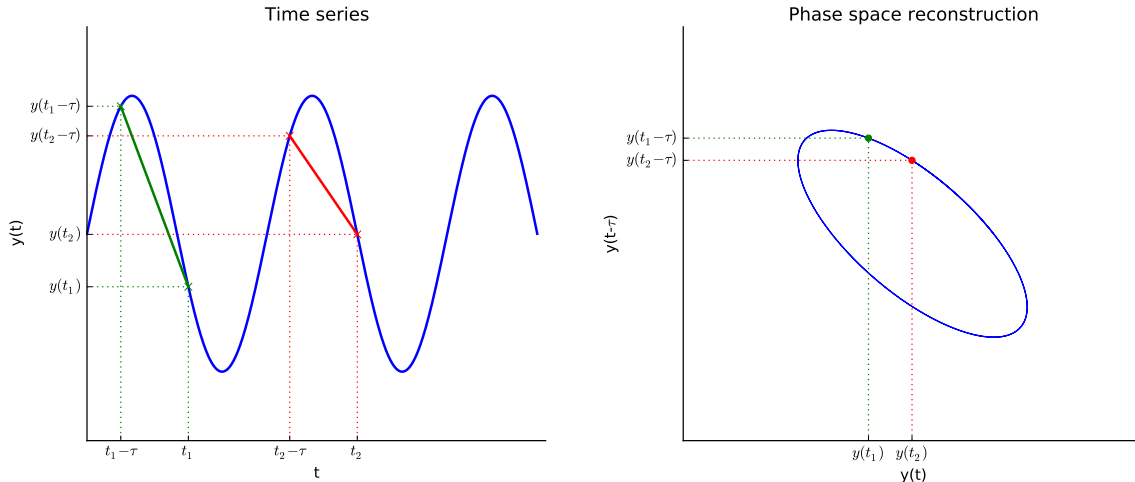


Figure 4.5: Phase space reconstruction of a simple time-series using the method of delays. The original time-series is shown in the left hand plot and the phase space reconstruction using a lag of τ and an embedding dimension of 2 is shown in the right hand plot. Samples from the time-series (e.g. t_1 and t_2) are mapped to phase space by plotting them against the value of the time-series one lag prior to their sample time.

the points are said to be “false neighbours”. A high percentage of false nearest neighbours is indicative of too low a choice for the embedding dimension. The TISEAN software package was used both for the calculation of false nearest neighbours and for the creation of surrogate data [Schreiber and Schmitz, 1999]. Figure 4.6 shows the calculated percentage of false nearest neighbours for different embedding dimensions and thresholds. There is a clear difference in behaviour between the real data and the surrogate data. This indicates that the loss of false neighbours as we move to higher embedding dimensions is not simply due to linear correlations in the data. Furthermore, we can see that, for an embedding dimension of 4, the percentage of false nearest neighbours falls away very rapidly for low threshold values. We therefore used 4 as our embedding dimension when performing the phase space reconstruction. The data were low-pass filtered prior to phase space reconstruction to remove noise and the spikes due to bubbles.

The time-series analysed contains 141 bubble events (Fig. 4.7). We compared the cumulative distribution function (CDF) of the bubble events to a reference CDF in each of the phase space dimensions. The reference CDF is the CDF of the time-series itself. As an indicator of the expected variation in CDFs, the standard deviation of 10,000 CDFs, each constructed from 141 points randomly sampled from the time-series, was computed. A significant variation of the bubble event CDF from that of the reference in any of the dimensions, would indicate some correlation to the

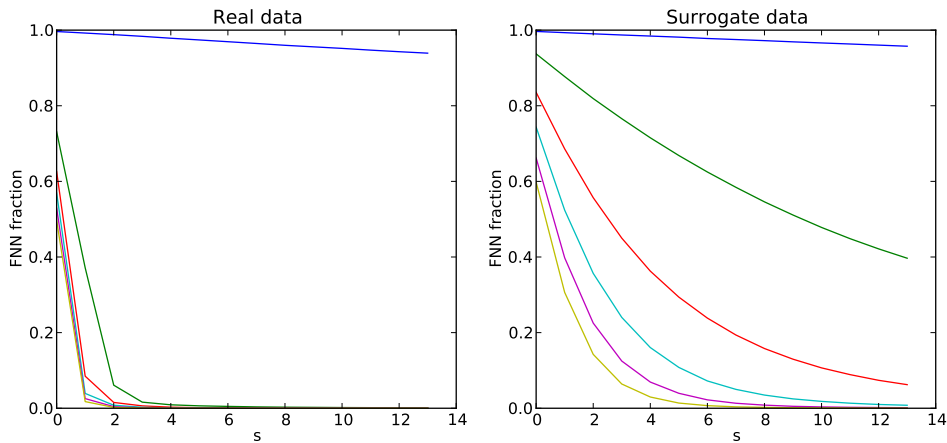


Figure 4.6: The fraction of false nearest neighbours (FNN) against the threshold value for embedding dimensions from 1 to 6 (top to bottom) and a lag of 150s, for both the real data (left hand plot) and a surrogate data series (right hand plot). The difference between the real and surrogate data shows that the reduction in FNN as we increase the embedding dimension is not simply due to linear correlations in the data. For an embedding dimension of 4, the FNN fraction reduces very quickly for small threshold values and there is little difference in behaviour compared to larger embedding dimensions. We therefore chose 4 as a suitable embedding dimension for our analysis.

phase of the cycle. Differences between CDFs were quantified using the two-sample Kolmogorov-Smirnov test (K-S test). The computed critical value for the K-S test at 90% confidence (based on a reference sample size of 90901, and a bubble event sample size of 141) is 0.102.

To verify the technique, we created a set of 95 fake bubble events located at the peaks of the mean speed cycles (Fig. 4.7). These events were then subjected to the same analysis as the real bubble events. The critical value for the K-S test at 90% confidence is 0.125 for the fake bubble sample size of 95. As shown in Fig. 4.8, the CDFs for the fake bubble events show a strong deviation from that of the random samples in each of the phase space dimensions, with K-S test results of 0.50, 0.15, 0.16 and 0.13 respectively (i.e. all above the critical K-S value, suggesting the two samples came from different distributions). Hence, the technique correctly identified the correlation between the fake bubble events and the phase of the speed cycles.

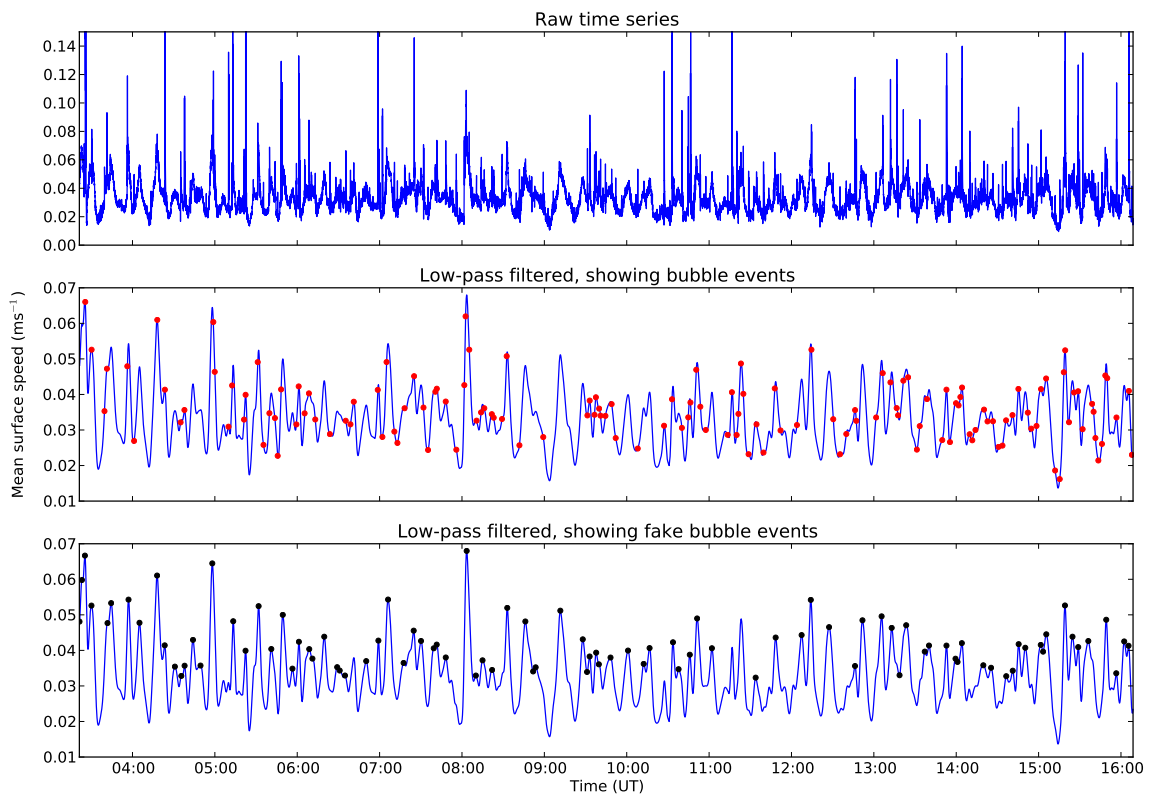


Figure 4.7: Top panel: time-series of mean lake surface speeds from 24 December 2010. Middle panel: the same data, low-pass filtered to remove noise and spikes due to bubbles and with bubble events marked. Bottom panel: low-pass filtered data with the fake bubble events used for testing marked.

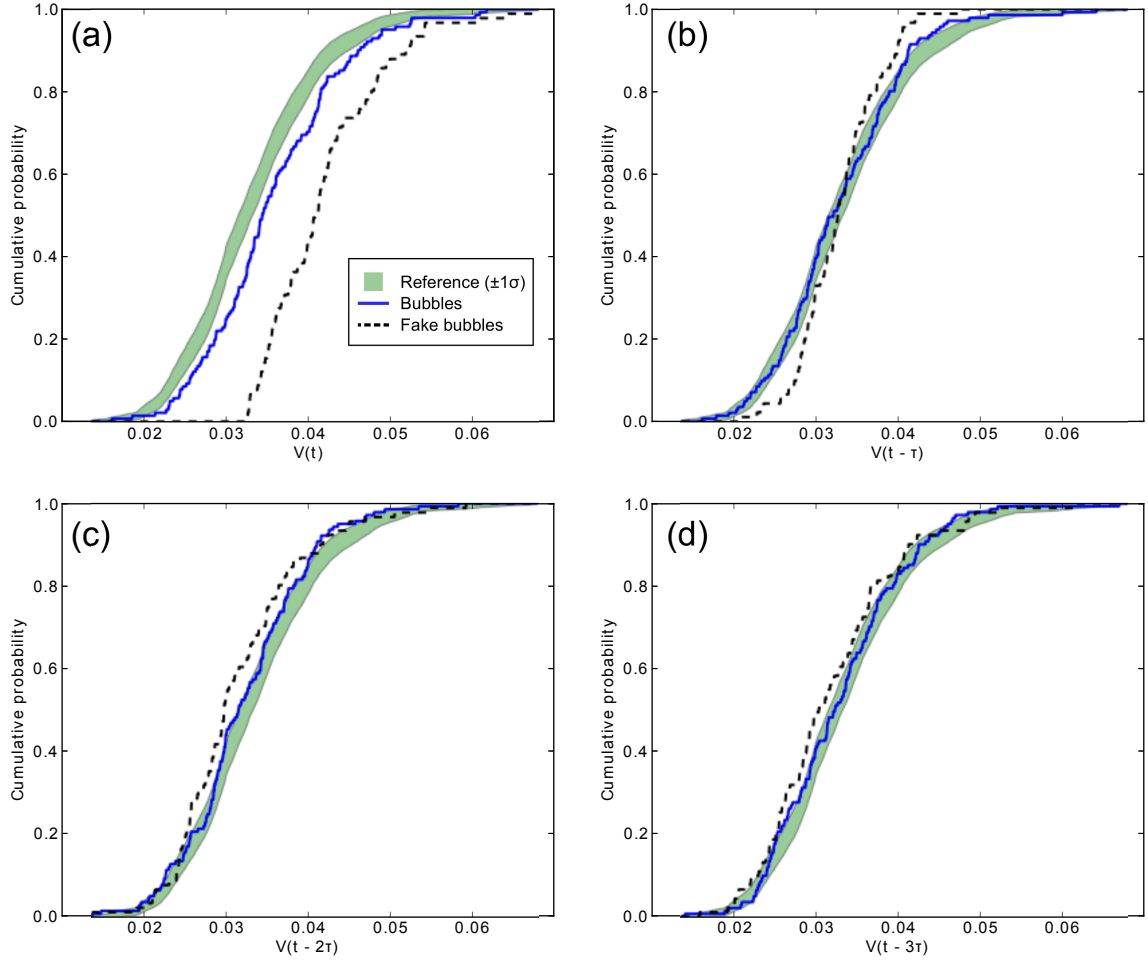


Figure 4.8: The cumulative distribution functions (CDFs) in each of the four phase space dimensions for the bubble events (solid line) and fake bubble events (dashed line). The x-axes represent the coordinates of the events in the corresponding phase space dimension, from the zero-lags dimension, $V(t)$, up to the three-lags dimension, $V(t - 3\tau)$, where $\tau=150$ s). The shaded region represents one standard deviation on either side of the reference CDF (i.e. the CDF of the mean speed data). Large deviations from the reference CDF are indicative of a correlation with the phase of the speed cycles, as can be seen in the fake bubble data. The deviation from the reference in the first dimension (a) of the bubbles CDF is attributed to imperfect filtering of the signal rather than a phase dependence.

4.3 Results

The 2010 field season was characterised by exceptional visibility of the lava lake. In addition to the IR images captured, several short time-series of visible images were captured using a digital SLR camera equipped with a telephoto lens. Figure 4.9 shows a short time-series of mean surface speed and mean surface temperature data calculated from IR images, with visible images corresponding to peaks and troughs in the speed also shown. There are no consistent differences observed between the appearance of the lake surface during periods of high speeds and periods of low speeds.

Oppenheimer et al. [2009] found a strong correlation between the phase of cycles in mean surface speed and radiative heat loss in their data set. This correlation is further demonstrated by the time-series shown in Fig. 4.9 and Fig. 4.10. Note however, that since we have not attempted an accurate temperature calibration of the IR images, we present mean surface temperatures normalised to their maximum value. What is not clear from these data alone, is whether the temperature variations observed are due to an increase in the surface temperature of the lava in the lake, or an increase in the area of cracks in the surface crust of the lake caused by the increased motion [Oppenheimer et al., 2009]. Additional cracks will expose more of the underlying lava to the surface and will therefore cause an increase in the mean temperature recorded by the IR camera. Increased cracking during periods of higher surface speed is not obvious in the images shown in Fig. 4.9, suggesting that the changes in recorded temperature are indeed due to variations in the mean temperature of the lake surface. However, we feel that a qualitative argument such as this is insufficient to rule out increased cracking as a cause.

In an attempt to identify more rigorously the reason for the temperature cycles, we compared the histograms of the thermal images at the minima and maxima of the cycles. If the cycles are caused by an increase in surface temperature, then we would expect the histograms at the cycle maxima to be shifted relative to those at the minima. If increased cracking is the cause, we would expect more high temperature pixels, resulting in a skewing of the histograms at the maxima compared to those at the minima. Unfortunately, the results obtained were ambiguous, with greater differences between histograms from the same point in the cycles than found by comparing those at maxima to those at minima. The cause of the measured temperature fluctuations remains elusive, however, it seems likely that they are caused by a combination of both increased surface cracking and increased surface temperature.

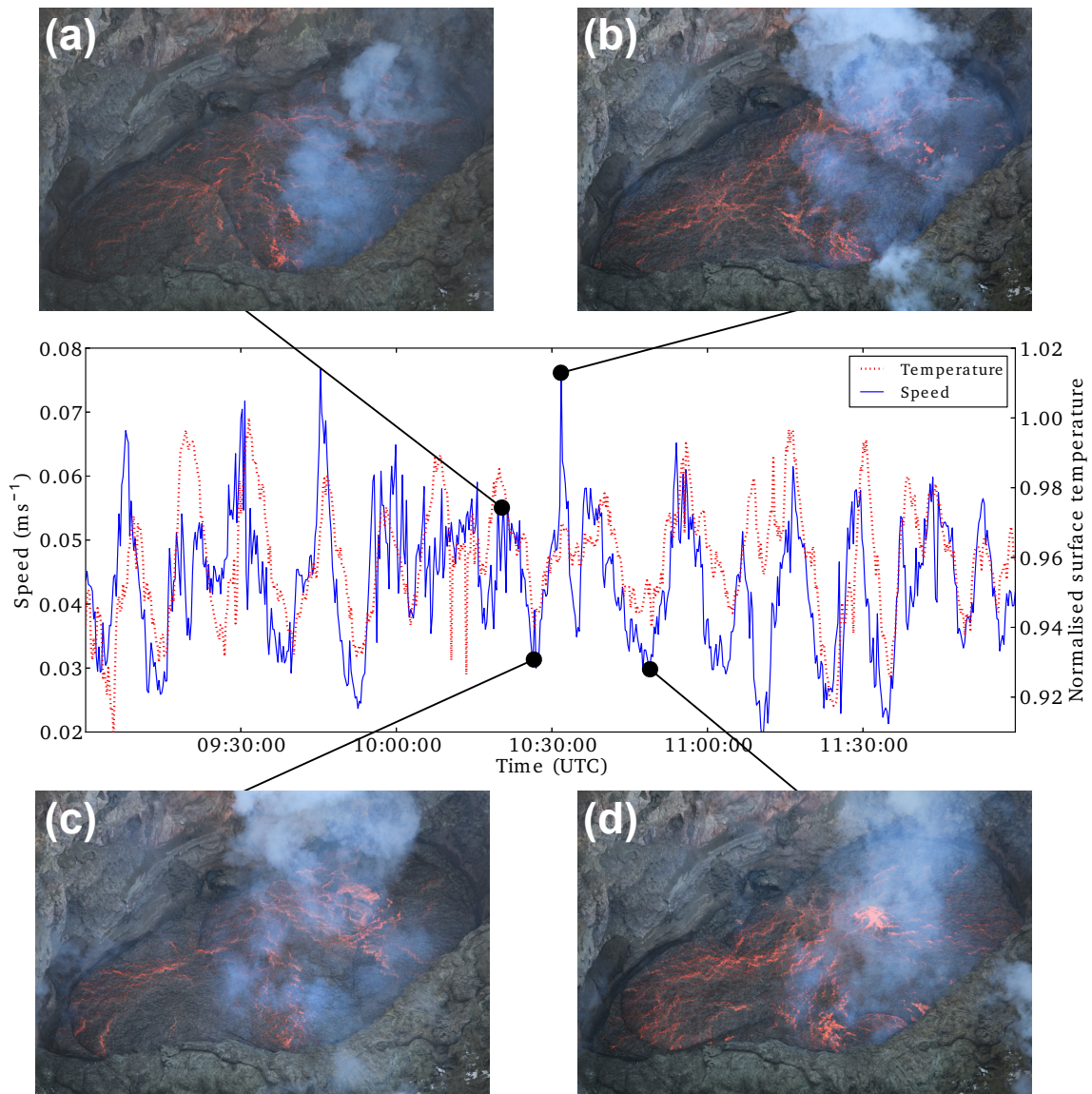


Figure 4.9: Time series of mean lake surface speed and mean surface temperature (arbitrary units) from 17 December 2010 calculated from images captured with the P25 IR camera, with photographs showing the appearance of the lake surface at periods of high surface speed (a,b) and low surface speed (c,d). There is no distinct difference between the appearance of the lake surface during periods of high or low surface motion. Note that in (d), a small gas bubble can be seen just reaching the surface. Note that the bubble does not appear as “shot noise” in the speed data because of the poor time resolution of the P25 camera. The lake is approximately 40 m across its long axis.

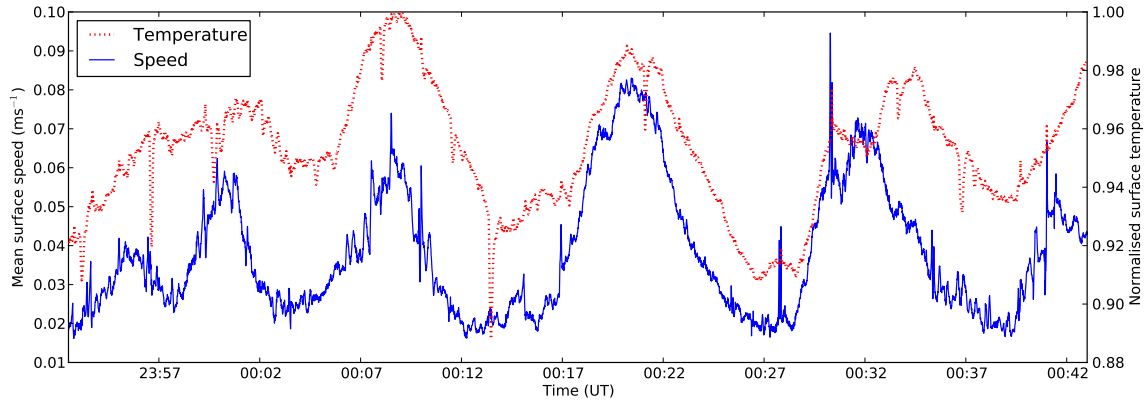


Figure 4.10: Short time-series of mean surface velocity and mean surface temperature data from 21–22 December 2010 calculated from images acquired with the SC645 camera. We have not attempted to retrieve accurate temperatures from the images, and instead report unitless temperature values normalised by the maximum value in the time-series. The pulsatory behaviour is particularly clear during this period, and the symmetry of the peaks in time (i.e. about their horizontal centre) is evident.

It is important to realise that even if increased surface cracking is insignificant, cycles in the surface temperature do not necessarily reflect periodic variations in the internal temperature of the lake itself. It is possible for example, that during periods of increased surface motion the mean surface age of the lake is lower. Younger crust is likely to be thinner, and hence the conductive heat flow through it will be larger, resulting in higher measured surface temperatures despite the bulk temperature of the lake remaining static.

Figure 4.10 shows a short time-series of mean surface speed and mean surface temperature calculated from IR images captured in 2010. The pulsatory behaviour was particularly pronounced during the period shown, and the waveform of the cycles is clear. The peaks in speed and temperature are approximately Gaussian in shape, with rising and falling edges that are symmetric about the centre of the peak. The peaks tend to be shorter lived than the troughs, suggesting a system with a stable baseline state that is being perturbed, rather than a system that is oscillating about a mid-point. There also appears to be a correlation between the magnitude of the cycles and their period, with longer period cycles having a greater amplitude. However, such a relationship is not always observed, and there are many instances where the opposite is true.

Morlet spectrograms of the mean speed data from the 2007–2011 field seasons are

provided in Section 4.3.1. What is clear from the data is that the cycles in speed are not strictly periodic. Instead, there tends to be a broad range of periodic components present, centred at around 900 s. However, these components appear to be fairly consistent across the dataset and have not changed appreciably during the period of study. Figure 4.11 further illustrates this point, showing the time average (normalised to have a mean of zero and standard deviation of one) of the modulus of all the Morlet spectrograms from each field season. The general trend towards higher modulus at longer periods is due to the fact that long period variations in mean speed tend to be of greater amplitude than short period variations (as is typical for most time-series data from natural systems). Despite this, the broad peak around 900 s is evident in the data from the 2007–2011 field seasons. The time-series from the 2004 and 2006 field seasons were of insufficient duration to allow analysis for long period behaviour, and as a result do not show the same behaviour as the other years.

It is unfortunate that during the 2005 and 2006 field seasons, which covered the period of increased explosive activity, IR data were either not collected at all, or are of insufficient length to compare to other years. However, as shown in Fig. 4.12, the pulsatory behaviour of the lake appears to be unperturbed by large bubble bursts. The figure shows a short time-series of mean surface velocity data from 29–30 December 2010, during which a large (~ 30 m) bubble arrived at the surface of the lake. Despite a significant ejection of material from the lake, the mean speed data show that the pulsatory behaviour appears to be uninterrupted on timescales greater than that of lake refill (several minutes). It is interesting to note that at the time of the explosion, the Morlet spectrogram shows a particularly strong periodic component at ~ 1000 s. We believe that this may be caused by increased surface speeds in the build-up to the explosion and also during the recovery phase as the lake refills. The IR images show that the lake level rises rapidly immediately prior to a large bubble reaching the surface, likely causing an increase in the recorded surface speed. Rapid flow of lava into the lake during the refill phase of an explosive event is also likely to cause elevated surface speeds.

In addition to the apparent stability of cycles in surface speed, the magnitude of the surface speed has also remained approximately unchanged since 2004. Although the mean surface speed can exhibit considerable variability (~ 3 – 20 cm s^{-1}) on a timescale of days, no systematic change was observed over the period of study.

Whilst the behaviour of the mean surface speed has remained remarkably stable,

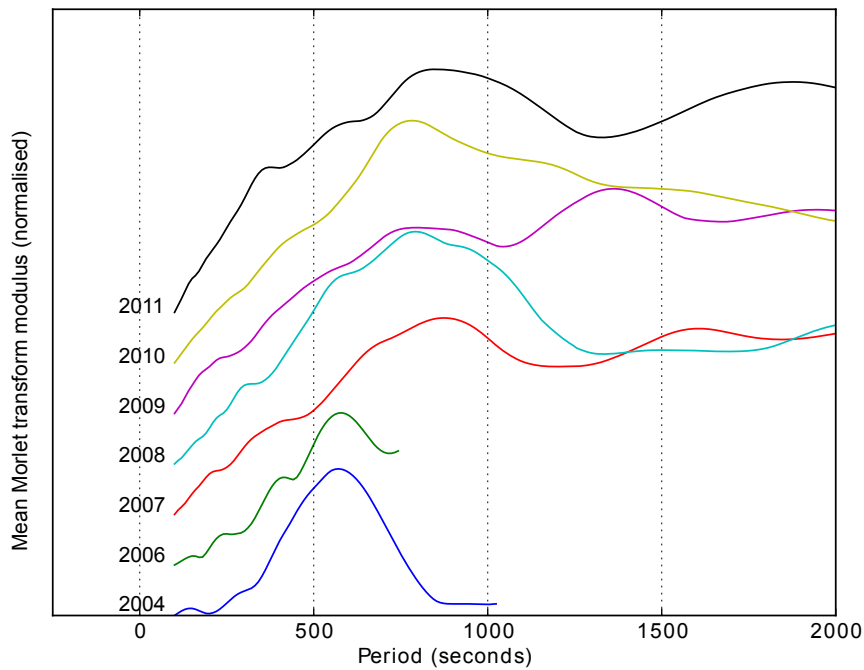


Figure 4.11: Normalised time averages of the Morlet transform modulus of all available data from each field season. The data from each year have been vertically offset from each other for clarity. A broad peak corresponding to the period of the lake cycles (~ 900 s) is evident in the 2007–2011 data confirming that the cyclic behaviour is a persistent and largely unchanging feature of the lake. The time-series from the 2004 and 2006 field seasons were of insufficient length to be able to resolve long period fluctuations.

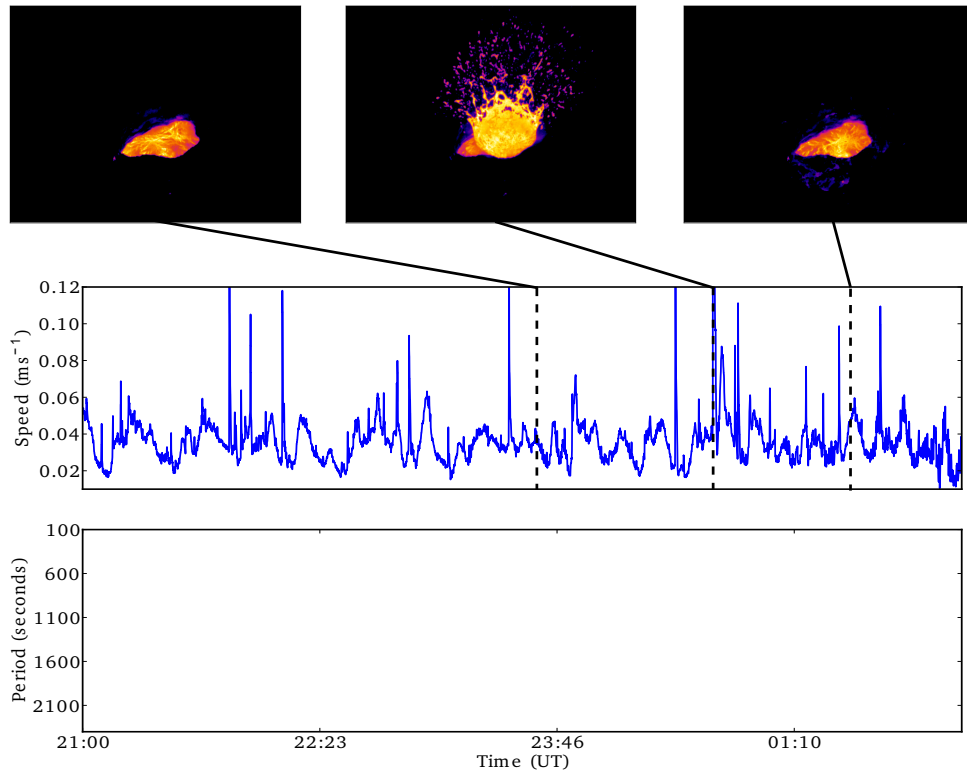


Figure 4.12: A 5 h time-series of mean surface speed data from the 29–30 December 2010 calculated from images acquired with the SC645 camera and the corresponding Morlet spectrogram. The IR images above show the state of the lake before, during and after a large (~ 30 m) bubble burst. Cycles of between ~ 600 – 1100 s are visible across the time-series both in the Morlet spectrogram and in the mean speed data. The strong ~ 1000 s signal in the spectrogram corresponding to the explosion itself may be caused by elevated speeds due to the rising of the lake level prior to the explosion and the subsequent refilling of the lake afterwards.

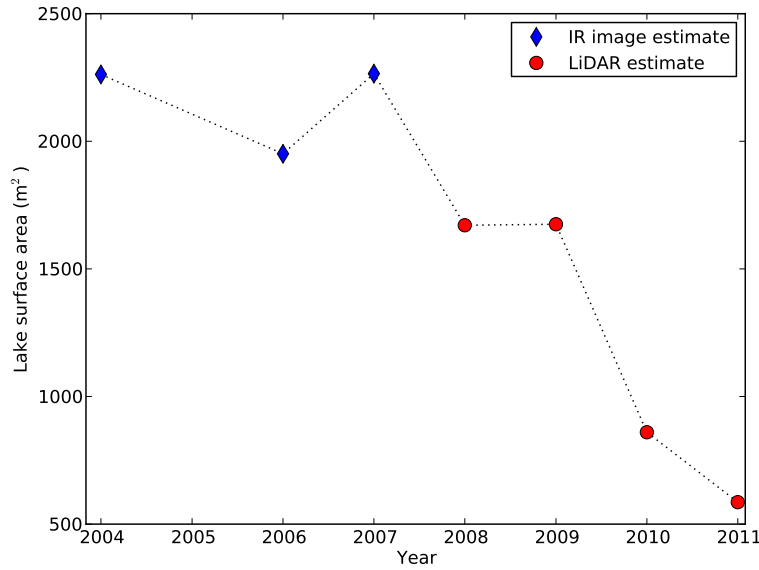


Figure 4.13: Surface area of the Erebus lava lake by field season (i.e. December of the year shown). The areas have been estimated from a combination of terrestrial laser scan data (Jones [2013], Frechette and Killingsworth pers. comm.) and rectified IR images.

the visual appearance of the lava lake has changed significantly. Figure 4.13 shows how the surface area of the lake (calculated from IR images and terrestrial laser scan data) has decreased since the first measurements in 2004. Overall the surface area has reduced by a factor of approximately four. The terrestrial laser scan data also show that since at least 2008 (when the first such data were recorded), the decrease in area has been accompanied by a 3–4 m per year drop in the lake’s mean surface elevation (Jones [2013], Frechette and Killingsworth pers. comm.). The dramatic reduction in surface area cannot be accounted for by the drop in surface elevation (i.e. due to the lake receding into a conical basin) since the lake walls are observed (from terrestrial laser scan data and visual observations) to have a near-vertical profile. It seems likely therefore, that the observed decrease in surface area is due to a change in the geometry of the lake basin, either due to accretion of lava onto its sides, or deformation of the surrounding rock. The apparent lack of influence of lake geometry on the cyclic behaviour would tend to suggest that the cycles are driven by processes occurring in the magma conduit or a connected reservoir rather than in the lake itself.

Figure 4.8 shows the cumulative distribution functions (CDFs) of the bubble events, and fake bubble events, in each of the four phase space dimensions. The shaded areas

delimit one standard deviation on either side of the reference CDFs. As discussed in Section 4.2.5, the CDFs for the fake bubbles show a strong deviation from the reference, correctly identifying the correlation between the phase of the speed data and the fake bubble events. In contrast, the CDFs for the real bubble events are very similar to the reference in all but the first dimension. The K-S test gives values of 0.15, 0.05, 0.07 and 0.06 for the four dimensions, respectively. Apart from the first dimension, these are all below the critical K-S value at 90% confidence (0.102), indicating that the bubble events are from the same distribution as the speed data itself and that there is, therefore, no correlation between the phase of the speed cycles and the bubbles.

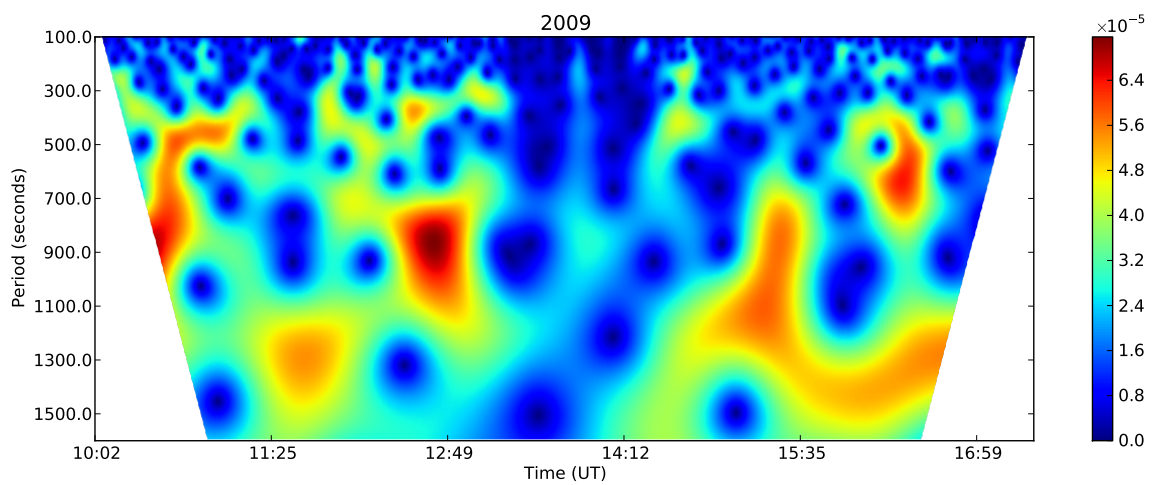
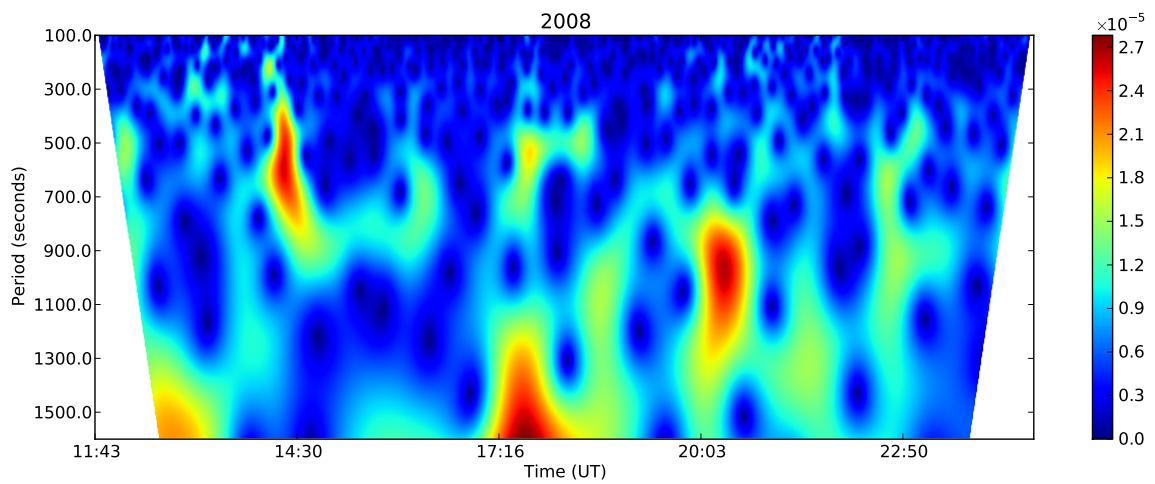
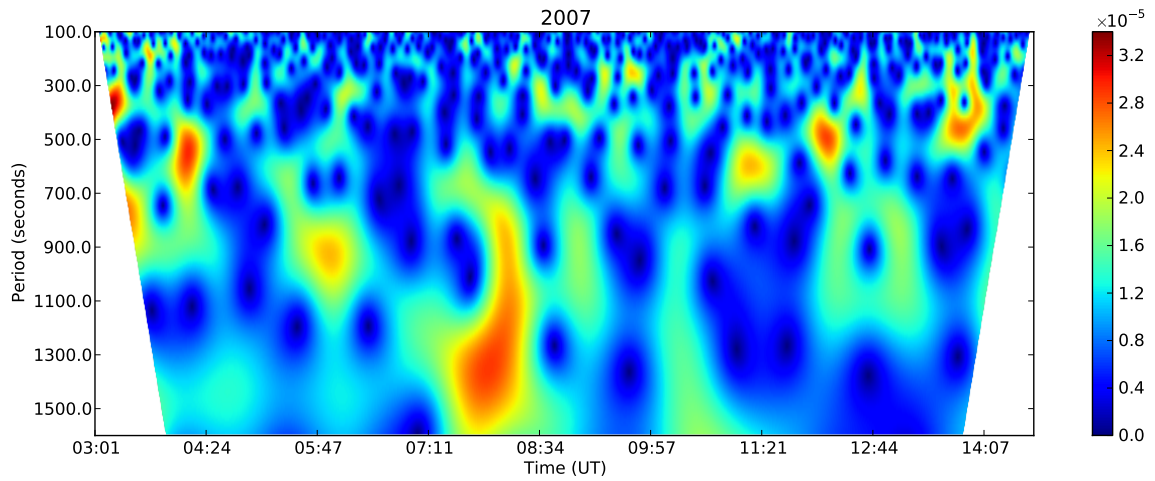
In the first dimension, the CDF of the bubble events appears to be the same shape as that of the mean speed data, but shifted slightly to the right (higher mean speed). We believe that this is caused by the failure of our low-pass filtering to remove fully the spikes caused by bubble events in the mean speed data, rather than any correlation with the phase of the cycles. As a result, bubble events appear to occur at slightly higher speeds than they actually do, shifting the CDF to the right. We tested this hypothesis by plotting the CDF of 141 randomly selected points from the speed data with a linear offset of 0.002 ms^{-1} added. The results showed a CDF that matched that of the mean speed data in all dimensions except the first, which showed a linear offset to the right as expected. We therefore conclude that the bubble events are not correlated to the phase of the velocity cycles and that the deviation we observe in the first dimension is due to the low-pass filter's inability to remove completely the effects of bubble events from the underlying mean speed signal.

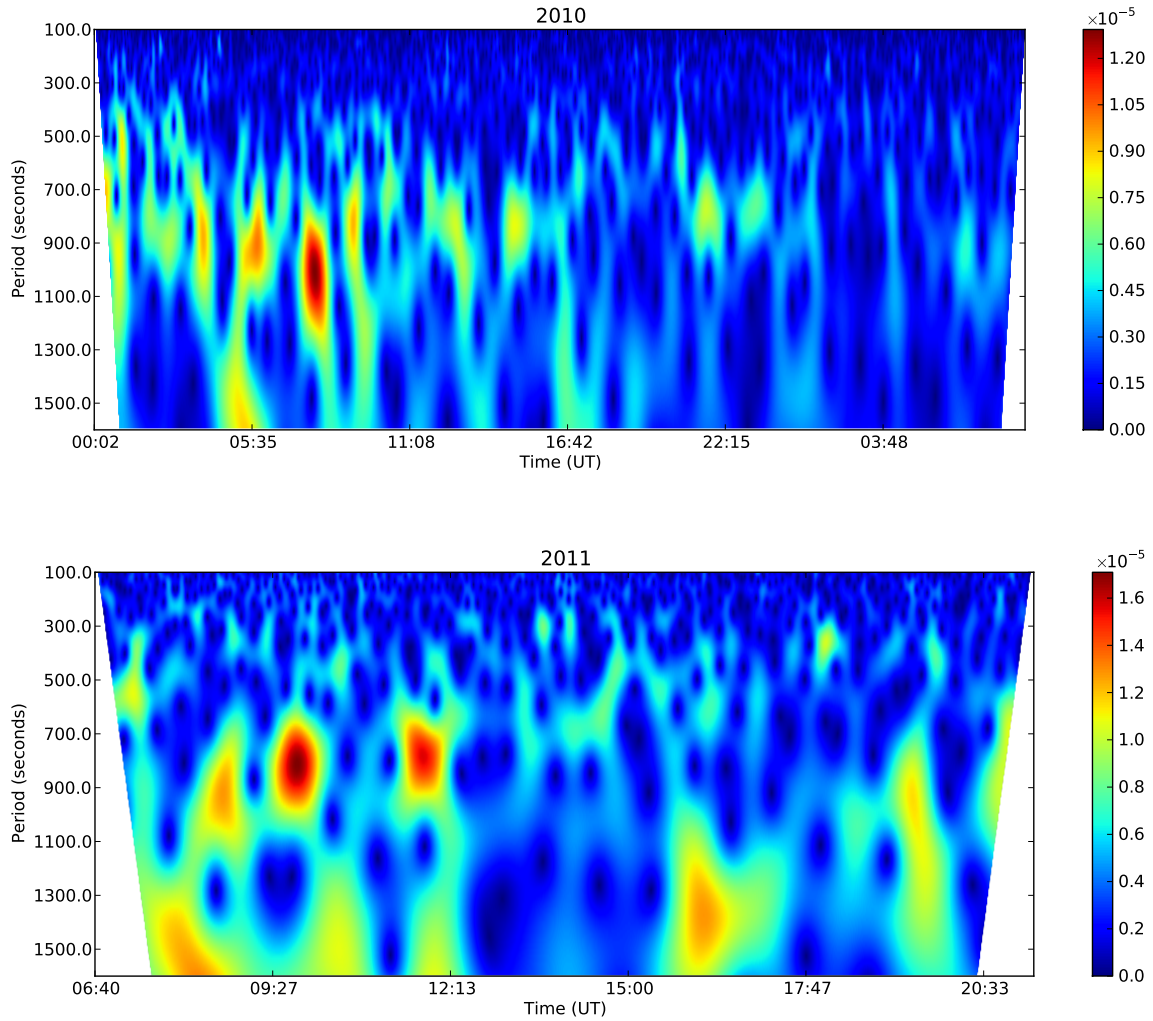
4.3.1 Spectrograms

Shown below are representative Morlet spectrograms of the mean surface speed of the lava lake from 2007-2011. The spectrograms shown here are from the longest continuous time series of IR images from the P25 camera from each year. Data from 2004 and 2006 have not been included, since the time series are too short to evaluate periods of above ~ 600 s.

The spectrograms demonstrate that the cycles are not perfectly periodic, nor is there any discernible pattern to the variation in their period. Instead, strong wavelet responses are apparent, ranging in period between ~ 500 – 1100 s, and often with sharp

transitions between them. The complexity of the spectrograms (in addition to the issues discussed in Fig. 4.4) demonstrates the difficulty of interpreting extended time series of speed data due to the high degree of non-stationarity.





4.4 Discussion

A common conclusion of multi-year studies conducted at Erebus volcano is that its behaviour is remarkably stable. Observations of radiant heat output [Wright and Pilger, 2008], SO_2 flux [Sweeney et al., 2008] and seismicity [Aster et al., 2003] have all found very little variation during the past decade. Our findings that the pulsatory behaviour of the lava lake has been a persistent and unchanging feature (both on a daily and a yearly time-scale) since at least 2004 fit well with these previous findings and further emphasise the remarkable stability of Erebus's magmatic system. The preservation of cycles in surface speed despite large perturbations to the system (decametric bubble bursts) is indicative not only of the stability of the responsible mechanism, but also that it is likely sourced at a deeper level than the lake itself. This argument is further supported by the consistency of the motion cycles despite a reduction in the area of the lava lake, exposed at the surface, over

the period of observation.

The broad width of the peak in the spectrograms that we observe is consistent with the findings of Oppenheimer et al. [2009] who found the period of the fluctuations in mean lake speed to vary between ~ 5 –18 min for the 2004 dataset. Although short sections of our data appear to contain several discrete frequency bands within this range, such fine scale structure is never observed consistently over time periods of more than a few hours. No clear pattern to the variation of the period of fluctuations measured is evident from the spectrograms. However, it is important to consider how well the mean speed of the lake surface represents the underlying process responsible for the pulsatory behaviour. Even if this process contains well defined, discrete periods, complex flow dynamics and other forcing mechanisms (such as thermal convection within the lake) may result in a highly non-linear response in the surface speed. It is possible that the broad distribution in period of the cycles in speed observed is due to the complex coupling between a periodic driving mechanism and the dynamics of the bubbly flow within the lake. Given the correlation between surface motion and gas composition ratios (which must have different couplings to the driving mechanism) reported by Oppenheimer et al. [2009], we believe that the variability in period stems primarily from the variability in the underlying driving mechanism.

Current theories on driving mechanisms for lava lake fluctuations can be grouped into three main categories; (i) instability in density driven, bi-directional flow of magma in the conduit feeding the lake [Oppenheimer et al., 2009], (ii) “gas piston-ing” caused by gas accumulation either beneath a solidified crust on the surface of the lake [Patrick et al., 2011] or as a foam layer at the top of the lava column [Orr and Rea, 2012], and (iii) gas bubble-driven pressurisation changes [Witham et al., 2006]. In the latter mechanism, the (uni-directional) upflow of bubbly magma in the conduit is interrupted by excess hydrostatic pressure in the lake. Stagnation of the flow allows bubbles in the conduit to coalesce into large gas slugs that rise to the surface independently of the melt. The loss of large gas slugs at the surface of the lake causes an increase in pressure at the base of the conduit. If this exceeds the pressure in the magma chamber then downflow occurs, suppressing the ascent of bubbles in the conduit. As the lake drains, the downflow reduces until it can no longer suppress the ascent of bubbles, and the cycle repeats. Witham et al. [2006] were able to demonstrate this mechanism by bubbling air through a water column with a basin attached to the top to represent the lake. They observed cyclic varia-

tions in the depth of water in the basin, consisting of a logarithmic increase in depth followed by a rapid, linear decrease.

As shown by Orr and Rea [2012], gas pistoning, as observed at Kīlauea, is also an asymmetric process, consisting of a relatively slow, cumulative deviation from the baseline state of the system as bubbles are trapped in the foam layer or beneath the solidified crust, followed by a sudden release of the accumulated gas and rapid return to the baseline state. The temporal symmetry of the perturbations in the Erebus lava lake is not consistent with either of these mechanism. It may be argued that the complex geometry of the upper magmatic system of Erebus could lead to a more symmetric variation than observed by Witham et al. [2006] and Orr and Rea [2012]. However, our finding that the arrival of small (metre-scale) bubbles at the surface of the lake is uncorrelated with the phase of the speed cycles is only consistent with the bi-directional flow mechanism. Both bubble-driven mechanisms require a periodic release of bubbles prior to lake draining and, in the case of the Witham et al. [2006] mechanism, a significant decrease in the number of bubbles during lake draining. Large (decametric) bubbles, typically occur at Erebus only a few times per week, and cannot therefore be responsible for the ~ 5 –18 min cycles. Since no periodic release of small bubbles is observed either (visually e.g. Fig. 4.9, or statistically Fig. 4.8), we argue that the pulsatory behaviour of the lava lake at Erebus volcano is driven by magma exchange between a shallow magma chamber [Zandomenighi et al., 2013] and the lake via bi-directional flow in the connecting conduit.

It is interesting to note that, on average, bubble events in the data presented in Fig. 4.7 occur every 5.5 min. This is comparable to the cycles in surface speed, which range from ~ 5 –18 min in period. However, given that some cycles occur without any bubbles surfacing (e.g. 09:00–09:15 in Fig. 4.7) and given the random distribution of bubbles with respect to the phase of the cycles (Fig. 4.8), we believe the similarity in timescales to be coincidental.

Pulsatory behaviour deriving from bi-directional flow in a conduit has been demonstrated for single-phase systems using two fluids of different densities [Huppert and Hallworth, 2007]. However, any exchange of magma occurring at the Erebus lava lake will clearly be multi-phase, and its dynamics will be influenced not only by the presence of gas bubbles but also by the large anorthoclase crystals which constitute 30–40% of the melt volume [Kelly et al., 2008]. Indeed, numerical simulations of

the Erebus magmatic system indicate that the inclusion of crystals has a very significant effect on the flow dynamics [Molina et al., 2012]. While it is likely that gas bubbles play an even more significant role than the crystals, a complete multi-phase flow model of the Erebus system is not yet available. Whilst it is possible that the dynamics observed by Huppert and Hallworth [2007] may not be applicable to a complex multi-phase system such as that at Erebus, the lack of compelling evidence for an alternative mechanism leads us to conclude that instability associated with density-driven bi-directional flow is the most likely explanation for the observed cyclic behaviour. As noted by Oppenheimer et al. [2009], the density contrast driving the flow is likely to result primarily from magma degassing.

Bouche et al. [2010] observed that bubbles in the lava lake at Erta ‘Ale volcano may be trapped beneath the cooled crust at the surface of the lake and forced to travel laterally until they encounter a crack in the crust before they can surface. If such a process were also occurring in the Erebus lake, then it would invalidate our comparison of the bubble events to the cycles in surface speed. The variable duration of lateral migration of bubbles would prevent any direct comparison of the timings of the bubble events and the phase of the cycles, since it would tend to randomise their arrival at the surface. However, it can be observed in the IR images that even small bubbles ($\ll 1$ m in diameter) break the surface of the Erebus lake in areas with no visible cracks. We do not therefore believe that the crust on the Erebus lake inhibits bubble ascent, nor that it causes significant lateral displacement of bubbles. These differences likely reflect the contrasting rheologies of the magmas involved, which in turn reflect the differences in composition, temperature, viscosity and crystal content.

In our analysis of the correlation of bubble events to lake cycles (Section 4.2.5), we have only looked at small bubbles in detail, since the dataset did not contain any large events. Small bubbles may be sourced within the lake itself, whereas large (decametric, causing ejection of material out of the lake) bubbles are thought to have originated at greater depths [Oppenheimer et al., 2011, Burgisser et al., 2012]. It is possible that the passage of large bubbles through the conduit may perturb the bi-directional flow of magma, causing variations in the period of lake surface speed fluctuations. Although no such variation was observed in Fig. 4.12, we do not believe this to be sufficient evidence to discount such a possibility. Since the arrival of large bubbles is relatively infrequent, a time-series spanning several months would need to be analysed to achieve a statistically significant sample size with which to

investigate possible effects of large bubbles on the lake’s motion.

4.5 Conclusions

In this chapter, we have reported an analysis of thermal infrared image data of the active lava lake at Erebus volcano that spans seven field campaigns from 2004–2011. In total 370,000 useful images were acquired representing 42 “field days” of observations and spanning contiguous observations of up to 44 h duration. The images were analysed using a feature-tracking algorithm to determine surface motion vectors from which the mean speed of the surface of the lake was derived, and this parameter used to monitor the lake’s pulsatory behaviour. Shot noise in the mean-speed data was found to indicate bubbles arriving at the surface of the lake, allowing an analysis of the timings of bubble events with respect to the phase of the surface speed cycles.

Since 2004, the apparent size (surface area) of the Erebus lava lake has decreased by a factor of four. Despite these changes in the lake’s appearance, its pulsatory behaviour has remained constant over the period of study, exhibiting cycles in mean surface speed with periods in the range ~ 5 –18 min. Mean surface speeds are typically between 3 and 20 cm s^{-1} . No obvious long-term progression of the cycles was observed. Surface speed time-series are not symmetrical about their mean (the troughs in speed are broader than the peaks), suggesting that the pulsatory behaviour is due to intermittent perturbations of the system, rather than an oscillatory mechanism.

Bubbles arriving at the surface of the lake show no correlation to the phase of the surface speed cycles. We therefore conclude that the pulsatory behaviour of the lake is associated primarily with the flow dynamics of magma exchange within the shallow plumbing system rather than by a flux of bubbles.

While we have analysed a substantially larger dataset than Oppenheimer et al. [2009], we have still been limited by the intermittent coverage. We hope that our recently-installed autonomous thermal camera system will yield much more extended time-series, facilitating investigations into the effect of large (decametric) bubbles on the pulsatory behaviour of the lake.

Chapter 5

Multi-parameter Observations of Cyclic Lava Lake Behaviour

The work presented in this chapter was undertaken in order to meet the “Multi-parameter Observations of Cyclic Behaviour” research objective (Section 1.7.3). As discussed in chapters 1 and 4, numerous studies at Erebus volcano have recorded pulsatory behaviour in many of the observable properties of its active lava lake. However, although the periods of the cycles in the different properties recorded are similar, suggesting they are linked, a lack of overlap between the different measurements has prevented direct comparisons from being made. Using high time-resolution measurements of surface elevation, surface speed, gas composition and SO₂ flux we demonstrate for the first time a definitive link between the cyclic behaviour in each of these properties. The cycles are found to be in-phase with each other, with a small but consistent lag of 1–3 min between the peaks in surface elevation and surface speed. Explosive events are found to have no observable effect on the pulsatory behaviour beyond the ~5 min period required for lake refill.

The majority of content from this chapter has been published as: Peters, N., C. Oppenheimer, D. R. Killingsworth, J. Frechette, and P. Kyle, “Correlation of cycles in Lava Lake motion and degassing at Erebus Volcano, Antarctica”, *Geochemistry, Geophysics, Geosystems*, 2014

The collection and processing of the FTIR data presented in this chapter was performed by Clive Oppenheimer. Collection and analysis of the TLS data was undertaken by Drea Rae Killingsworth and Jed Frechette. The section describing the FTIR methodology (Section 5.2.3) was written by Clive Oppenheimer, and is reproduced here with his consent.

5.1 Introduction

As discussed in Section 1.3, the pulsatory behaviour of the Erebus lava lake manifests itself in many of its observable properties. In Chapter 4, we used the surface motion of the lake as a metric to assess the inter-annual variability of the cyclic behaviour. However, the choice of surface speed as a parameter was made purely on the basis of an extended set of IR images being available. Observing how the cycles in different parameters relate to each other is key in understanding the underlying mechanism responsible for them. Since the cycles are believed to derive from processes occurring at depth, a detailed knowledge of their behaviour will undoubtedly lead to an improved understanding of how Erebus's magmatic system as a whole functions. Unfortunately, coordinating multi-instrument studies of volcanoes, such that the time series of different data overlap, is a non-trivial exercise. As a result, previous field campaigns at Erebus volcano have largely failed to concurrently record fluctuations in more than one parameter. Similarities between surface motion and gas composition were observed by Oppenheimer et al. [2009] in a short time series from 2004. However, due to the limited available data and a lack of high precision time-stamping, a detailed analysis of the correlation was not possible. Thus, although it has been widely assumed that the cyclic behaviour of the different parameters must be linked, to date there has been no significant body of data to confirm this.

As the infrastructure installed by the Mount Erebus Volcano Observatory (MEVO), such as power and data telemetry, continues to be improved, longer continuous time series are becoming possible [Chapter 2, Peters et al., 2014c] and with them, a greater degree of overlap between different observations. Here we present data from December 2012 and December 2013 which show for the first time a definitive link between the pseudo-periodic behaviour of the lava lake's surface speed, surface elevation, SO₂ flux and plume composition.

In December 2013, the lake was approximately 30 m across (Fig. 5.1), with a surface area of $\sim 580 \text{ m}^2$ (measured using TLS). This is slightly larger than its surface area in 2012 ($\sim 400 \text{ m}^2$), but is just a quarter of its 2004 size (Fig. 4.13). As discussed in Section 1.6, in 2013, Erebus was in a particularly active phase, with several large explosive events occurring per day. Despite the increased activity, the lake's behaviour in periods of quiescence between explosions was indistinguishable from other years. We believe therefore that the data presented here are representative of Erebus's behaviour in general rather than only during its periods of elevated activity.

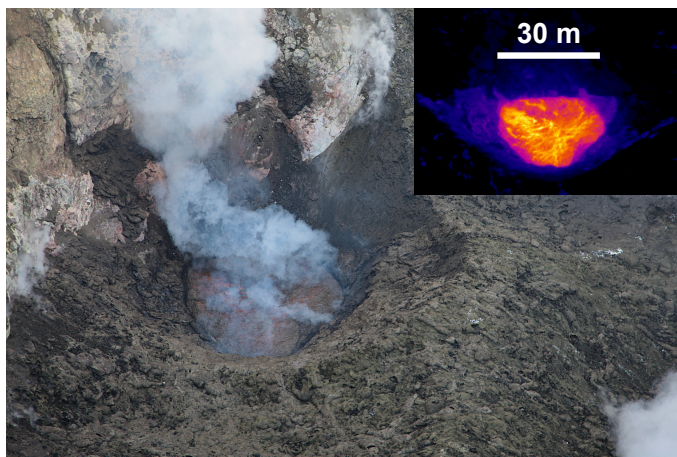


Figure 5.1: Visible and infrared images of the lava lake on 15 December 2013. Freshly ejected material surrounding the lake is visible in both images.

The findings of this chapter provide an important cornerstone for future studies, and will be of particular relevance to future efforts to model pulsatory behaviour either through experiments or computer simulations. They also provide a greater body of evidence in support of the conclusions reached in Chapter 4.

5.2 Methodology

5.2.1 Lava Lake Surface Velocity

Using a thermal infrared (IR) camera situated on the northern rim of Erebus’s main crater (~ 330 m from the lake), images of the lava lake were recorded at a rate of ~ 0.5 Hz. The thermal camera system used in this chapter is described in detail in Chapter 2. Despite the small visible surface of the lake compared to many previous years, estimates of the surface velocity using the same wavelet-transform feature tracking algorithm as used in Chapter 4 were still possible. TLS data collected during the 2013 field season were used to correct the IR images for perspective effects and the mean lake surface speed was then calculated using the same methodology as in Chapter 4.

Unlike the study presented in Chapter 4, there was no need to search the images for periods of data with little camera shake. The new tripod system installed in 2012 [Chapter 2, Peters et al., 2014c] has solved this issue. Instead, periods of data with good visibility of the lake (low humidity in the crater) which coincided with data from the FTIR and the DW-FOV DOAS were chosen. This selection process was

done by manually inspecting the images.

Subsequent processing of the mean speed time series presented has been avoided. The data shown have not been enhanced or filtered in any way. This is deliberate so as to make the signal to noise ratio clear to see. The correlations between data sets are still clearly visible “by eye” and we feel that this is sufficient to support our conclusions.

5.2.2 SO₂ Flux

Ultraviolet Differential Optical Absorption Spectroscopy (UV DOAS) is a powerful tool for monitoring volcanic sulphur dioxide emissions [Galle et al., 2003]. Typically, UV spectra are collected across a transect of the volcanic plume perpendicular to its transport direction, either through the use of a scanning unit or by carrying the spectrometer in a traverse [e.g. McGonigle, 2002, Salerno et al., 2009]. Sulphur dioxide flux is calculated by integrating across the transect and multiplying by rise speed (for a vertically rising plume) or by wind speed (for a horizontally drifting plume). Although this technique is well established and commonly used within the volcanological community, the necessity to record spectra at many positions across the plume greatly restricts the time resolution of the flux measurements made. It is therefore not possible to use the results in studies of dynamic phenomenon such as Erebus’s pulsatory gas flux. Furthermore, the inclusion of plume transport speed, which is often poorly constrained, in the calculation introduces large errors which are difficult to quantify.

Increasingly, ultraviolet cameras [Mori and Burton, 2006, Bluth et al., 2007] are being used to quantify SO₂ emissions associated with short lived events such as Strombolian eruptions [Tamburello et al., 2012, Dalton et al., 2009, Mori and Burton, 2009] and for comparison with other high time resolution monitoring data, such as observations of seismic tremor [Nadeau et al., 2011]. Plume transport speeds can be determined from the UV images either by a simple correlation of pixel values between successive frames, or by more advanced optical flow methods [Chapter 7, Kern et al., 2012, Peters et al., 2014a]. However, despite their promise as a tool for high time resolution SO₂ measurements, there remain many significant calibration issues which must be addressed before accurate fluxes can be obtained [Kern et al., 2010]. Although some of these issues have begun to be addressed by using a co-located UV spectrometer to calibrate the images [Lübcke et al., 2013], the technique

is still very much in its infancy. This, combined with the rather low SO₂ flux of the Erebus plume ($\sim 0.5 \text{ kg s}^{-1}$), makes measuring the periodic fluctuations using a UV camera problematic. Instead, we took a similar approach to that of Boichu et al. [2010], the so-called Dual Wide Field of View DOAS (DW-FOV DOAS) technique.

DW-FOV DOAS uses a pair of UV spectrometers connected by optical fibres to two telescopes. Each telescope houses cylindrical lenses to give its spectrometer a field of view that is very wide in one dimension (typically the horizontal) and very narrow in the other. The fields of view of the two spectrometers are aligned parallel along their long axes, with a small offset in the narrow field of view direction. The width of the fields of view is such that they encompass the entire plume (the width can be adjusted according to plume dimensions and viewing geometry) allowing the column amount of sulphur dioxide to be measured instantaneously at two different heights in the plume. Column amount measurements are made repeatedly with both spectrometers and by cross-correlation of the two time series the plume transport speed, and therefore flux, can be measured.

The spectrometers used in this study were OceanOptics USB2000+ instruments with a spectral range of 283–427 nm. Mercury lamp calibration spectra were collected at both the beginning and the end of the field campaign. We measured the instrument response function (assuming a Gaussian shape) from the calibration spectra using the AvoPlot software [Section 3.1, Peters, 2014] and found it to have a consistent full width at half maximum of 0.6 nm for both spectrometers across the wavelength range used for the SO₂ column amount retrievals ($\sim 310\text{--}324 \text{ nm}$).

SO₂ column amounts were estimated using the standard DOAS methodology [Platt and Stutz, 2008] whereby out-of-plume background spectra are averaged and used to calculate the Ring spectrum (this is used to correct for the distortion of the solar Fraunhofer lines due to rotational Raman scattering in the atmosphere). The averaged background is then fitted to both a solar spectrum [Chance and Kurucz, 2010] and the Ring spectrum calculated from the solar spectrum to estimate the wavelength calibration errors in the spectrometer, the so-called “shift and squeeze” correction. Each in-plume spectrum is then corrected for shift and fitted to the Ring spectrum calculated from the averaged background and scaled reference spectra for SO₂ [Vandaele et al., 1994] and O₃ [Burrows et al., 1999] (the dominant absorbers in the wavelength range of the fitting window). The optimum scaling factor for the SO₂ reference spectrum is directly proportional to

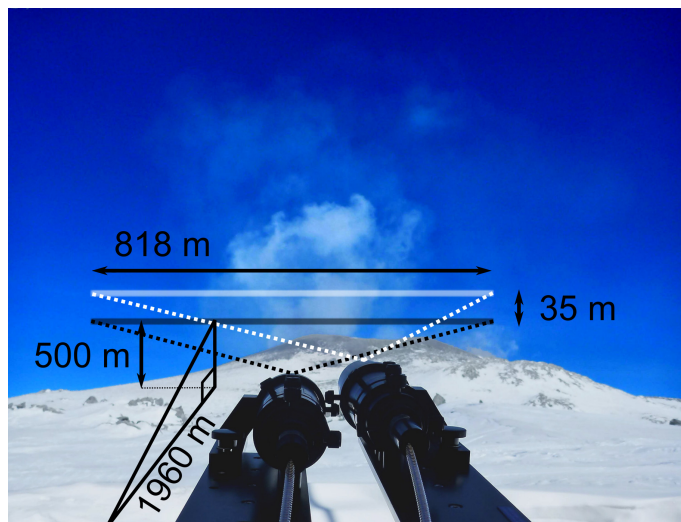


Figure 5.2: Photograph showing the plume conditions on 14 December 2013, with annotations describing the viewing geometry of the DW-FOV DOAS instrument. Although the plume is rising approximately vertically, there is a certain amount of grounded plume around the crater which will cause the instrument to overestimate the SO_2 flux.

the amount of SO_2 along the optical path of the spectrometer allowing column amounts to be extracted. All DOAS retrievals were implemented using a combination of the DOASIS software [Kraus, 2006] and scripts written by Tsanev (<http://www.geog.cam.ac.uk/research/projects/doasretrieval>).

Plume rise speeds were determined using the same windowed cross-correlation approach as Boichu et al. [2010], whereby a fixed length window of column amount data from the lower spectrometer is extracted at regular time intervals, normalised with respect to its mean and standard deviation, and cross-correlated with the normalised column amount data from the upper spectrometer (up to a certain maximum lag). In this study we used a window length of 600 s and a maximum lag of 120 s. The peak in the cross-correlation of the two signals is taken to represent the time taken for the plume to rise the separation distance between the two fields of view, in our case a distance of 36.5 m (Fig. 5.2). The rise speeds calculated were smoothed using a low-pass filter before being used in the flux calculation.

The column amounts recorded by each spectrometer in the DW-FOV DOAS system represent the mean column amount across its field of view at the distance of the

plume [Boichu et al., 2010]. The SO₂ flux, ϕ , can therefore be expressed as:

$$\phi = \frac{10^4 M}{N_{Av}} A_{\text{lower}} D v \theta_{\text{WFOV}} \quad (5.1)$$

where M is the molar mass of SO₂ in kg mol⁻¹, N_{Av} is Avogadro’s number, A_{lower} is the column amount recorded by the lower spectrometer in molec cm⁻², D is the horizontal distance to the plume in metres (see Fig. 5.2), v is the rise speed in m s⁻¹ and θ_{WFOV} is the field of view of the spectrometer in the horizontal (wide) direction in radians.

Note that our equation for flux differs slightly from that of Boichu et al. [2010], since we have accounted for the increased path length through the plume due to the inclined viewing angle. This results in an additional $\cos(\alpha)$ term, which cancels with that in the expression used by Boichu et al. [2010]. We use the column amounts recorded by the lower spectrometer in our flux calculation to minimise the distance above the lake that we are measuring.

The weather conditions at the summit of Erebus on 14 December 2013 were clear, with no clouds within the fields of view of the spectrometers and light winds of between 1–3 ms⁻¹. The plume was rising approximately vertically for a few hundred metres above the crater rim, before drifting sideways with the wind. However, as can be seen in Fig. 5.2, the plume was somewhat “messy” with a certain amount of stagnated gas within the fields of view of the spectrometers. Whilst this will not adversely affect the rapid variations in SO₂ flux that we are interested in, it is important to realise that the fluxes reported here may be overestimates compared to the true values.

5.2.3 Gas Composition

Open-path absorption spectra of the gas emissions were collected with a MIDAC Corporation M-4402-1 FTIR spectrometer sited on the crater rim, with the lava lake, ~ 330 m line-of-sight distant, acting as infrared source [Oppenheimer and Kyle, 2008, Oppenheimer et al., 2011]. All interferograms were recorded with a time step of 1.7 s and a nominal 0.5 cm⁻¹ spectral resolution. The measurements presented here were made in December 2013. Retrievals of the species recognised in the absorption spectra were made from transformed interferograms using a code that simulates and fits atmospheric transmittance in discrete wavebands [Burton et al., 2000], specifically

2020–2100 cm^{-1} for H_2O , CO_2 , CO and OCS . Uncertainties on these measurements are typically about 5% [e.g. Horrocks et al., 2001]. Gas ratios are calculated from the raw column amounts after corrections are made for contributions of atmospheric water and CO_2 [Oppenheimer and Kyle, 2008]. This procedure works particularly well in this setting owing to the hyperarid background atmosphere.

We inspected the ratios of all possible pairs of the seven magmatic gas species detected and found that the CO_2/OCS ratio most clearly revealed the cyclic variation sought. We have therefore focused on this quantity for the purposes of the multi-parameter inter-comparison sought here.

5.2.4 Lava Lake Surface Elevation

An Optec ILRIS 3D terrestrial laser scanner was used to survey the lava lake surface from the same location on the crater rim as the thermal camera and FTIR spectrometer. The scanner uses a near-infrared laser (1535 nm wavelength), with a scanning frequency of 2.5 kHz. At a distance of 300 m (the approximate distance to the lake’s surface), the spot diameter of the laser beam is ~ 7 cm. The scanner was connected to a Trimble GPS pulse-per-second signal to provide accurate time stamps for each data point.

The data used in this study consists of a series of repeated 30-s-duration scans, focused on the lava lake surface. Scan data from within a circular region of 4 m diameter, approximately centred in the middle of the lake, is averaged and used as a measure of lake surface elevation. The density of points within the averaged region is variable due to changing plume conditions, however, it typically contains around 90 measurements. The time taken to record these measurements (< 2 s) is small compared to the timescale of change in lake surface elevation.

5.3 Results

Although cyclic behaviour is observed in many of the gas ratios measured with the FTIR [Ilanko et al., 2014], in the 2013 dataset they are most apparent in the CO_2/OCS ratio time series and we therefore use this ratio to characterise the changing gas chemistry. Figure 5.3 shows four three-hour time series of mean lake surface speed and CO_2/OCS ratio from 6, 12 and 13 December 2013. Each three-hour

sequence contains a large (lake-emptying) explosion. These are highlighted, and inset sequences of thermal images show the progression of each event with a ~ 2 s time-step. The correlation between the gas ratio and speed data is striking, and clearly demonstrates that the cyclic behaviour of the two properties must be inherently linked. Periods where there is no obvious correlation (e.g. around 16:00 on 12 December) correspond to times where there are no appreciable cycles in the time series. Although there are periods where the peak in mean speed clearly precedes the peak in CO_2/OCS ratio (e.g. 18:30 on 6 December 2013), there are also periods where the converse is true (e.g. 11:50 on 6 December 2013). A windowed correlation analysis confirmed that there was no consistent lag between the signals. Given the potentially complex coupling between the underlying mechanism driving the pulsatory behaviour and the properties being measured, this is perhaps to be expected.

The large explosions shown in Fig. 5.3 do not appear to have any significant impact on the cyclic behaviour of the lake. Following a short period (~ 5 min, corresponding to the time-scale of lake refill) of elevated speed and CO_2/OCS ratio, both time series are seen to return to similar values as prior to the explosion and resume their pulsatory behaviour. No obvious changes in the period or amplitude of the cycles following an explosion are apparent.

Figure 5.4 shows a little over two hours of SO_2 flux, CO_2/OCS ratio and mean lake surface speed data collected on 14 December 2013. The SO_2 flux data have been offset by -3 min to account for the time taken for gas emitted at the lake's surface to rise to within the DW-FOV DOAS instrument's field of view, a distance of ~ 500 m (the mean rise speed measured with the DW-FOV DOAS was 2.7 ms^{-1} , giving a rise time of ~ 3 min from the lake's surface to the field of view of the DW-FOV DOAS instrument). However, it is important to realise that this is an approximation, and the variability of the true delay time will result not only in a shift of the measured flux compared to the real flux, but also in compression or rarefaction. The correlation of the SO_2 flux with the other signals is contingent on inhomogeneities in gas flux at the lake's surface rising coherently until they can be measured with the DW-FOV DOAS. Turbulence and mixing in the lower portions of the plume are likely to disrupt any structure in the emissions from the lake, and we believe that this may account for the rather poor correlation of the data series at some times. Despite this, the general agreement between the three time series is compelling, and provides very strong evidence for the fluctuations in SO_2 flux being driven by the same underlying mechanism as those in the gas composition and lake surface mo-

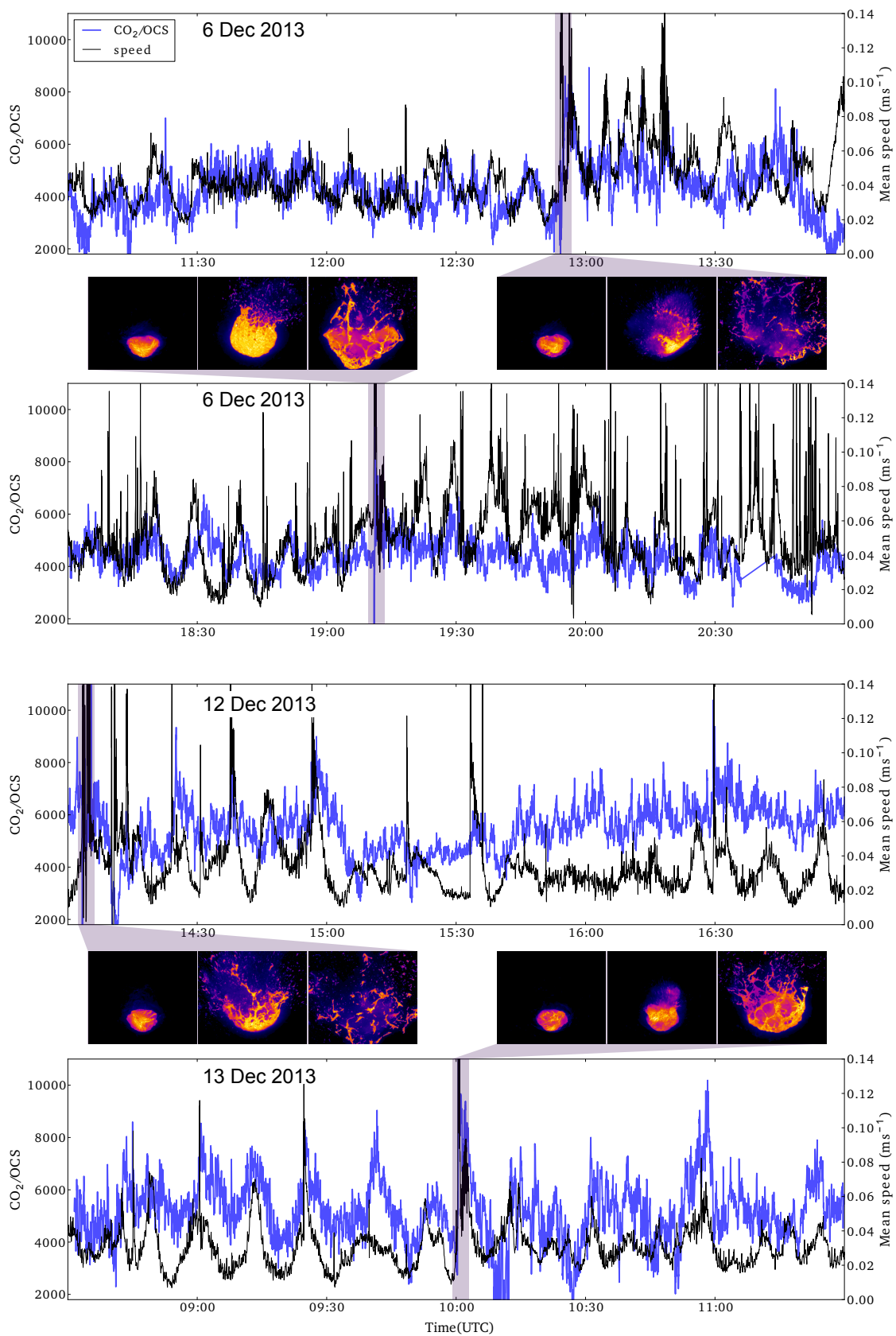


Figure 5.3: Comparison between the CO_2/OCS ratio measured with the FTIR and the mean speed of the lake surface. IR images show the progression of explosive events at a ~ 2 s timestep.

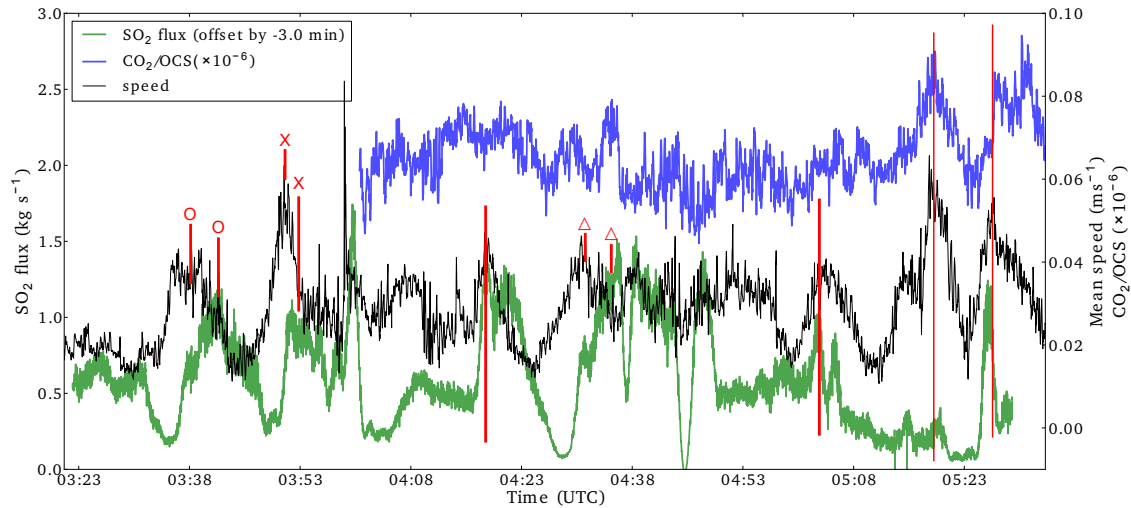


Figure 5.4: Data from the 14 December 2013 showing the correlation between SO_2 flux, CO_2/OCS ratio and the mean speed of the lava lake surface. Cycles with particularly good correlation are marked.

tion. Peaks in SO_2 flux are observed to coincide with peaks in lake surface speed. However, given the uncertainty in the time delay between gas being emitted from the lake to when it is measured, particularly since this will vary with time, it is not possible to investigate the alignment of peaks in any greater detail and there may well be short lags between the signals which are not resolvable. There were no explosions during the acquisition period of the SO_2 flux data, so we cannot comment on how they might influence the flux.

A ~ 7 h time-series of mean lake surface speed and lake surface elevation recorded on 17 December 2012 is shown in Fig. 5.5. Again, the correlation between the cyclicity in both properties is clearly visible. The sequence of IR images in the figure show the progression of the large bubble burst that occurred at 17:24 UTC. Immediately following the explosion, there is a ~ 2 min gap in the TLS acquisition due to the lake being obscured by the fumes from the explosion. The lake is then seen to refill rapidly over the next ~ 3 min and subsequently resume a pulsatory behaviour which is indistinguishable from that exhibited prior to the explosion. This recovery time is consistent with that of the large bubble events highlighted in Fig. 5.3 as is the fact that the pulsatory behaviour does not appear to be influenced by the explosions beyond the timescale of lake refill.

Also evident in Fig. 5.5 and shown more clearly in Fig. 5.6, is that the peak in surface speed occurs after the peak in surface elevation. Figure 5.7a shows the results of a windowed cross-correlation of the two series (as described in Section 5.2.2) using

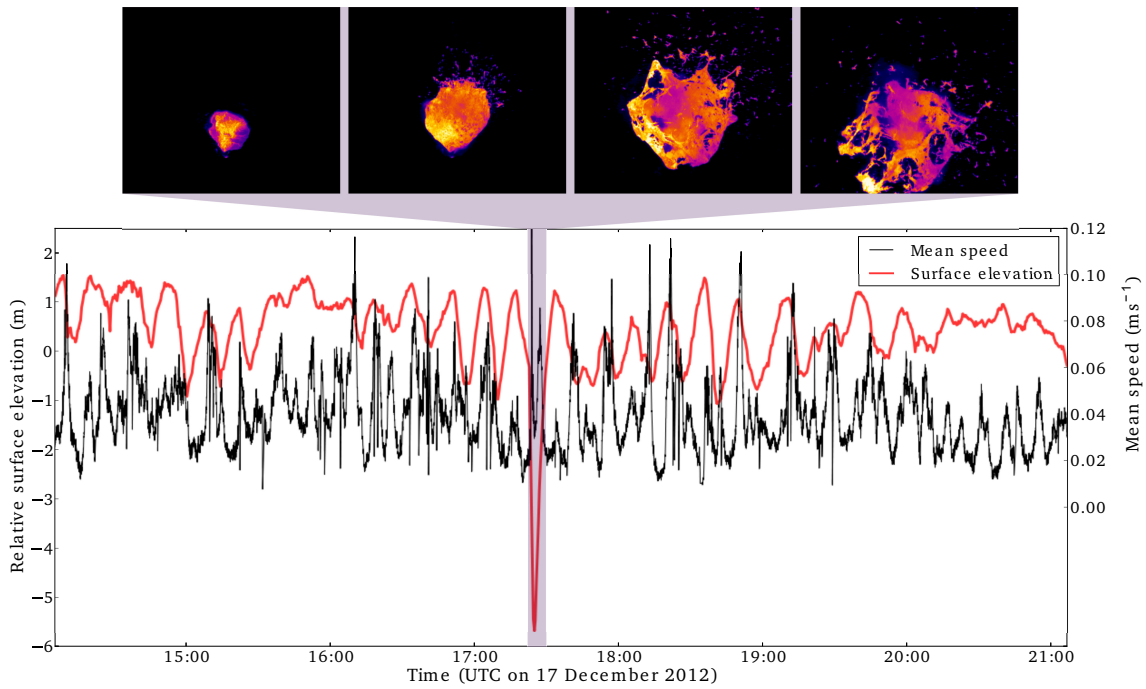


Figure 5.5: Data from 17 December 2012, showing the surface elevation of the lake (measured using TLS) and the mean surface speed (estimated from IR images). IR images show the progression of a large explosion that occurs at 17:24 with a timestep of ~ 2 s.

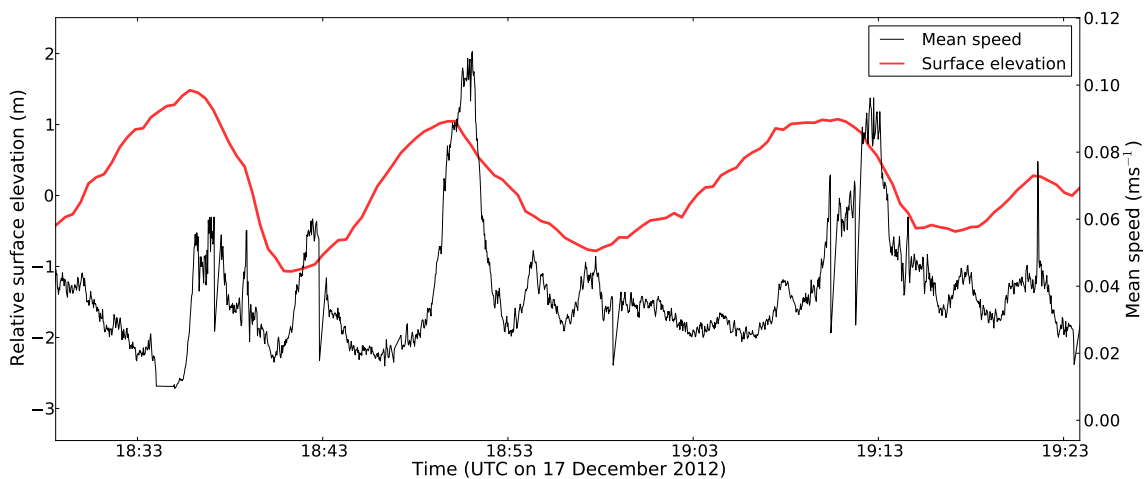


Figure 5.6: Expanded section of the data presented in Fig. 5.5, showing the lag between the surface elevation and surface speed of the lake.

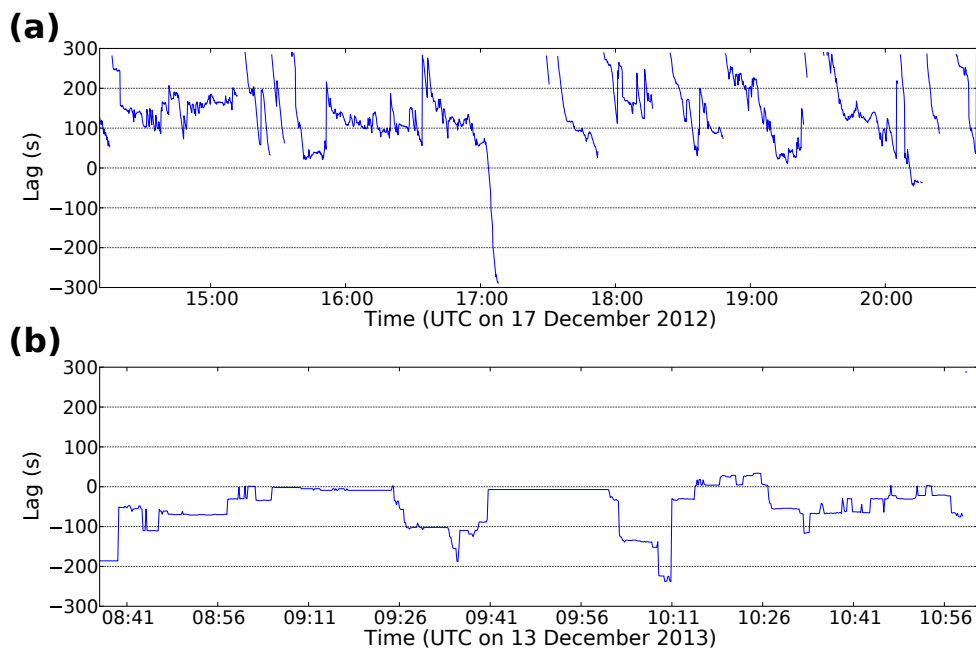


Figure 5.7: Results of a windowed cross-correlation using a window length of 1200 s of: **(a)** the lake surface speed and the surface elevation on 17 December 2012; **(b)** lake surface speed and CO_2/OCS molar ratio on 13 December 2013. The plotted data are the lags corresponding to the maximum in the cross-correlation at each time step and therefore represent the lag between the two data series.

a window length of 1200 s and shows that the surface speed typically lags the the surface elevation by 1–3 min. This contrasts with the relationship between the surface speed and CO₂/OCS ratio (Fig. 5.7b), which are generally in phase with each other. Periods when the time series were very dissimilar and could therefore not be cross-correlated successfully (e.g. due to the explosion at 17:24 on 17 December 2012) have been omitted from the figure for clarity.

5.4 Discussion

Given the apparent complexity of Erebus’s shallow magmatic system [e.g. Zandomenighi et al., 2013] and the sensitivity of multi-phase flows to small changes in system parameters [e.g. Molina et al., 2012], the regularity and longevity of the cyclic behaviour of the lava lake is somewhat surprising. That such disparate methodologies as FTIR spectroscopy, motion estimation and DW-FOV DOAS are not only all capable of independently detecting this behaviour but also demonstrate such a striking correlation with each other, is remarkable, particularly given the challenging conditions under which the data were collected. The correlation between the different data provides persuasive evidence that the cycles are not an artefact of the measurement techniques.

Fig. 5.7 shows that the cycles in CO₂/OCS ratio are in-phase with those in the lake’s surface speed. In other words, the CO₂/OCS ratio reaches its peak when the lake motion is most vigorous, and its trough when the lake is most sluggish. This raises the important question as to why the CO₂/OCS ratio is varying. A comprehensive analysis of the gas composition cycles is forthcoming in Ilanko et al. [2014] but we note here that the two species are related through the following redox equilibrium:



Whose equilibrium constant, K_1 is given by:

$$K_1 = \frac{x_{\text{OCS}}x_{\text{CO}_2}^2}{x_{\text{CO}}^3x_{\text{SO}_2}} \cdot P^{-1} \quad (5.3)$$

where x_a is the mole fraction of species a and P is the pressure.

We can also consider the equilibrium between CO₂ and CO as follows:



For which the equilibrium constant is given by:

$$K_2 = \frac{x_{\text{CO}_2}}{x_{\text{CO}} \sqrt{f_{\text{O}_2}}} \quad (5.5)$$

Rearranging, we can write the CO_2/OCS molar ratio as:

$$\frac{x_{\text{CO}_2}}{x_{\text{OCS}}} = \frac{K_2^3}{K_1} \cdot \frac{f_{\text{O}_2}^{\frac{3}{2}}}{x_{\text{SO}_2}} \cdot P^{-1} \quad (5.6)$$

There are thus several factors that can influence the CO_2/OCS ratio, including temperature (the equilibrium constants are temperature-dependent), oxygen fugacity and pressure, in addition to the mole fraction of SO_2 in the gas phase (itself dependent on redox conditions, temperature and pressure). The system is under-determined but can be solved if we assume (i) the measured gases represent an equilibrium composition, and (ii) one of the unknown parameters. In this case, we make the assumption that the gases are equilibrated at atmospheric pressure. This enables us to compute, spectrum by spectrum, the equilibrium temperature and oxygen fugacity. Under these assumptions, we may conclude that the cycles represent variation of approximately 0.1 log units relative to the rock buffer Quartz-Fayalite-Magnetite (QFM; Fig. 5.8). This does not explain the origin of this variation but provides compelling evidence for a close association between magma degassing, redox conditions and the fluid dynamics of the lava lake.

Measurements made by Ripepe et al. [2002] on Stromboli, revealed a correlation between increased explosive activity and intensified gas puffing. Periods where degassing consisted of vigorous puffing were found to coincide with a high number of Strombolian explosions, whereas periods with a low number of Strombolian events were characterised by fewer, lower-velocity gas puffs. Stromboli alternates between these two different degassing regimes on timescales of 5–40 min, not dissimilar to the ~ 5 –18 min cycles in SO_2 flux observed on Erebus. Ripepe et al. [2002] proposed that the observed behaviour at Stromboli was due to changes in the gas supply rate into a shallow foam layer. On Erebus however, no correlation between explosive activity and passive degassing behaviour is observed. Large (decametric) bubbles are too infrequent to correlate with the cyclicity in the gas flux. For example, cyclic variations in SO_2 flux were observed in the data presented in Fig. 5.4, during a period when no large bubbles were recorded. Although smaller (metre-scale) bubbles

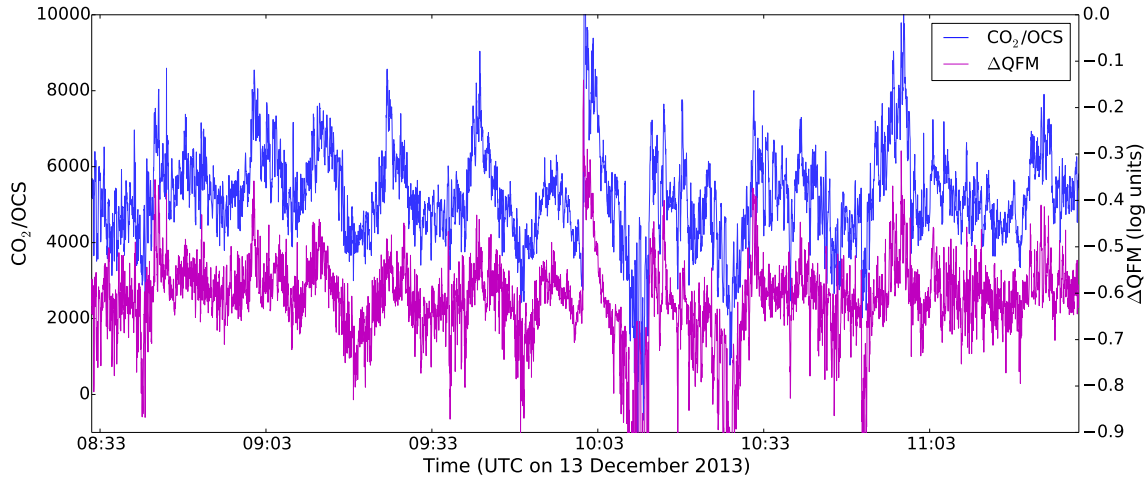


Figure 5.8: Comparison of the CO_2/OCS molar ratio on 13 December 2013 and the computed oxygen fugacity at which the gas equilibrated (relative to the QFM buffer).

occur on a similar time-scale to that of the cycles in SO_2 flux, these have been found to be uncorrelated with the fluctuations in surface speed [Chapter 4, Peters et al., 2014d] and by inference therefore, also with variations in the gas flux. Explosive activity on Erebus appears to be entirely decoupled from its passive degassing behaviour. This is consistent with the findings of Burgisser et al. [2012], who propose that while explosive degassing at Erebus is due to rupture of gas bubbles that rise from depth independently of the melt, its passive degassing is dominated by exsolved and exsolving volatiles from magma in the lake itself. This would suggest that the fluctuations in SO_2 flux observed at Erebus (Fig. 5.4) are due to changes in supply of gas-rich magma into the shallow system. However, in contrast to the mechanism proposed by Ripepe et al. [2002] for Stromboli, we argue that significant gas accumulation at a shallow level does not occur at Erebus. This prevents large bubbles from forming in the shallow system due to coalescence, allowing significant changes in SO_2 flux without any changes in explosive activity.

A high degree of gas permeability of the Erebus lava lake was also proposed by Peters et al. [2014d] (see also Chapter 4). This argument can be strengthened by considering the emissions that occur during a single cycle. From the TLS data (e.g. Fig. 5.5) we can see that a change in surface elevation of ~ 2 m is typical during a single cycle. Treating the upper part of the lake basin as cylindrical, with a surface area of ~ 400 m^2 (its 2012 size), this represents a volume change of 800 m^3 . The additional amount of SO_2 released during a single cycle (above the background SO_2 emission rate) is ~ 5300 mol (found by integrating the flux data in Fig. 5.4). FTIR

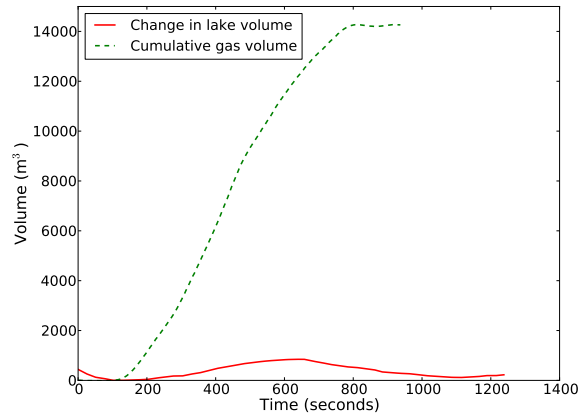


Figure 5.9: Comparison of the volume change of the lava lake and the additional volume (at atmospheric pressure) of gas released (above the background level) during a single cycle.

measurements indicate a typical SO_2 /total-gas molar ratio of ~ 113 , giving a total gas output of $1.4 \times 10^4 \text{ m}^3$ in a single cycle (assuming standard temperature and pressure). These results are summarised in Fig. 5.9, which shows a comparison between the volume of gas released and the volume change of the lake during a single cycle. It should be noted that overlapping SO_2 flux data and TLS data are not yet available, and so whilst the lake volume data are from 17 December 2012, the gas volume data are calculated from SO_2 flux data recorded on 14 December 2013. However, since inter-annual variability in surface elevation variations and SO_2 flux is small at Erebus [Sweeney et al., 2008, Jones, 2013], it is reasonable to compare these data. The data show that the total volume of gas released during a single cycle is an order of magnitude greater than the volume change of the lake, supporting the argument that the lake must be highly permeable to gas.

The 1–3 min lag between the peak in surface motion (and therefore also in gas composition) and the peak in surface elevation may be indicative of the dwell-time of gas in the lake. The lag may be explained by the time taken for fresh pulses of magma injected into the lake to rise to the surface, but this would suggest that gas escaping at the surface has travelled with the melt rather than rising independently through the lake. It is important to remember however, that even at the low-point of the cycles there is a net gas flux. If bubbles are not rising independently of the melt, then there must be a sustained transfer of magma to the surface of the lake. Since the surface motion is not seen to stagnate, this seems feasible. However, the definition of “surface” in this argument is rather unclear, and it is not yet possible to constrain either the depth at which magma motion might influence the surface motion measured with the thermal camera, or the depth at which the gas might

separate from the magma.

Witham and Llewelin [2006] showed that stable lava lake systems would rapidly return to equilibrium following a perturbation. This is indeed what is observed in the Erebus lake, with a rapid return to “normal” behaviour following explosive events. It is interesting to note that the refill following an explosion does not appear to “overshoot” the maximum lake level reached during periods of quiescence. Recovery from an explosion is rapid, and shows that the response of the lake system to a perturbation is much faster than the time-scale of the pulsatory behaviour. This would suggest that the recorded waveform of the cycles in surface elevation (which must be a convolution of the lake’s response function and the driving mechanism’s waveform) are representative of the underlying process responsible for the cycles and has not been overly smoothed due to a sluggish response of the lake system. Although the waveforms of the surface motion and gas composition indicate that the observed cyclicity is caused by periodic perturbations to a system that is otherwise at equilibrium [Chapter 4, Peters et al., 2014d], the surface elevation appears to be approximately symmetric about its mean, indicating a system that is oscillating about its equilibrium state. It seems likely that the surface elevation of the lake is a more “direct” measure of the underlying process responsible for the pulsatory behaviour and we therefore believe it to be an oscillatory mechanism rather than an impulsive one. One possible explanation is that the base of the lake is maintained at magmastic equilibrium. Fluctuations in surface elevation balance changes in the bulk density of the lake caused by injection of bubbly (lower density) magma from the conduit, and gas loss at the surface.

In Chapter 4, we noted that whilst the cycles in surface speed were not always clear, there did always appear to be some periodicity present, concluding that the pulsatory behaviour was a sustained feature of the lake. These findings are supported by the data presented here. In particular, Fig. 5.5 (e.g. between 20:10 and 21:00) demonstrates that even when pulsatory behaviour in the lake surface level is not evident, there are still clear cycles in the surface speed. A similar phenomenon is shown in Fig. 5.4 (e.g. between 04:08 and 05:08) where cycles are apparent in the surface speed, but not in the CO_2/OCS ratio. It is curious that at different times, cyclic behaviour may be present in some properties but not others. We attribute this behaviour to the fact that each property being measured is a different surface manifestation of a common underlying periodic (or pseudo-periodic) process. The coupling between the underlying process and the measured quantity could be ex-

tremely complex, and also susceptible to other forcing mechanisms. The clearest example of this is the SO_2 flux measurements. Even if the flux of SO_2 is perfectly periodic at the lake's surface, changing atmospheric conditions within the crater will alter how visible this periodicity is at the point of measurement and under certain circumstances plume transport dynamics may dominate the flux, masking the periodic signal entirely. A similar argument may be made for the FTIR measurements, where the measured composition may be influenced by an accumulation of gases within the crater over the time-scale of one lake cycle. In the case of the surface elevation and surface speed measurements, it is possible that other processes within the lake (e.g. thermal convection or foam formation) can overshadow the mechanism responsible for the pulsatory behaviour, concealing its influence.

The discovery of periodic degassing at Mt. Etna in Sicily [Tamburello et al., 2013, Pering et al., 2014], raises the possibility that, despite the differences in magma viscosities, the models of magma flow being developed to explain the pulsatory behaviour of the Erebus lava lake may be more widely applicable to open-vent volcanoes around the world. However, some care is needed when assessing periodic degassing since it is possible that the development of turbulence within the plume between the vent and the point of measurement (often a few hundred meters) could cause a periodicity in the measured flux, even if the source is constant. In the data presented here, we believe that this is not the case, as it would seem an unlikely coincidence for turbulence effects to be so well correlated with the cycles occurring in plume chemistry and lake surface motion.

5.5 Conclusions

In this chapter, we have presented measurements made during December 2012 and December 2013 of the SO_2 flux, CO_2/OCS ratio, surface elevation and mean surface speed of the Erebus lava lake. Well established methodologies (UV and FTIR spectroscopy, TLS and motion estimation from thermal imagery), which have been used during numerous previous field campaigns on Erebus, were employed. However, the unprecedented overlap in the time series presented has enabled us to show for the first time a definitive link between the pseudo-periodic fluctuations observed in each of these properties. Cycles (with an approximate period of 10 min) in SO_2 flux, CO_2/OCS ratio, oxygen fugacity and mean surface speed were shown to be correlated, and in-phase with each other, providing strong evidence for a common

underlying mechanism. The cycles in surface speed were found to lag cycles in surface elevation by 1–3 min. The volume of gas released during a single cycle (above the background gas flux) is an order of magnitude greater than the associated change in lake volume. This suggests that gas is effectively lost from the lake as soon as it has entered. Large explosions appeared to have no appreciable effect on the pulsatory behaviour observed, at least beyond the time taken for the lake to refill to its normal level (~ 5 min). However, insufficient events were analysed to rule out the possibility of subtle changes to the behaviour caused by large gas bubbles, leaving this as an interesting avenue for future investigation.

Chapter 6

Analysis of the 2D Surface Velocity of the Erebus Lava Lake

This chapter looks in more detail at the structure of the velocity field over the surface of the Erebus lava lake. Whereas the previous chapters have focused on the mean velocity, here we examine the 2D velocity field using a combination of vector plots and the divergence of the flow. Time periods from both 2004 and 2013 are analysed and found to have similar flow patterns despite the dramatic change in lake surface area between the years. The flow typically consists of flow from a single principal source region to a single principal sink region. No variation in flow structure is observed during the cycles in the lake's behaviour, nor does it appear different during periods of little cyclic activity. The observations fit well with the bi-directional flow mechanism proposed by Oppenheimer et al. [2009], however, they also imply that there is a continuous flow of magma into the lake and that the observed pulsatory behaviour is due to periodic intensifications of this flow.

6.1 Introduction

The previous chapters of this thesis have focused primarily on the study of spatially-averaged metrics of the behaviour of the Erebus lava lake. In Chapter 4, we used mean surface speed to analyse inter-annual variability in the lake’s behaviour and in Chapter 5 we combined the mean speed data with other “bulk property” measurements such as SO_2 flux and mean surface elevation to demonstrate how the behaviours of these properties are linked. However, inherent in the method of computing the mean surface speed of the lake (see Section 4.2.3), is the calculation of the two-dimensional velocity field over the whole of the lake’s surface. The analysis presented previously has therefore discarded much of the information that is available from the IR dataset.

In this chapter, we revisit the velocity fields calculated in the previous chapters and look in more detail at the two-dimensional structure of flow at the lake’s surface. The flow structure is evaluated across complete cycles in mean lake surface speed for data collected in both 2004 and 2013. As discussed in Chapter 4, despite the significant change in lake surface area between 2004 and 2013, the overall behaviour of the lake remained similar, with ~ 5 –20 min period cyclicality evident. We also compare the flow structure between a time period in 2013 with no evident cyclicality and a ensuing period demonstrating strongly cyclic behaviour. The structure of the flow during these periods is analysed using both vector plots and plots of the divergence of the flow field.

6.2 Methodology

The IR images analysed in this chapter were collected using the same thermal camera systems as described in Chapter 4 [see also Peters et al., 2014d]. The calculation of the lake surface velocities followed the same methodology as used in the previous chapters (see Section 4.2.3).

6.2.1 Data Selection

Time periods for analysis were chosen by considering plots of the mean surface speed of the lake (e.g. Fig. 5.3). Periods where the cyclic behaviour was particularly evident were used in order to demonstrate how the velocity field changed during the

progression of a cycle. Data from both December 2004 and December 2013 were used in order to compare the velocity fields for different sizes of lake ($\sim 2300 \text{ m}^2$ in 2004 and $\sim 580 \text{ m}^2$ in 2013).

A period of data from 15:45–16:45 UTC on 12 December 2013 was also chosen for analysis as it shows a transition between a period of no evident cyclicity and well defined cycles (see Fig. 5.3).

Visibility of the lake was good during all time periods used (low humidity in the crater) and there was no apparent camera shake.

6.2.2 Divergence

Evaluating temporal changes in a 2D velocity field is challenging due to the difficulty of visualising such data. In previous chapters, this issue was addressed by summarising the velocity field using its mean. However, this gives little information about the structure of the velocity field. Here, we use the divergence of the velocity field as a means of assessing the progression of the surface motion of the lake. Divergence was chosen since it not only provides information about the 2D structure of the velocity field, but also has a simple physical interpretation.

Given a 2D vector function of the form $\mathbf{V}(x, y)$, the divergence of the function is defined [e.g. Boas, 1983b] as:

$$\text{div } \mathbf{V} = \nabla \cdot \mathbf{V} = \frac{\partial V_x}{\partial x} + \frac{\partial V_y}{\partial y} \quad (6.1)$$

The physical interpretation of the divergence at a particular point is the extent to which that point behaves as a source or sink. A point in a vector field with positive divergence is a source, whereas negative divergence indicates a sink region. In the context of lake surface motion (where the vector field under consideration is the displacement field), source regions correspond to spreading centres associated with lava up-welling and sink regions correspond to “subduction zones” associated with lava down-welling.

6.3 Results

Figure 6.1 shows a short time series of mean lake surface speed calculated from IR images recorded on 17 December 2004. On this date, the lake was $\sim 2300 \text{ m}^2$ in size. The time series spans a single cycle in mean speed and plots of the 2D flow field and its associated divergence are shown at different points in the cycle. Although the flow field is rather complex, with many source and sink regions, the majority of these are transient and the flow structure is dominated by flow from a source region in the upper right of the lake to a sink region in the lower left. This flow structure is consistent across cycles in the mean surface speed of the lake.

Figure 6.2 shows how the 2D velocity field and its divergence changes across a single cycle in mean speed on 13 December 2013. At this time, the lake was $\sim 580 \text{ m}^2$ in size, just a quarter of its size in 2004. The data are generally smoother than those shown in Fig. 6.1. This is likely due to the superior temporal and spatial resolution of the thermal camera system used in 2013 compared to that of 2004 (0.5 Hz and 640×480 pixels compared to 0.25 Hz and 320×240 pixels). The figure shows that the lake surface has one pronounced source region (lower left) and one pronounced sink region (upper right). The configuration of these regions does not change throughout the duration of the cycle in mean speed. There is no reversal of the flow between the leading and trailing edges of the peak in mean speed. The source and sink regions are observed to intensify at the peak of the cycle. However, this is to be expected given the increase in magnitude of the surface speeds.

Figure 6.3 shows the 2D velocity field and associated divergence at different times during a ~ 1.25 hr period of mean surface speed data on 12 December 2013. During the first ~ 30 min of the timeseries there is no apparent cyclic behaviour in the lake's mean surface speed, whereas, for the latter part of the timeseries there are clearly defined cycles. Despite this dramatic change, the structure of the velocity field varies little across the transition in behaviour of the lake, with flow being predominantly from a source region in the lower left to a sink region in the upper right. As can be seen from the plot of mean speed in the figure, during the period with no cyclic behaviour, the mean speed of the lake's surface is comparable to the troughs in mean speed during the period with well defined cycles.

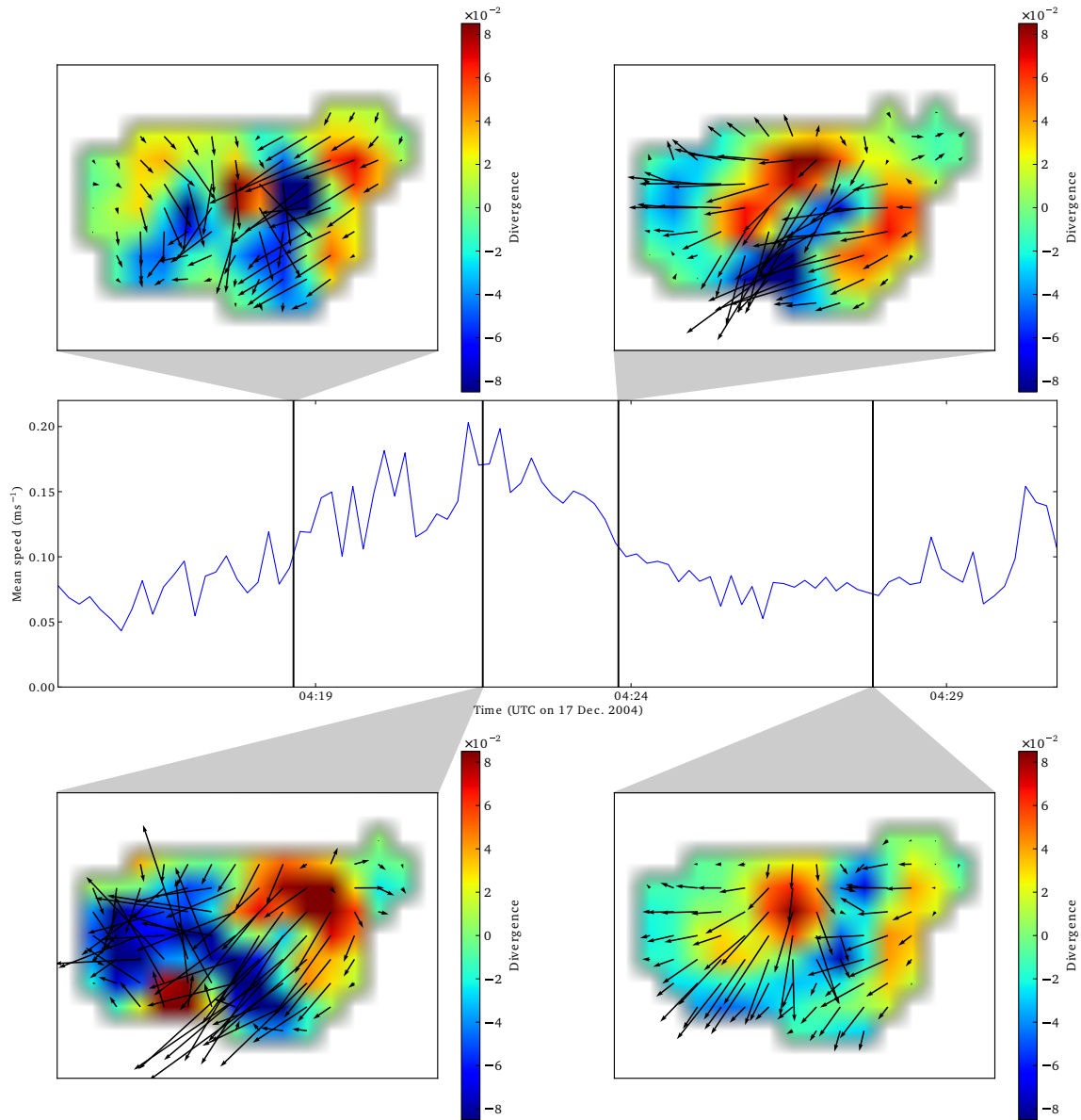


Figure 6.1: Comparison of the 2D velocity field (black arrows) and associated divergence (colour scale) across a single cycle in the mean surface speed of the lake computed from IR images recorded on 17 December 2004. A positive divergence (red) is indicative of a spreading/up-welling region while a negative divergence (blue) indicates a converging/down-welling region. Arrow lengths are proportional to speed.

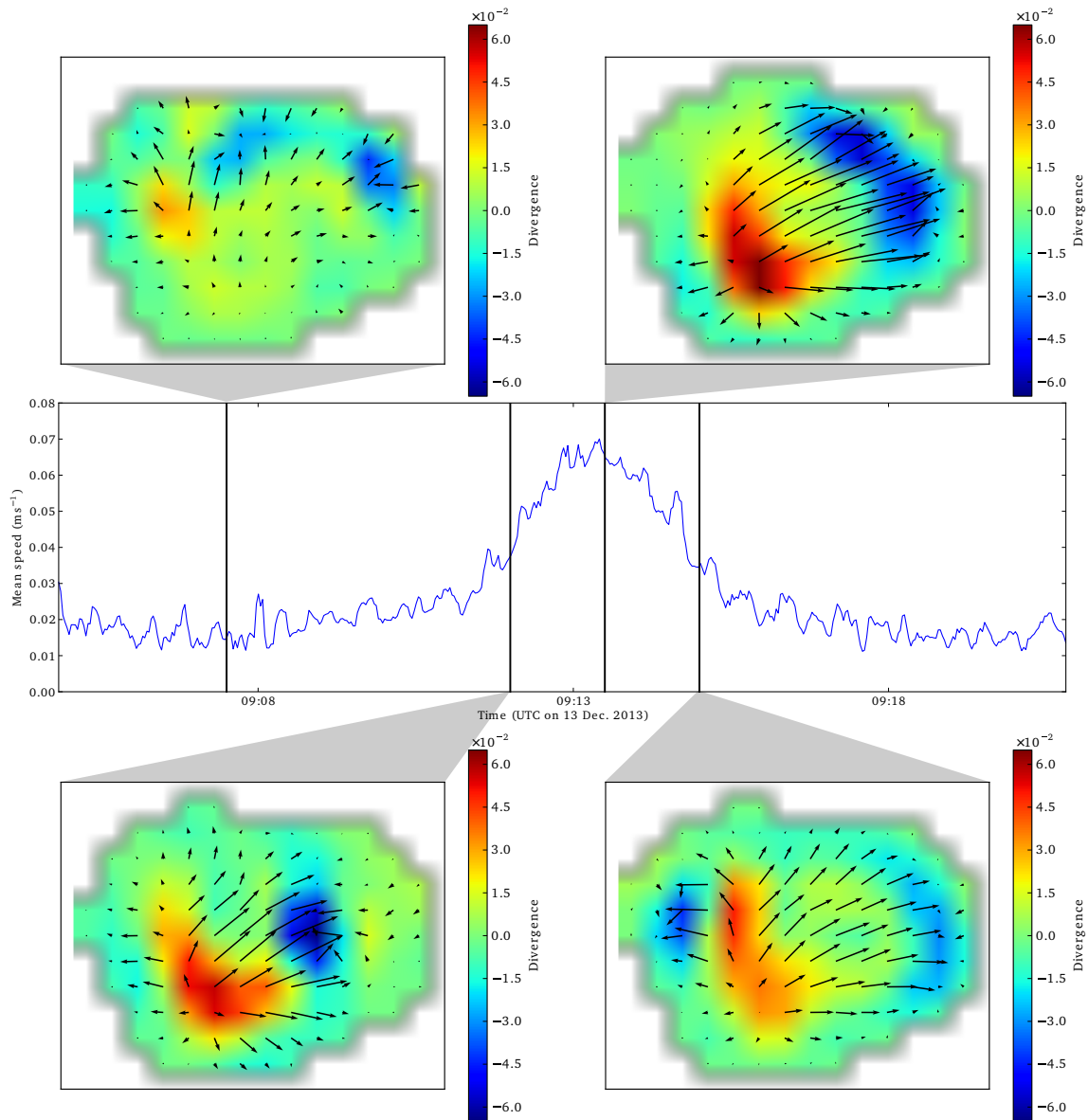


Figure 6.2: Comparison of the 2D velocity field (black arrows) and associated divergence (colour scale) across a single cycle in the mean surface speed of the lake computed from IR images recorded on 13 December 2013. A positive divergence (red) is indicative of a spreading/up-welling region while a negative divergence (blue) indicates a converging/down-welling region. Arrow lengths are proportional to speed.

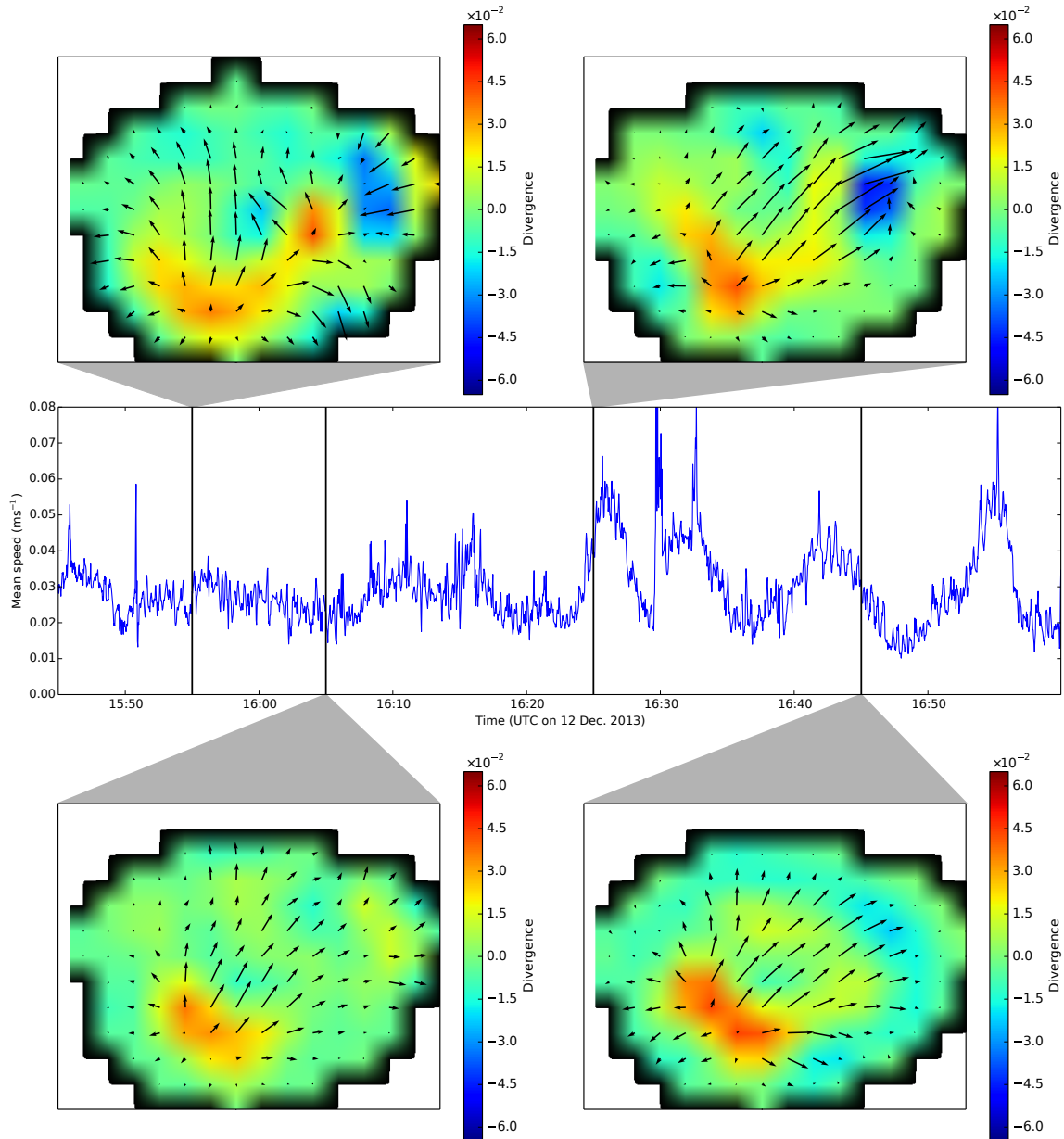


Figure 6.3: Comparison of the 2D velocity field (black arrows) and associated divergence (colour scale) between a time period with no apparent cyclic behaviour (15:45 – 16:25 UTC) and a time period with well defined cycles (16:25 – 17:00 UTC) on 12 December 2013.

6.4 Discussion

When comparing the divergence fields calculated from images from 2004 to those of 2013 it is tempting to conclude that the principal up-welling region, and therefore the location of the conduit, has moved from the upper-right to the lower-left of the lake. However, it is important to remember that the fields of view of the camera systems recording the images are different between the two years, and there is no way to assess how the lake boundaries in each year relate to each other. Given the fairly rapid variations in the topography of Erebus's inner crater that have been observed [Jones, 2013], it seems plausible that the positioning of the conduit could vary between years. However, there is insufficient data to rule out the possibility that the conduit remains fixed, and that it is the relative position of the lake that changes.

Peters et al. [2014d] (see also Section 4.3) found that the CDF of bubble events is shifted towards higher mean speeds than a reference of random samples of lake speeds, suggesting that bubbles tend to surface when the lake surface is moving faster than average. This was attributed to the failure of the low-pass filter used in the analysis to completely remove the spikes in speed caused by the bubble events. However, animations of the 2D velocity plots and associated divergences (available on request) show that, following a bubble, there is rapid flow into the void space left by the bubble. Although very localised, this region of high velocity will skew the mean speed value, and may account partially for the offset of the CDF.

In Section 1.4, proposed mechanisms for lava lake degassing were discussed. In Chapter 4, we discounted the gas pistoning and bubble-driven pressurisation changes as candidates for the Erebus system based on the absence of periodic gas releases from the lake and also because of the symmetry of the Erebus cycles in time. The structure of the velocity field supports these conclusions, since both aforementioned mechanisms require uni-directional upflow followed by uni-directional downflow of magma in the conduit. No reversal of the surface flow pattern of the lake is observed, suggesting that these mechanisms are not active at Erebus.

The observed flow structure at Erebus is indicative of a stable and continuous exchange flow between the lava lake and the deeper magmatic system. The cycles that are observed are due to an intensification of this flow rather than a change in flow regime. Such observations are not at odds with the bi-directional flow mechanism proposed by Oppenheimer et al. [2009], however, what is not made clear by Oppenheimer et al. [2009] is that underpinning the pulsatory flow of magma into the

lake is a relatively stable baseline flow which is present even when cyclic behaviour is not. Furthermore, it is possible, given the frequency of bubble events presented in Chapter 4, that the perturbations to the baseline flow are caused by detached bubble wakes rather than flow instability. However, this hypothesis seems less likely since cycles are occasionally observed without any evidence of bubbles arriving at the surface (e.g. Figure 4.7).

6.5 Conclusions

In this chapter, we have presented estimates of the surface velocity field of the Erebus lava lake in December 2004 and December 2013. The same motion estimation methodology as employed in Chapter 4 and Chapter 5 was used. However, here, the structure of the flow field was analysed rather than just the mean surface velocity. In addition to vector plots of the surface velocities, the divergence of the flow field was used as a tool to assess changes in its structure. It was found that the flow field did not change in structure during the course of a cycle. Specifically, there was no reversal of flow or changes in the number of source and sink regions. The surface flow of the lake in 2004 was broadly similar to that in 2013 with one predominant source region and one predominant sink region, despite the large change in lake surface area between the years. The structure of the surface flow field was found to be similar between periods of strongly cyclic activity and periods of little cyclicality.

The continuity of the upwelling region in the lake, and lack of evidence for any flow reversal precludes gas pistoning and the Witham et al. [2006] pressurisation change mechanism as being responsible for the observed cyclicality of the lake. Although not directly contradictory to the bi-directional flow model proposed by Oppenheimer et al. [2009] (see also Section 1.4), the results suggest that the pulsatory delivery of magma into the lake is superimposed on top of a relatively stable baseline flow. It appears that the cyclic behaviour of the lake is caused by periodic intensifications of this baseline flow.

Chapter 7

Use of Motion Estimation Algorithms for Improved SO₂ Measurements Using UV Cameras

UV cameras are rapidly gaining popularity as a tool for monitoring SO₂ emissions from volcanoes. A variety of different SO₂ camera systems have been developed with varying patterns of image acquisition in space, time and wavelength. Despite this diversity, there are two steps common to the workflows of most of these systems; aligning images of different wavelengths to calculate apparent absorbance and estimating plume transport speeds, both of which can be achieved using motion estimation algorithms. In this chapter we present two such algorithms, the Dual Tree Complex Wavelet Transform-based algorithm used in the previous chapters and the Farnebäck Optical Flow algorithm. We assess their accuracy using a synthetic dataset created using the numeric cloud-resolving model ATHAM, and then apply them to real world data from Villarrica volcano. Both algorithms are found to perform well and the ATHAM simulations offer useful datasets for benchmarking and validating future algorithms.

The majority of content from this chapter has been published as: Peters, N., A. Hoffmann, T. Barnie, M. Herzog, C. Oppenheimer, “Use of Motion Estimation Algorithms for Improved Flux Measurements Using SO₂ Cameras”, *Journal of Volcanology and Geothermal Research*, in press 2014

The development and execution of the ATHAM model to produce synthetic UV images was conducted entirely by Alex Hoffmann (with supervision from Michael Herzog), and other than providing some advice on initialisation parameters, I did not contribute to this part of the work. The text describing the model (Section 7.2.3) was also written by Alex Hoffmann, and is reproduced here with his consent. All post-processing of the model data (including development of the processing codes), and all other content of this chapter, is my own work.

7.1 Introduction

Ultraviolet (UV) cameras are the latest addition to the family of UV spectroscopy techniques used to measure sulphur dioxide (SO₂) emissions. Since the first volcanological demonstrations [Mori and Burton, 2006, Bluth et al., 2007] they have been used in numerous studies of SO₂ fluxes from volcanoes [e.g. Holland et al., 2011, Tamburello et al., 2011, Campion et al., 2012, Smekens et al., 2013, La Spina et al., 2013]. Using UV cameras, estimates of SO₂ flux at ~ 1 s temporal resolution are possible, enabling studies of highly dynamic degassing events such as Strombolian eruptions [Tamburello et al., 2012, Dalton et al., 2009, Mori and Burton, 2009] and pulsatory degassing [Tamburello et al., 2013, Pering et al., 2014].

In order to measure SO₂, UV cameras typically use bandpass filters to image at two narrow wavebands, one within and one outside-of an absorption band of SO₂ (typically 310 and 330 nm respectively). The cameras operate on the principle that the apparent absorbance between the two bands will vary only as a function of atmospheric species that absorb unequally across them [Mori and Burton, 2006]. However, the calibration of apparent absorbance to SO₂ column amount is non-trivial [Kern et al., 2010], and calibration curves are typically estimated from imaging gas cells of known concentration, or UV spectrometer retrievals coincident with a region in the absorption image [Lübcke et al., 2013, Kern et al., 2013].

Images at the two wavebands are either captured simultaneously, necessitating two separate cameras, or sequentially, using a filter wheel to change the recorded waveband for each image. The latter method permits a single camera unit to be used, but at the expense of having a short time delay between the in-band and out-of-band images. Since volcanic plumes are seldom stationary in the atmosphere, this is clearly undesirable. Heterogeneities may have shifted by several pixels between consecutive images, compromising the SO₂ retrieval method described above. Simultaneous capture of images at two wavebands is also problematic, since the retrieval of SO₂ column amounts requires the field of view of each pixel in the in-band image to match that of the corresponding pixel in the out-of-band image. Any misalignment of the optical planes of the two camera units and any differences in lens distortion between them will mean that this is not the case and will lead to errors in the SO₂ column amounts calculated. UV cameras are typically used “in the field” and, as such, are often subjected to rapid temperature changes, vibration and physical shocks. Alignment of optical components to the degree of single-pixel correspondence is simply not practical.

A further problem, also applicable to other gas flux measurement techniques [e.g. McGonigle et al., 2005], is that of estimating plume transport speed. To calculate SO_2 flux from UV camera images, the SO_2 column amounts must be integrated across a transect of the plume and multiplied by the transport speed perpendicular to the transect. Typically, the plume speed is either estimated manually [Bluth et al., 2007], which is unfeasible for long datasets or, more commonly, by cross-correlating the integrated column amount values from two complete transects of the plume at different distances from the vent [Kantzas et al., 2010]. The latter method assumes a uniform velocity field across the entire plume and does not account for complex flow structures or vorticity. One has only to observe a volcanic plume, to realise that this is a poor assumption to make. Boichu et al. [2010] discuss in more detail the compromises that must be made between time- and motion-resolution when using the cross-correlation method. An additional, and perhaps more serious issue, is that the lack of reliable “ground truth” data means that the errors introduced by using this method are largely unconstrained.

Estimating plume speed and accurate registration of images from two separate cameras are essentially the same problem; that of calculating motion vectors which map pixels in one image to their corresponding positions in another. This is a common computer-vision problem, which is addressed by a large number of well-established motion estimation algorithms of varying complexity and trade-offs [e.g. Geiger et al., 2014]. To date, use of these techniques in volcanology has mostly been constrained to estimating lava motion from infrared images [James et al., 2007, Oppenheimer et al., 2009, Lev et al., 2012, Peters et al., 2014d], and their application to UV camera images has so far been limited to the work of Kern et al. [2012] who demonstrated how optical-flow methods may be used to estimate SO_2 flux. We extend this work here by assessing the performance of two different motion estimation algorithms when applied to UV images, both for flux estimation and for registering images from separate cameras. We use both a Dual-Tree Complex Wavelet Transform (DT-CWT) algorithm [Magarey and Kingsbury, 1998], and the Farneback optical-flow algorithm [Farneback, 2003].

As already discussed, a major problem with estimating plume transport speeds is that of validation. With no possibility of accurately measuring plume speed by an alternative method, it is not possible to assess the performance of the techniques being developed to estimate plume speeds, nor is it possible to constrain the errors

which they may introduce. In an attempt to address this issue, we use the Active Tracer High-Resolution Atmospheric Model (ATHAM) run in a two-dimensional configuration to create a set of synthetic images of a volcanic plume from a passively degassing volcano. Algorithms for estimating plume speed can be applied to the synthetic images and the results compared to the “real” velocity field computed by the model, providing a simple method of assessing their performance in the context of volcanic plume observations. We demonstrate the technique with both the DT-CWT and Farneback motion estimation algorithms.

It is not our intent to conduct an in-depth comparison of the many different motion estimation algorithms available, and we acknowledge that more suitable algorithms may exist for use with UV camera images than the two which we present here. Instead, we hope to demonstrate the potential applications and benefits of motion estimation algorithms in volcanic-plume UV imaging, and establish a framework for validating and comparing them within this context.

Our specific aims are threefold: (i) to introduce the ATHAM model as a tool for validating plume transport speed estimation methods, (ii) to present two different motion estimation algorithms which are suitable for use with images from UV cameras and show how they perform on both real and synthetic data, (iii) to demonstrate how these algorithms can be employed to provide accurate registration of images from separate camera units.

7.2 Methodology

7.2.1 Motion Estimation Algorithms

The DT-CWT algorithm works by decomposing images using the Dual-Tree Complex Wavelet Transform [Kingsbury, 2001]. The phase shift between the decomposed subimages of two frames is related to the motion of features between those frames. The algorithm employs an iterative approach, using coarse features to create an initial motion estimate and then refining this using progressively finer-scale features. Full details of the algorithm are given by Magarey and Kingsbury [1998].

The DT-CWT algorithm has been used in previous volcanological studies to estimate the surface motion of the lava lake at Erebus volcano from time series of infrared images [Chapter 4 Oppenheimer et al., 2009, Peters et al., 2014d]. Whilst this is

clearly a very different scenario to that of estimating plume transport speeds from UV images, many of the fundamental problems are the same; identifiable features are often diffuse, transient, and may change significantly between frames. The algorithm copes well under these conditions, and is also robust against the noise introduced by varying amounts of volcanic plume, which degrades the camera’s view of the lake.

The Farneback algorithm works by expressing the local neighbourhoods of each pixel in the images as polynomial expansions. The translations between the polynomial expansions for each successive frame can then be calculated and, by enforcing a certain model of motion (e.g. the affine motion model) the two-dimensional displacement field can be estimated. The Farneback algorithm also employs an iterative approach, with a starting estimate for motion being derived from coarse features and then refined using progressively finer features. The algorithm is described in detail by Farneback [2003].

In this investigation we used the same implementation of the DT-CWT algorithm as in Chapters 4 and 5. MatLab code for this was kindly provided by Prof. Nick Kingsbury at the Engineering Department of the University of Cambridge. We used the implementation of the Farneback algorithm provided by the open-source computer-vision library OpenCV [Bradski, 2000].

Both of these implementations allow several parameters to be set by the user to control the operation of the algorithm. A description of the parameters along with the specific values used for this study are given in Section.7.2.2. Broadly speaking the parameters set both the averaging level and the scale of features used by the algorithms. Selecting higher averaging and larger features will usually result in a more robust (less prone to noise, more tolerant of transient features) motion estimate, but at the expense of a less detailed motion field. Given a set of images for which the motion vectors are known (e.g. the data presented in Figs.7.2 and 7.4), it would be possible to optimise an algorithm’s performance by systematically varying its input parameters and minimising the mean-squared error with respect to the known velocities (e.g. using Levenberg-Marquardt optimisation). However, for this study we have not employed such a rigorous approach and instead selected suitable parameters by “trial and error” using a small subset of our data. We believe this approach to be sufficient to support our conclusions, however, it should be noted that the velocity estimates presented could likely be improved upon by using a more thorough parameter selection process.

7.2.2 Algorithm Parameters

Below, we describe the input parameters for the two motion estimation algorithms, and list the values that were assigned to them for this investigation. We refer to the parameters by the same names as are used in the source-code and documentation for the specific implementations that we used (see Section 7.2.1). Optional parameters that have not been defined below were left set to their default values. Different values were used for the image registration (Fig. 7.10) and the plume speed estimations (Figs. 7.2, 7.4 and 7.8). Both sets of values are listed in the tables below.

DT-CWT Algorithm

Parameter	Value for Flux Estimation	Value for Registration
w	$[-\pi/2.15, -3\pi/2.15]$	$[-\pi/2.15, -3\pi/2.15]$
nit	6	6
$levelsel$	[[6, 4], [6, 3], [5, 3], [5, 3]]	[[4, 4], [4, 3], [4, 3], [4, 3], [4, 2]]
$sizeqfilt$	[4, 2, 2, 1]	[48, 32, 32, 16]
$avlevel$	3	4

Table 7.1: Parameters used with DT-CWT algorithm for both image registration and plume speed estimation.

w Expected phase rotation per sample of the high and low band filters used in the DT-CWT decomposition.

nit Number of iterations of the algorithm. A higher value may lead to a more refined motion estimate, but at the expense of increased computation time.

levelsel Defines the coarsest and finest CWT levels to be used during each iteration. In general it is best to use only the coarse levels for the early iterations, and then gradually expand the range to progressively finer levels. This parameter effectively selects the “size” of the features that are being tracked. Use of larger features often gives estimates that are less prone to noise, but also results in a less detailed velocity field.

sizeqfilt Defines the size of the smoothing filter used at each iteration. A larger filter gives a smoother velocity field, but also causes loss of detail.

avlevel Defines the CWT level which has the same resolution as the velocity estimates.

Farneback Algorithm

Parameter	Value for Flux Estimation	Value for Registration
<i>pyr_scale</i>	0.5	0.5
<i>levels</i>	4	3
<i>winsize</i>	20	15
<i>iterations</i>	5	10
<i>poly_n</i>	7	5
<i>poly_sigma</i>	1.5	1.2
<i>flags</i>	OPTFLOW_FARNEBACK_GAUSSIAN	OPTFLOW_FARNEBACK_GAUSSIAN

Table 7.2: Parameters used with Farneback algorithm for both image registration and plume speed estimation.

pyr_scale Scale factor for each pyramid level compared to the previous.

levels Number of pyramid levels to create. A higher number results in coarser features being used for the initial motion estimate.

winsize Defines the size of the averaging filter used. A larger filter gives a smoother velocity field, but also causes loss of detail.

iterations Defines the number of iterations of the algorithm at each pyramid level. A higher value may lead to a more refined motion estimate, but at the expense of increased computation time.

poly_n Size of the neighbourhood used in the polynomial expansion for each pixel. A higher value results in more robust, but less detailed motion estimates.

poly_sigma The standard deviation of the Gaussian smoothing filter used during the polynomial expansion.

flags Optional parameters. We used the OPTFLOW_FARNEBACK_GAUSSIAN option so that the algorithm uses a Gaussian filter rather than a simple “box” filter. This gives more robust motion estimates at the expense of increased computation time.

7.2.3 Using ATHAM as a Validation Tool

We used the non-hydrostatic, fully compressible, multiphase, mesoscale Active Tracer High-Resolution Atmospheric Model (ATHAM) to simulate a synthetic SO₂ plume from passive degassing of an idealised volcano, loosely based on Villarrica. Built

within the Large Eddy Simulation framework, ATHAM was originally designed for simulating plinian eruption dynamics [Oberhuber et al., 1998, Herzog et al., 1998, 2003]. Within a volcanic context, it has been used for research into volcanic gas scavenging, particle aggregation and interactions with microphysics [Textor et al., 2006a,b], and more recently, into the dynamics of large co-ignimbrite [Herzog and Graf, 2010] and phreatomagmatic [Van Eaton et al., 2012] eruption clouds.

ATHAM is based on a modular structure that facilitates the coupling of specific process modules to the dynamical core. The core solves, within an Eulerian framework, the Navier-Stokes equations of momentum, and the pressure, temperature and tracer transport equations for a gas-particle mixture [Oberhuber et al., 1998]. Active tracers, i.e. solid, liquid or gaseous components that have their own heat capacities and densities, influence the mixture’s flow by changing its thermodynamic and dynamic properties. Momentum and tracer equations are described in flux form to guarantee conservation of momentum and mass; the heat transport equation is in advective form.

Short- and longwave radiative transfer, as well as surface fluxes of sensible and latent heat, have not been applied in our model runs, to reduce complexity and computational expense. Resolved and unresolved turbulent entrainment of ambient air into the plume modifies its buoyancy and disperses tracers and temperature anomalies. Subgrid-scale (SGS) turbulence is treated as eddy diffusivity and parametrised on the basis of a 1.5-order prognostic SGS anisotropic turbulent kinetic energy (TKE) closure scheme, described by Herzog et al. [2003]. The mixed-phase cloud microphysics included in the model correspond to a simple prognostic bulk Kessler-type approach, predicting cloud droplets, rain, ice crystals and graupel as specific concentrations [Herzog et al., 1998]. The current model configuration does not include aerosol microphysics and nucleation, cloud nuclei activation, or ash aggregation.

For our validation exercise, we used the same volcano model configuration as in the previously cited studies. The volcanic topography was parametrised as a simple Gaussian-shaped mountain with a height of 2850 m and a width parameter chosen such that the height-to-base ratio (500/2000) captured within our model domain roughly matched that of the Villarrica edifice. The crater was also chosen to be Gaussian-shaped (inverted), with a depth of 100 m, a width parameter of 50 m, and a flat bottom. Emissions from Villarrica typically emanate from large (5–20 m) vents in the cooled-crust covering the ~ 40 m-diameter lava lake that occupies the

base of its crater [Witter et al., 2004, Shinohara and Witter, 2005]. To emulate heat and volcanic gas fluxes from the lake, we applied a vertical velocity forcing over the cross-section of a lake, assumed to have a 50 m diameter. The baseline “exit” velocity was prescribed at 1 ms^{-1} , ramped up over 30 s, then modulated in time by a sine function of the same amplitude and a period of 2 min, mimicking periodicity in lake activity. Additionally, we superimposed random heterogeneity at each of the lake’s 25 grid-points of $\pm 50\%$ of the “exit” velocity. The potential temperature of the erupting gas-particle mixture above the lake was set to 1000 K, and specific gas and aerosol concentrations were aligned with the values measured by Sawyer et al. [2011]. From the tabled mass ratios of emitted gas species, we set the specific concentrations of the two gaseous tracers included in our model runs, magmatic H_2O and SO_2 , to 782 and 79 g kg^{-1} , respectively. From the ratio of the measured mass fluxes of SO_2 (3.7 kg s^{-1}) to aerosol (1 kg s^{-1}), we inferred a total aerosol active tracer specific concentration of 21 g kg^{-1} . The remainder was assumed to be dry air from unresolved near-surface turbulent entrainment. All particulate aerosol was assigned to a single size bin with a radius of $0.5 \mu\text{m}$ and in equal amounts of 7 g kg^{-1} to 3 size bins with radii of 0.1, 0.5 and $5 \mu\text{m}$ in a second simulation as described in Section 7.3. All aerosol was given a specific heat capacity of $1200 \text{ J kg}^{-1} \text{ K}^{-1}$ and a density of 2000 kg m^{-3} . Note that the actual values chosen to characterise volcanic degassing are not overly important, as the primary objective of the modelling exercise is to provide validation for motion estimation algorithms, rather than to constrain accurate plume dynamics and composition of a specific volcano. The turbulent length scale, and the horizontal and vertical TKE components over the lake were set to 2 m and $2 \text{ m}^2 \text{ s}^{-2}$, respectively.

To account for wind-driven advection, without incurring excessive computational expense, we opted for a two-dimensional Cartesian grid, acknowledging that this approach precludes three-dimensional turbulent entrainment and therefore limits effective plume dispersion. An equal and homogeneous grid-spacing of 2 m in both the horizontal and vertical dimensions was used, roughly matching the 1 m^2 pixel size of our Villarrica dataset (Section 7.2.4). We used 1010×751 grid-points to cover a domain 2018 m wide and 1500 m high, starting at an altitude of 2350 m. A no-slip condition was applied at the ground-level lower boundary, characterised by a roughness length of 10 cm; the lateral boundaries were open. The top boundary was treated as a rigid lid. Open boundaries defy mass conservation within the domain, requiring us to limit our simulations to 15 min. The minimum and maximum time steps were 0.01 and 1 s, respectively, governed by a Courant-Friederichs-Lewy cri-

terion limited to 0.8 for advection. Complete model data-fields were output every minute, and the full velocity, density and SO₂ fields were output roughly every second. Typical runtime on two computational cores was approximately one week.

Atmospheric initial conditions are specified in the model via a standard single vertical sounding profile of temperature, relative humidity and horizontal winds. These characterise atmospheric stability and determine potential advective transport. We used a sounding from Puerto Montt (station SCTE/85799, 41.43° S 73.10° W; ~250 km south of Villarrica) collected on 8 February 2012, at 12:00 UTC (-4 h time zone), which sets the simulation start to 08:00:00 LT (local time). Since the crater extends out of the atmospheric boundary layer and into the free troposphere, we estimate that the use of an early morning profile is inconsequential to the evolution of the plume. Only the west-east (u) component of the horizontal wind was retained. This was aligned with the model’s orientation, and scaled down to 20% of the measured values, in order to avoid excessively fast advection of the plume (and of turbulence) out of our small model domain, and strong up- and down-slope flow.

The model output was used to create a set of synthetic calibrated UV images, where pixel values represent column amounts of SO₂ in kg m⁻¹. The motion estimation algorithms were then applied to these images, and their performance evaluated by comparing the calculated SO₂ flux across a particular line of pixels to its real value (calculated using the motion field from the model output). The fluxes were calculated by integrating the product of the SO₂ column amounts across a transect of the image with the components of the velocity perpendicular to that transect.

Prior to applying the motion estimation algorithms, background and foreground regions (i.e. clear sky and the ground) were masked with Gaussian-distributed white noise, with a mean value approximating that of the pixels within the plume. This was found to greatly improve the performance of both algorithms, preventing spurious motion vectors from being computed in regions of very little texture and at high contrast boundaries.

7.2.4 Villarrica Dataset

A ~20 min sequence of UV images recorded at Villarrica volcano, Chile, on 8 February 2012 was used to test both algorithms’ performance on “real” data. The images were captured using an Apogee Alta U47-UV camera with an E2V CCD47-10,

1024×1024 pixel CCD and fitted with a 50 mm lens, giving a single pixel “footprint” of 1.02×1.02 m² (distance to the plume was ~4 km). The camera used a filter-wheel to alternate between in-band and out-of-band imaging, with an in-band image being recorded approximately every 4 s. Only the in-band images (310 nm) have been used in this study. We have not attempted to calibrate the images into SO₂ column amounts and the colour-scales on the images presented are in arbitrary units.

As in the case of the ATHAM data, random noise was used to mask background and foreground regions prior to motion estimation.

7.2.5 Image Registration

To demonstrate how motion estimation algorithms may be used to ensure an accurate mapping between pixels from different cameras (i.e. between the in-band and out-of-band images), we used a single UV camera image of Villarrica and applied a known distortion to it using OpenCV’s *cvWarpImage* function. As shown in Fig. 7.1, the distortion was made up of a perspective shift (the expected effect if the optical planes of the two cameras are not co-planar), and a rotation of 0.5° clockwise about the top left corner of the image. The two motion tracking algorithms were then used to calculate the shift vectors that mapped features in the distorted image to their respective positions in the original image.

In order to distribute errors in the shift estimates across the whole of the corrected image, we used the shift vectors to calculate a single corrective transform which we then applied to the whole image. In this case we assumed a projective distortion, and were therefore able to calculate the optimal (least-squares error) correction using OpenCV’s *cvFindHomography* function [described in detail by Bradski and Kaehler, 2008]. However, more complex corrections (e.g. including lens distortion) could be calculated in a similar manner using the correspondences found by the motion tracking algorithms.

To avoid errors caused by edge effects, we only included shifts from within a set region of interest (ROI) when calculating the corrective transformation. The ROI was selected so as to exclude the edges of the image, the crater region (which has very high intensity contrasts) and the clear sky regions (which have almost no intensity contrast) since motion estimates in these regions are often inaccurate. This selection procedure could potentially be automated by thresholding the image based

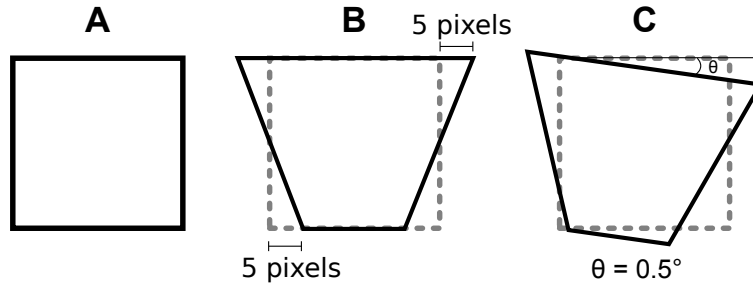


Figure 7.1: Cartoon of the distortion used to create a test image for the image registration technique. (A) The original (square) image, (B) perspective shift, (C) rotation (0.5° clockwise about top left corner).

on texture i.e. excluding regions where variation in pixel value is very small.

7.3 Results

Figure 7.2 shows the results of applying the motion estimation algorithms to the synthetic images produced using ATHAM. An animation showing the velocity fields produced for the full time series of images is provided in the supplementary material to the online version of this article. The SO_2 fluxes through a horizontal line of pixels 170 m above the crater, calculated using the velocities from ATHAM and the two motion estimation algorithms, are plotted against time. As shown in Fig. 7.3, the agreement of the estimated fluxes with the fluxes computed from ATHAM is striking and provides a strong argument for the use of these algorithms in computing plume transport speeds. Both the DT-CWT and Farneback methods show a good correlation across the full range of flux values, with R^2 values of 0.95 and 0.97 respectively.

The model used to produce the images for Fig. 7.2 had a closed top (rigid lid) boundary (as described in Section 7.2.3), acting essentially in a similar way as a very strong temperature inversion layer. When the buoyant plume reached the top boundary of the domain, it was forced to spread laterally and large down-welling regions quickly led to a negative flux across the integration line (as can be seen beyond 08:04:31 in Fig. 7.2). To overcome this issue, an additional 49 vertical grid-points were added, extending the vertical model domain to a total elevation of more than 6 km on a stretched grid. In addition, we increased vertical wind shear by applying a linear multiplier function to the wind profile, varying between 1 and 1.5 over the lower 1.5 km vertical extent of the model domain. Furthermore, we applied $\pm 20\%$ random white noise onto the initial horizontally homogeneous wind field, and initialised the

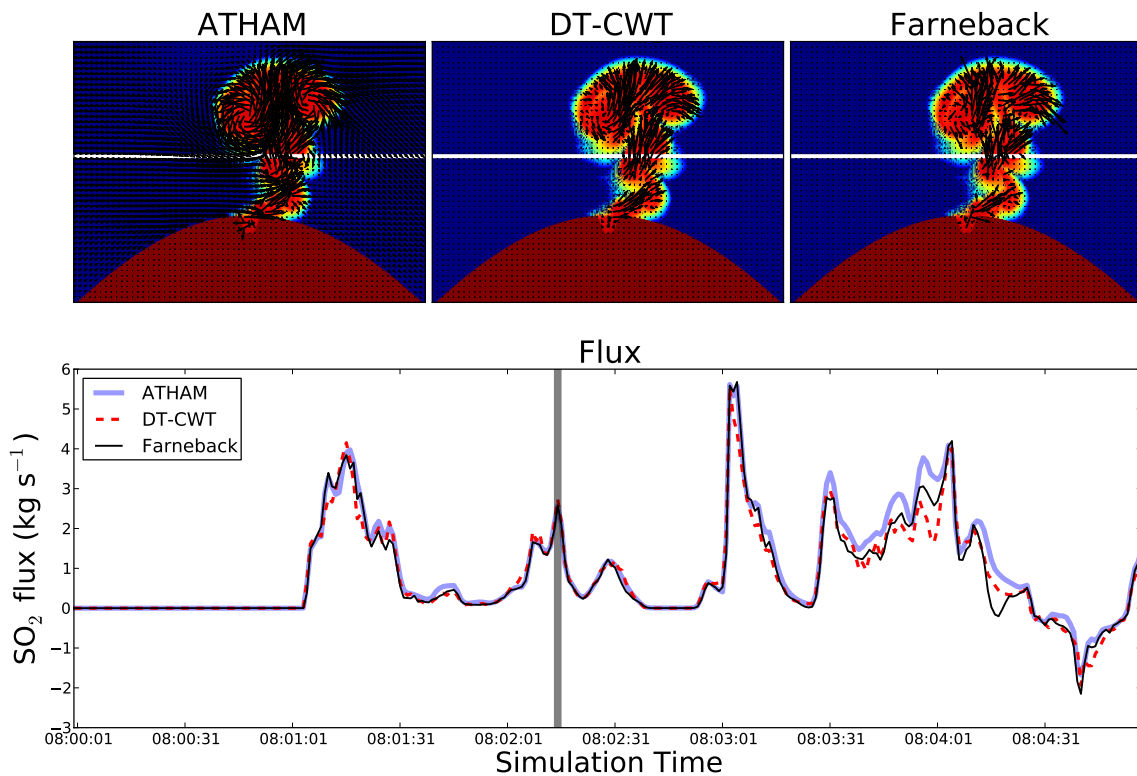


Figure 7.2: Summary of results from the “closed-top” ATHAM simulation. SO_2 fluxes calculated using the velocity fields from ATHAM, the DT-CWT algorithm, and the Farneback algorithm are plotted against time. Snapshots of the velocity fields (corresponding to the time denoted by the vertical grey line) superimposed over the SO_2 amounts are also shown. The line of pixels over which the fluxes were calculated is highlighted in white.

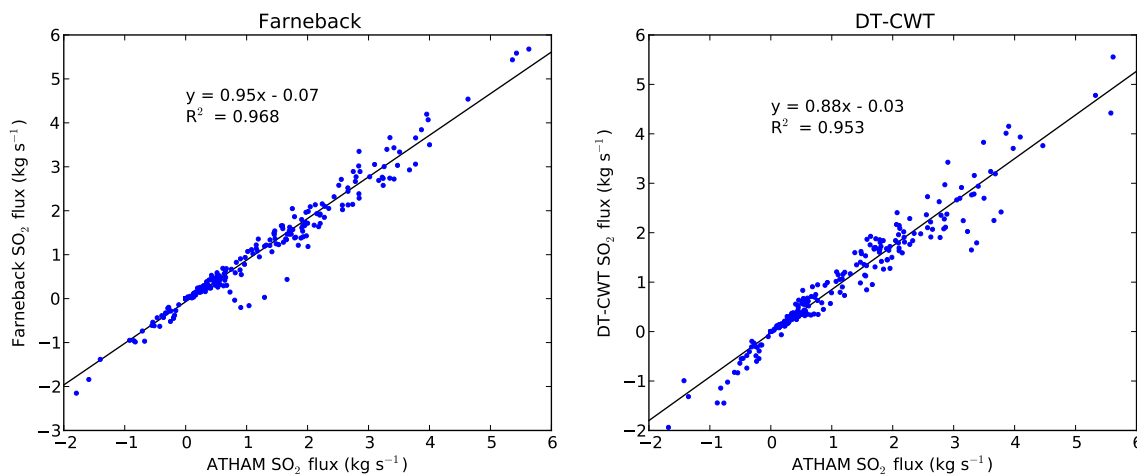


Figure 7.3: Scatter plots showing the relationship between the SO_2 fluxes computed using velocity estimates from the Farneback (left) and DT-CWT (right) algorithms and the real fluxes from the “closed-top” ATHAM model. A linear regression line and the associated R^2 value are also shown.

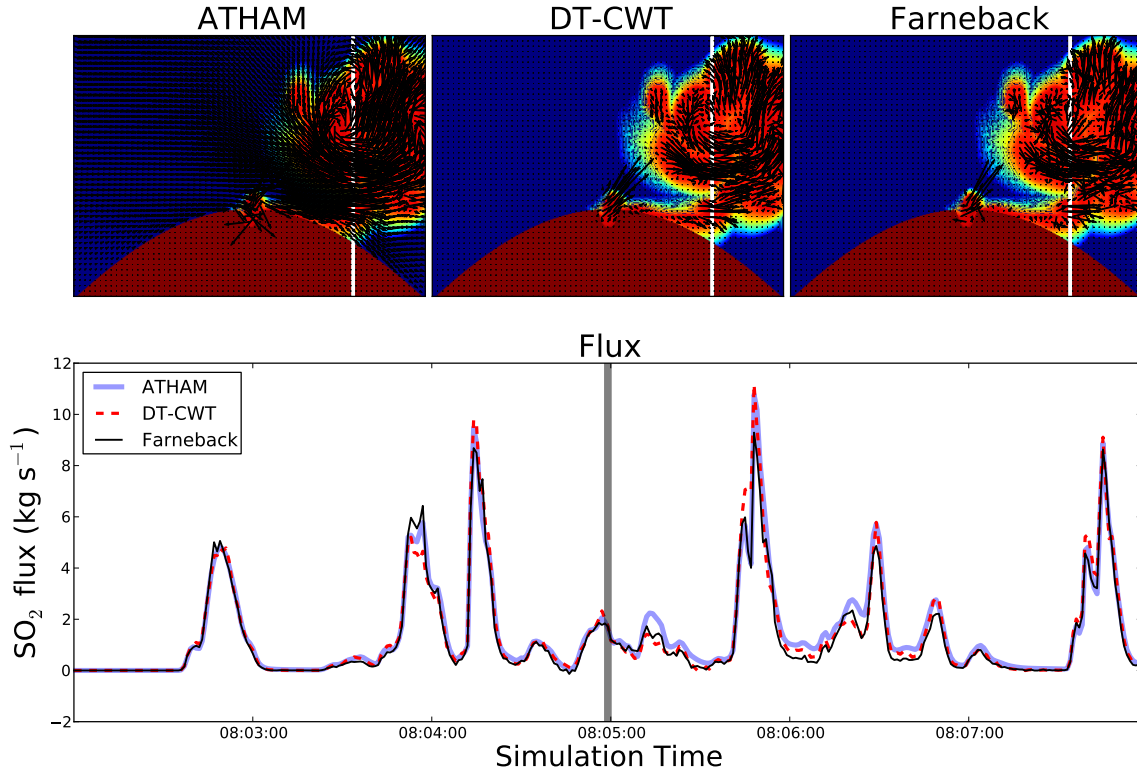


Figure 7.4: Summary of results from the “open-top” ATHAM simulation. SO_2 fluxes calculated using the velocity fields from ATHAM, the DT-CWT algorithm, and the Farneback algorithm are plotted against time. Snapshots of the velocity fields (corresponding to the time denoted by the vertical grey line) superimposed over the SO_2 amounts are also shown. The line of pixels over which the fluxes were calculated is highlighted in white.

SGS TKE with isotropic turbulence on the order of $1 \text{ m}^2 \text{ s}^{-2}$, to promote resolved turbulent effects. However, the increased randomisation of the initial conditions did not produce a significant effect. The motion of the plume produced by this setup was predominantly horizontal (and often grounded in the vicinity of the crater), necessitating a vertical integration line. The results from this simulation are shown in Fig. 7.4. Note however, that the extended vertical extent of the model domain has been cropped from the plotted data such that the plotted extent matches that of Fig. 7.2. Once again, the effectiveness of the motion estimation algorithms is clearly demonstrated (Fig. 7.5). As shown in the animated sequence (see supplementary materials), the periods in which the motion estimation algorithms significantly underestimate the SO_2 flux (e.g. 08:06) correspond to periods when large portions of the plume are grounded at the integration line and lack any significant structure.

Using the same images as for Figs. 7.2 and 7.4, we made flux estimates using the conventional cross-correlation technique often used in UV imaging [Kantzas et al.,

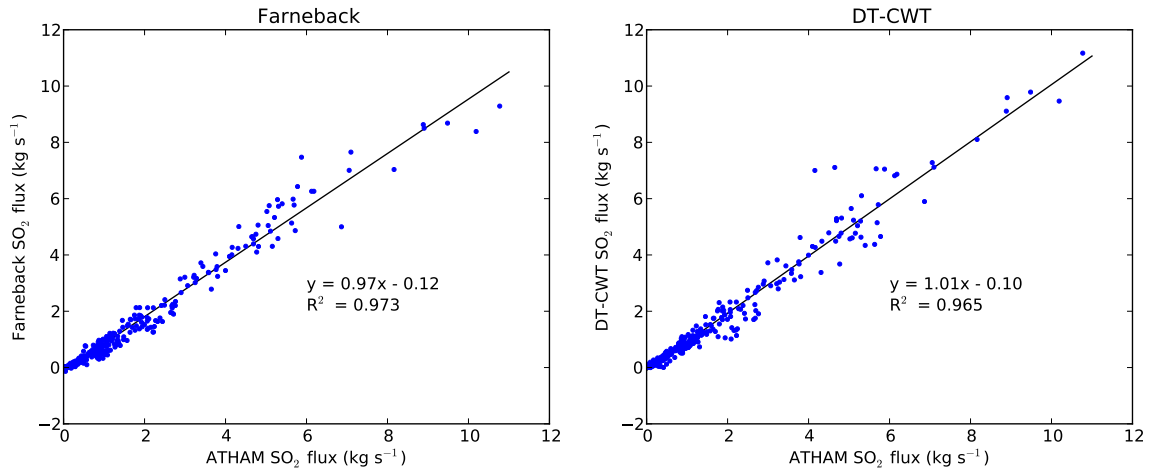


Figure 7.5: Scatter plots showing the relationship between the SO_2 fluxes computed using velocity estimates from the Farneback (left) and DT-CWT (right) algorithms and the real fluxes from the “open-top” ATHAM model. A linear regression line and the associated R^2 value are also shown.

2010]. The integrated SO_2 column amounts for the cross-correlation were taken from 20 m either side of the integration lines used in Figs. 7.2 and 7.4. The correlation window used spanned 20 s. Short time series of the resulting fluxes are shown in Figs. 7.6 and 7.7. Figure 7.6 shows a period when the cross-correlation method performs well, and Fig. 7.7 shows a period when it does not. Fluxes calculated using velocity estimates from the Farneback algorithm are also shown for comparison. It can be seen that although the cross-correlation method produces reasonable flux estimates when the plume consists of discrete puffs (Fig. 7.6), when the plume is less structured it can produce errors of up to 300 % (Fig. 7.7). The Farneback algorithm performs consistently better than the cross-correlation method, and appears to be less sensitive to plume conditions.

As already discussed, it is not possible to quantitatively assess the performance of motion estimation algorithms on real UV images. However, some insight can be gained through a visual inspection of the motion vectors produced by the algorithms. Figure 7.8 shows a snapshot of the motion vectors calculated by both the DT-CWT and Farneback algorithms when applied to a sequence of UV images of Villarrica (see Section 7.2.4). Animations of the motion estimates from the full sequence of images are provided in the supplementary material to the online version of this article. As shown by the histograms in Fig. 7.8, both algorithms produce a similar distribution of velocity vectors over the plume region. In general the DT-CWT technique produces a smoother velocity field. However, this is possibly due to our choice of algorithm parameters rather than the algorithm itself and, as discussed

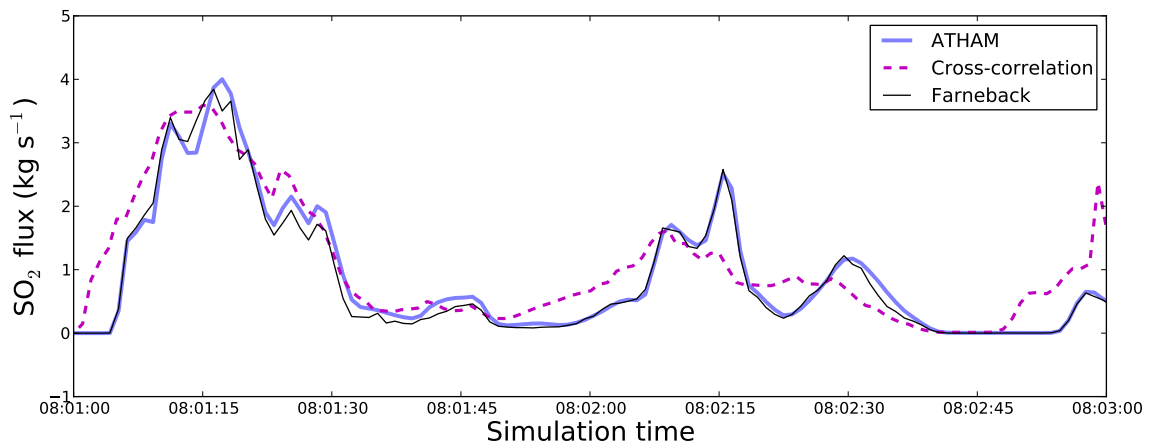


Figure 7.6: Short time series comparing SO_2 fluxes calculated from synthetic images from the “closed-top” ATHAM simulation using a simple cross-correlation method and the Farneback algorithm. The true fluxes (calculated using the ATHAM velocity field) are also shown. This time period was chosen deliberately as an example of good performance of the cross-correlation technique.

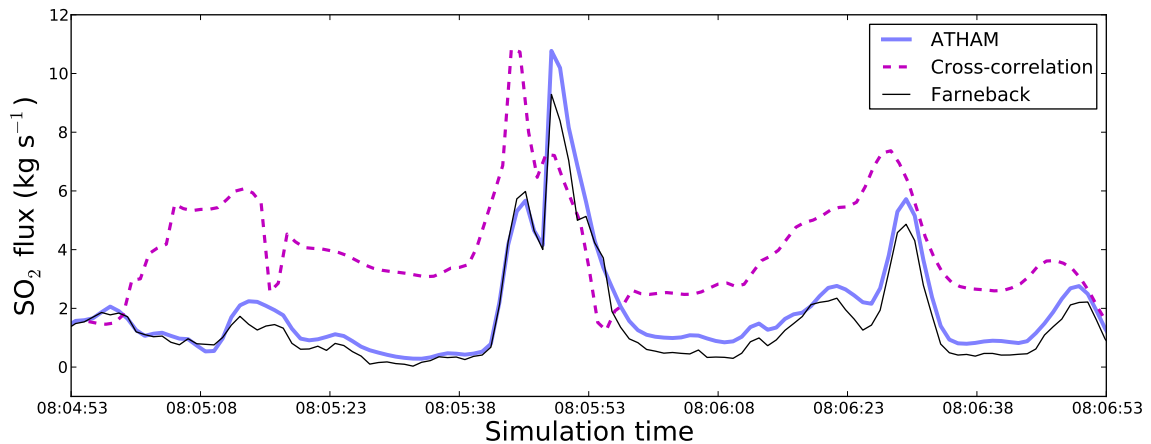


Figure 7.7: Short time series comparing SO_2 fluxes calculated from synthetic images from the “open-top” ATHAM simulation using a simple cross-correlation method and the Farneback algorithm. The true fluxes (calculated using the ATHAM velocity field) are also shown. This time period was chosen deliberately as an example of poor performance of the cross-correlation technique.

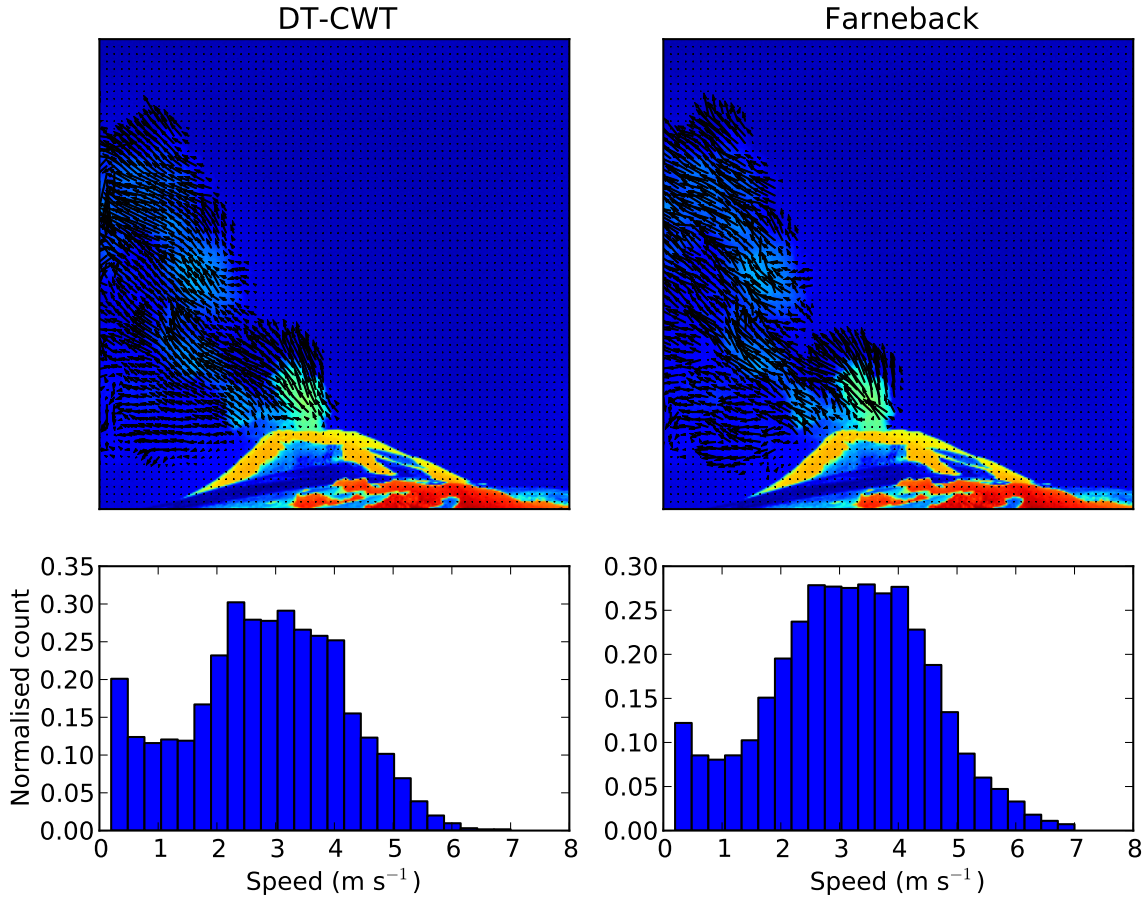


Figure 7.8: A UV image of Villarrica captured on 8 February 2012, with motion vectors estimated using the DT-CWT algorithm (left image) and the Farneback algorithm (right image). Normalised histograms showing the distribution of magnitudes of the velocity vectors produced by each method are also plotted. Motion vectors from the outside 10 pixels of the image have been excluded from the histograms, as have the zero velocity vectors.

in Section 7.2.1, a more rigorous methodology for selecting parameter values would be needed to enable direct comparison of the methods. Both algorithms produce a mean plume velocity of around 3.5 m s^{-1} , which seems plausible for Villarrica. Closer inspection of the estimated motion shows, as demonstrated by Fig. 7.9, that the magnitudes and directions of the velocity vectors from both algorithms match the motion of easily observable features.

The results of using the DT-CWT and Farneback algorithms to calculate the corrective transform for a distorted image (as described in Section 7.2.5) are shown in Fig. 7.10. To assess the performance of the registration we have plotted the percentage error of each pixel value in the corrected image with respect to its value in the original image, i.e. the error associated with the pixel at coordinates (i, j) , $E_{i,j}$, is

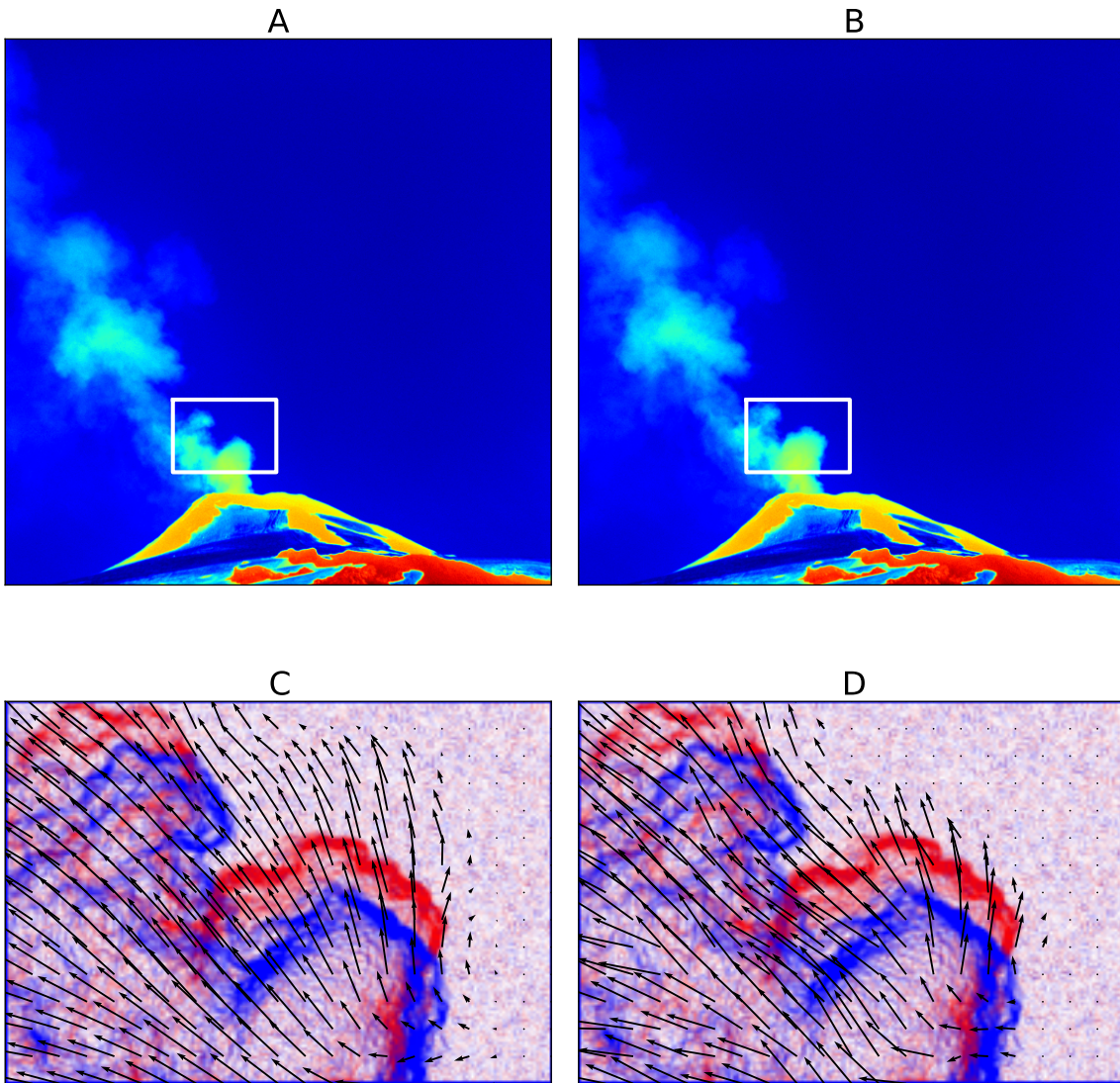


Figure 7.9: (A, B) Two successive UV images of Villarrica with a ~ 4 s delay between them, the region displayed in C and D is denoted by the white rectangles. (C, D) Motion vectors mapping pixels in A to their corresponding positions in B; computed using the DT-CWT algorithm (C) and the Farnebäck algorithm (D). Notable features in the plume from image A (blue) and B (red) have been enhanced using Sobel edge detection and are displayed. Correct motion vectors are expected to point from features shown in blue to the corresponding feature in red.

given by:

$$E_{i,j} = \frac{|O_{i,j} - C_{i,j}|}{O_{i,j}} \times 100 \quad (7.1)$$

where $O_{i,j}$ is the pixel value in the original image, and $C_{i,j}$ is its value in the corrected image.

The correction to the image was applied using OpenCV's *cvWarpImage* function (as was the original distortion). It should be noted that distortion and subsequent correction, even when the transformation is known exactly, leads to errors of 30–40% in the out-of-plume region of the corrected image (where the pixel values are close to zero). This is due to the interpolation required when performing the transformations. The striped pattern observed in the error plots is caused by a small-amplitude periodic fluctuation in the intensities of pixels in the original image, and is not an artifact of the registration technique. We are unclear on the exact origin of this phenomenon but suggest that it may be caused by an instrumental effect due to the particular hardware configuration of the camera. As can be seen in Fig. 7.10, both algorithms produce similar results, with resultant errors being within the interpolation error of the *cvWarpImage* function. In the plume region, the errors in the corrected images are <3% for both algorithms.

7.4 Discussion

In general both algorithms performed similarly, with equal resultant errors when used for image registration, and comparable correlations with real flux values when applied to our synthetic data (Figs. 7.3 and 7.5). However, we found the Farnebäck algorithm to be less sensitive to input parameters, and therefore a little easier to use than the DT-CWT algorithm. As previously mentioned, a wide range of motion estimation algorithms exist and it is not our intent to promote the DT-CWT or Farnebäck algorithms in particular as being superior for use with UV camera images. That said, the results produced by both when applied to the Villarrica and ATHAM datasets were encouraging, and suggest that, even if not optimal, either algorithm would be a reasonable choice for this application.

More specialised optical-flow algorithms exist, which are specifically designed for tracking fluid flows. As such, they incorporate constraints from fluid mechanics, such as continuity, to prevent un-physical flow estimations. The findings of Corpetti

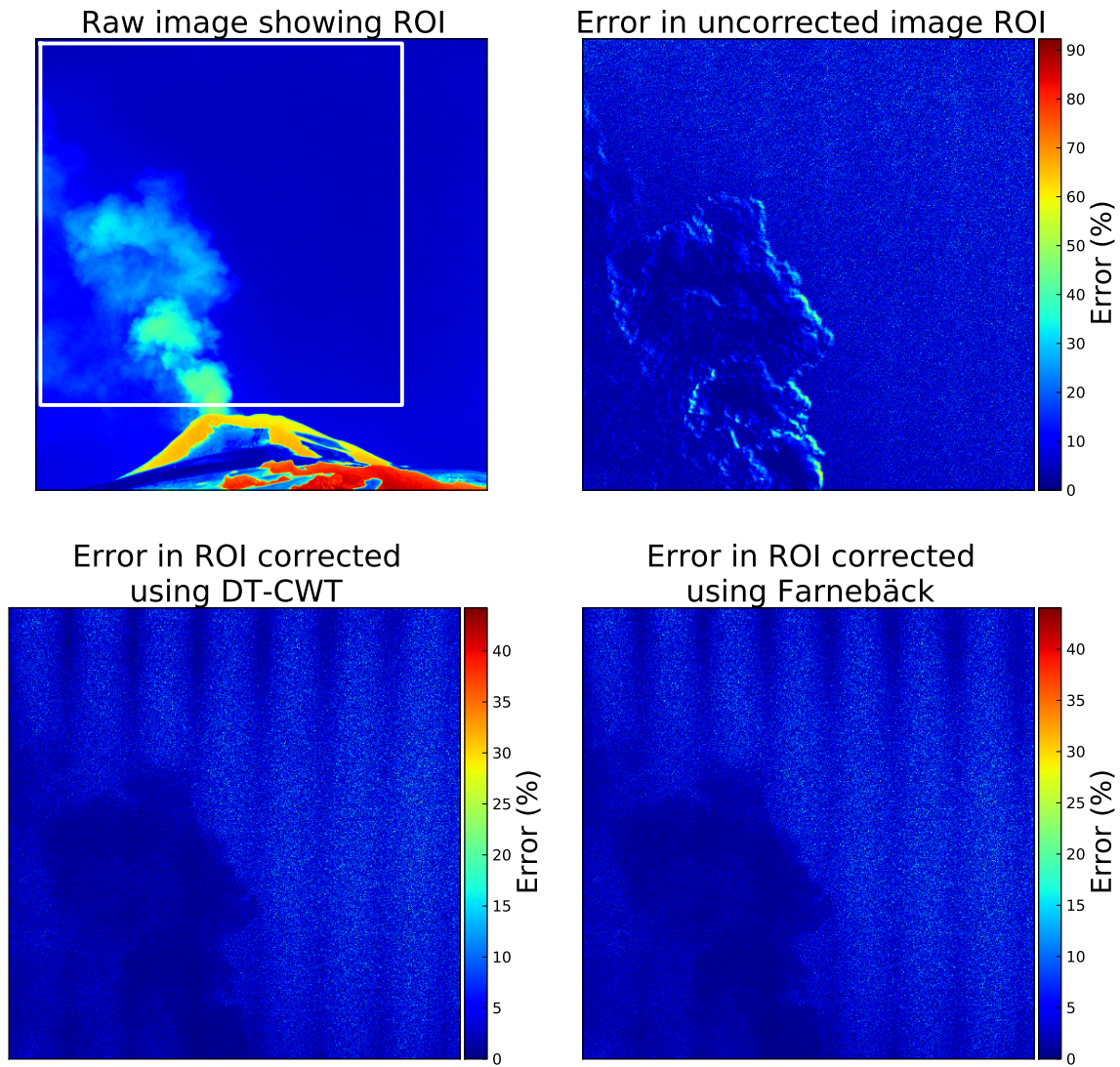


Figure 7.10: Results of using the DT-CWT and Farneback algorithms to estimate a projective distortion to an image. Top left: the original, undistorted image with the region of interest (ROI) over which motion vectors were estimated highlighted. Top right: percentage pixel errors in the ROI of the distorted image. Lower left: percentage pixel errors in the ROI of the image corrected using the DT-CWT algorithm. Lower right: percentage pixel errors in the ROI of the image corrected using the Farneback algorithm.

et al. [2002] show that inclusion of these constraints can lead to improved accuracy of the motion estimates produced for fluid flows. Such algorithms may be more suitable for estimating the plume transport speed than the DT-CWT or Farnebäck algorithms. However, successful application of the continuity constraint relies on accurate knowledge of the SO₂ amounts in each pixel. Whilst this is the case for the synthetic images produced by ATHAM, the calibration of real images is more questionable and it is not clear how these errors might propagate into the motion estimate. In the future it may be possible to combine the motion estimates and the apparent absorbance data into a single coherent plume model which could then be inverted for SO₂ flux, minimising the errors from both the motion and the calibration. However, this is pure speculation, and is beyond the scope of this investigation.

Synthetic plume images, such as those created using ATHAM, are clearly a useful validation tool for SO₂ flux calculation techniques. However, the extent to which they are representative of images of a real plume is questionable. In short, it is not necessarily true that a motion estimation algorithm that can perfectly reproduce the velocity field of the synthetic images will work well when applied to real data. However, it seems fair to say that the synthetic images provide a useful starting point for algorithm development and tuning.

The configuration and setup of the model used in this study was limited by computing time, and it is likely that with more resources its capabilities could be exploited to a greater extent. In particular, our simulations fail to reproduce the very rapid dilution of the plume that is seen in the Villarrica images. This may be due in part to the fact that the model is run only in two-dimensions, greatly reducing the scope for entrainment of the surrounding atmosphere into the plume. A three-dimensional setup using ATHAM, whilst possible, would be very computationally expensive. It would, however, facilitate very useful studies into the effects of treating a real volcanic plume as a two-dimensional object when calculating transport speeds. It is important to remember that each pixel in a UV image represents an integrated amount of SO₂ in the plume along the optical path of that pixel. Hence, estimating motion vectors from such an image can only ever yield a coarse approximation to the true plume velocity. Three-dimensional plume model data would allow the errors introduced by estimating transport speeds from a two-dimensional projection of the plume to be investigated.

Although both algorithms were able to accurately compute the transformation re-

quired to correct our distorted image, in reality the problem is more complex. The image pairs to be registered from UV camera systems employing two camera units are captured at different wavebands and features visible in the in-band image may not be present in the out-of-band image. This will likely degrade the performance of the algorithms and may compromise their ability to compute the motion vectors altogether. The extent of this problem will depend on the composition of the specific plume being imaged, and could be alleviated by careful selection of regions of the images over which to perform the motion estimation. An alternative, and possibly superior approach, would be to periodically capture a set of images at the same waveband from both cameras and use these to compute the registration parameters required.

It is theoretically possible to use the motion estimation techniques to correct for more complex image distortions than the projective transformation which we demonstrated (e.g. radial lens distortions). However, allowing more degrees of freedom when calculating the corrective transformation will lead to a less robust result, which is more susceptible to errors in the motion estimates. Since the lens distortion should be relatively constant, we believe that this correction would be better calculated prior to field deployment of the camera, perhaps using the well-established “chess board” technique [described in detail by Bradski and Kaehler, 2008].

7.5 Conclusions

We have presented two different motion estimation algorithms, a DT-CWT based algorithm and the Farneback algorithm, and showed how they can be applied to UV camera images to improve the calculation of SO₂ flux. The ATHAM model was used to create a set of synthetic UV images for which the SO₂ amounts and velocity field were known, and these were used to validate the estimates produced by the two algorithms.

Motion estimation algorithms are clearly a useful tool when applied to SO₂ measurements using UV cameras. It has been found in this study that they can provide a means to accurately register images from two separate camera units, in addition to providing more robust estimates of plume velocity for use in flux calculations than the currently-used cross-correlation method. The two algorithms presented here were similar in performance and would both be suitable for UV camera appli-

cations, however, we found the Farneback algorithm a little easier to use. A more thorough comparison of different algorithms is needed to determine the optimal algorithm for UV camera applications and this will require a more rigorous approach to input parameter selection than was used in this study.

Using plume models, such as ATHAM, to produce test datasets for motion estimation algorithms provides a simple way to evaluate and compare their performance. Further research is required to ensure that the data produced are an accurate representation of real volcanic plumes, and extension of the model setup into three-dimensions promises to provide valuable insights into the errors associated with flux measurements.

Chapter 8

Conclusions

“Well if everything else wasn’t broken, we’d be sorted.”

– Bill McIntosh, Erebus, December 2010.

I have developed new volcanic monitoring technologies and techniques and also analysed the results of applying these to the Erebus lava lake. A new thermal camera system was created and deployed at the crater rim of Erebus and new hardware and software for recording SO₂ fluxes was also developed. Additionally, a new methodology for estimating plume transport velocity from UV camera images was investigated. Overall, IR images of the Erebus lava lake from 2004 up to 2013 have been analysed to obtain the mean speed of the lake surface. The most recent IR images were collected at concurrently with measurements of SO₂ flux, gas composition and surface elevation of the lake allowing, for the first time, a detailed inter-comparison of the cyclic behaviour observed in each. The conclusions from these studies are summarised below, organised in terms of the research objectives which were laid out in Section 1.7.

8.1 Improved Monitoring

The new thermal camera system developed as part of this study and deployed on Erebus in December 2012 (Chapter 2) is a great success. Despite the failure of the power system during the winter months, the dataset collected surpasses any previously collected, both in terms of length and continuity. The camera has not only greatly enhanced the monitoring capacity of the Mount Erebus Volcano Observatory, but has also provided a valuable pilot project to test the feasibility of running instruments at the crater rim outside of the short time window of the annual field campaigns. Future instruments are already under consideration and plans are currently being made to install year-round telemetry to the crater rim during the 2014 field season, allowing “live” imagery of the lake to be collected. As well as the camera system itself, the infrastructure that was installed to support it (power, Ethernet) has been hugely beneficial to the field campaigns in general. Data loss due to power and network failures is now largely a thing of the past, and time-series data continues to improve in terms of continuity, facilitating ever more detailed analyses.

High temporal resolution measurements of SO₂ flux from volcanoes are challenging to achieve for a variety of reasons. A major contribution to the problem is the difficulty of accurately measuring of plume transport velocity. I have demonstrated that using the motion tracking methodologies used during the IR image analysis part of this study, more accurate estimates of plume transport velocity can be obtained than is possible with the currently-used cross-correlation method. These findings will not only be useful for future studies at Erebus, but also for researchers and

volcano observatories around the world who use UV cameras for making SO₂ flux measurements.

8.2 Assessment of Annual Variability of the Lava Lake Cycles

Pulsatory behaviour in the mean surface speed of the lake has been sustained since at least 2004, when the first measurements were made. Cycles, with a period of 5–18 min, are always present although with varying degrees of visibility in the data. Despite significant changes in the visible size of the lake, no change in the cyclic behaviour was detectable across the period studied (2004–2013). This would suggest not only that the cyclic behaviour is a long-term stable feature, but also that the mechanism responsible occurs at a greater depth than the lake itself.

Large (decametric) bubbles are too infrequent to be considered as a possible driving mechanism for the pulsatory behaviour and the timings of smaller bubbles are found to be uncorrelated with the phase of the cycles in surface speed. These findings point towards a driving mechanism based on the flow dynamics of magma exchange within the shallow magmatic system and largely rule out gas-driven mechanisms.

8.3 Multi-parameter Observations of Cyclic Behaviour

In addition to the cyclic behaviour in the mean surface speed, similar behaviour is found in the SO₂ flux, plume composition and surface elevation of the lake. The cycles in each of these parameters are well correlated with each other, suggesting that they all derive from a common underlying process. It can be shown by considering the magma flux required to explain the mass of H₂O released per cycle, that the observed variations in surface elevation of the lake can be accounted for by exchange of magma in and out of the lake. This supports the hypothesis that the pulsatory behaviour of the Erebus lake is driven by magma exchange rather than gas flux. Furthermore, it suggests that the lake is highly permeable to gas, and does not present a significant barrier to its escape. However, this is somewhat contradicted by the finding that the peak in surface motion and gas composition lag the peak

in surface elevation by 1–3 min. This may be explained by the time taken for fresh magma injected into the lake to rise to the surface, suggesting that the gas rises with the melt through the lake.

The behaviour of the lake following explosive events caused by large bubble bursts is indistinguishable from its behaviour prior to the events, with the exception of the ~ 5 min required for the lake to refill. No change in amplitude or period of the pulsatory behaviour is observed, suggesting a high degree of decoupling between the explosive and passive degassing mechanisms of the system.

8.4 The Future

This study has done much to progress our understanding of the Erebus lava lake; identifying cycles in the surface elevation, surface motion, SO_2 flux and gas chemistry as a persistent and stable feature of its behaviour, which is decoupled from the explosive activity. However, there are clearly a lot of questions left unanswered. In particular, the exact mechanism responsible for the pulsatory behaviour remains elusive. Whilst the observations presented here have provided some insight into feasible mechanisms, it is simply not possible to test these hypotheses further based on observations alone. It is our belief that the next breakthroughs in understanding the Erebus magmatic system will come from combining the observations presented here with lab-based flow models and computer simulations. This will allow the exact conditions required to reproduce the observed behaviour to be deduced. The work presented here has brought us several steps closer to understanding Erebus, but it is a long road and the end is not yet in sight.

Acknowledgements

None of this would have been possible without the help and support of a huge number of people. First and foremost, I thank my supervisor Clive Oppenheimer. This PhD has played out almost exactly as I had hoped, and I owe that to you. Aaron Curtis, thanks for getting me into this mess in the first place and I really hope we manage to continue to find excuses to go into the field together. Phil Kyle, I'm still suspicious that the only reason you ever took me to Erebus was because you were embarrassed about nearly burning Clive's house down. But whatever the reason, thank you! Vitchko Tsanev, Talfan Barnie, Amy Donovan, Lex Hoffmann and Nick Kingsbury, it has been a great pleasure to work with you all. I would also like to thank my parents for their continued support and encouragement. A huge and deeply heartfelt thanks to Andrew and Bela, my wonderful house-mates, and to all the rest of the inhabitants and associates of the Long Road commune. Cycle-cake Sundays, box-of-wine Wednesdays, slugs and electric taps; it really is a "special" place to live and I hope we can keep it going for a bit longer at least. Last but not least, I must thank The Volcanofiles (Kelby Hicks, Tehnuka Ilanko, Kayla Iacovino, Yves Moussallam). It has certainly been a rough road guys, but the good times were some of the best in my life, and it is those that I will remember. Kelby, your passion and enthusiasm was truly inspirational; we all miss you dearly.



The Volcanofiles at Villarrica, Chile, 2012. Photo: Kayla Iacovino.

Appendix A

Data Availability

This appendix contains charts showing when thermal images of the Erebus lava lake have been recorded. Images from both the P25 and the newer SC645 camera (see Table 4.1) are included. It will be seen that the data are far from continuous, even with the new camera system [Chapter 2, Peters et al., 2014c]. However, many of the gaps in the the data are caused by a build-up of rime-ice on the lens of the camera, obscuring its view of the lake entirely.

It should be noted that the time-spans of the data included here have not been “cleaned” of unusable images (i.e. those in which the lake is not clearly visible). Therefore, even if images are available for a particular time period, it may not be possible to obtain useful results from them.

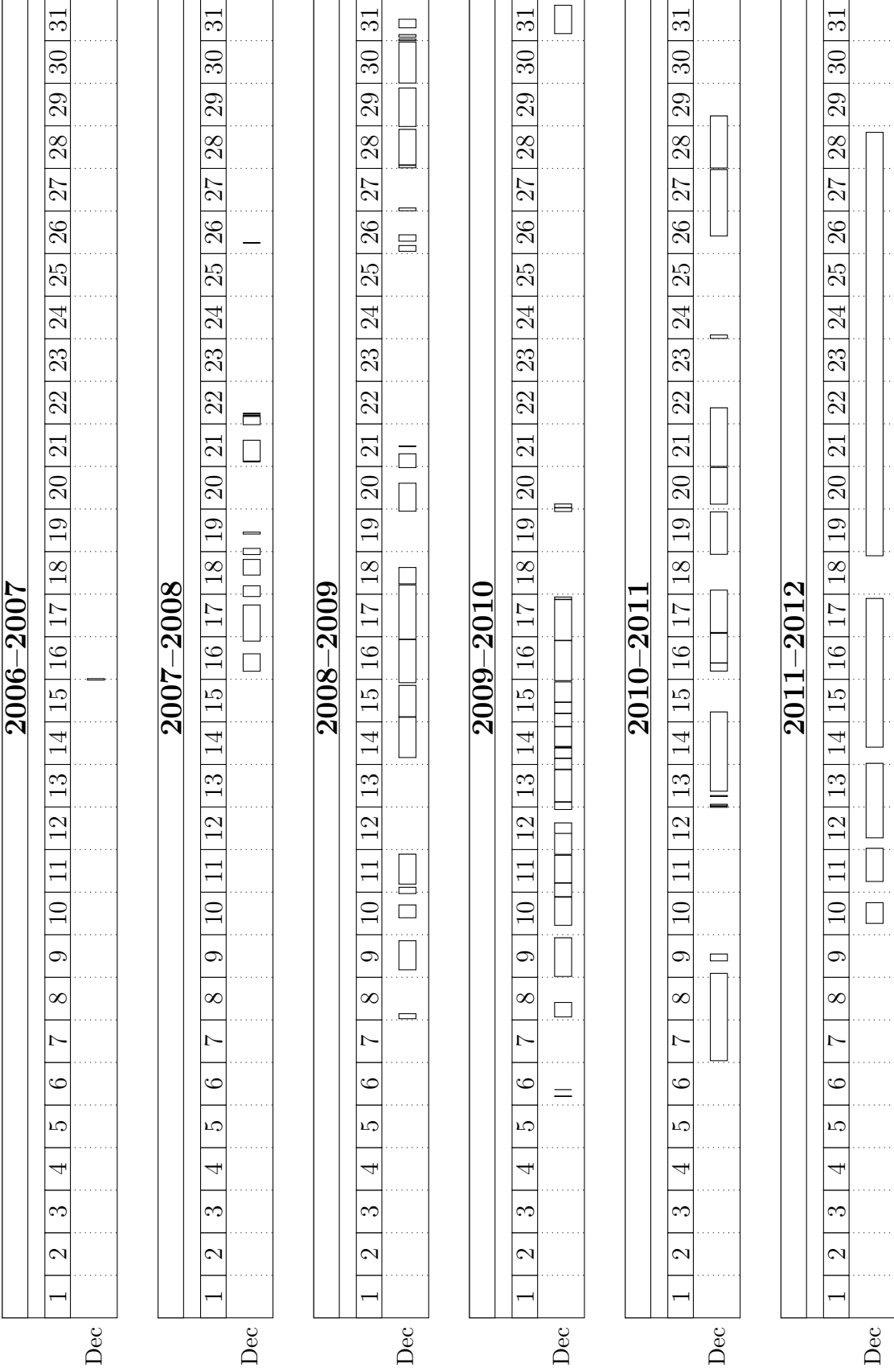


Figure A.1: Data availability for the P25 thermal camera.

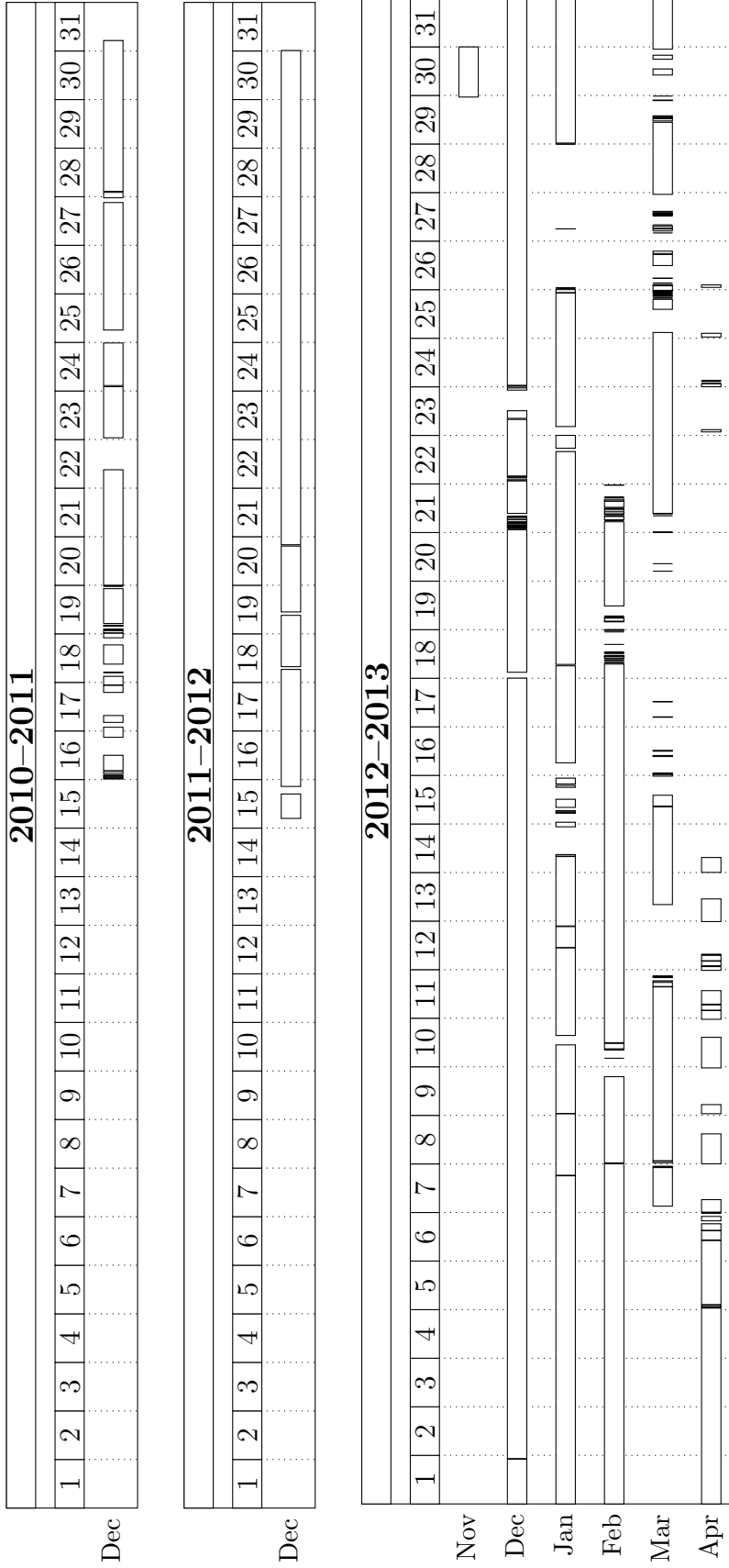


Figure A.2: Data availability for the SC645 thermal camera.

Bibliography

- A. Aiuppa, C. Federico, G. Giudice, and S. Gurrieri. Chemical mapping of a fumarolic field: La Fossa Crater, Vulcano Island (Aeolian Islands, Italy). *Geophysical Research Letters*, 32(13), 2005. ISSN 1944-8007. doi: 10.1029/2005GL023207.
- Apache. Apache OpenOffice Calc, 2013. URL <http://www.openoffice.org/product/calc.html>.
- R. Aster, S. Mah, P. Kyle, W. McIntosh, N. Dunbar, J. Johnson, M. Ruiz, and S. McNamara. Very long period oscillations of Mount Erebus volcano. *Journal of Geophysical Research*, 108:22 PP., Nov. 2003. doi: 200310.1029/2002JB002101.
- R. Aster, W. McIntosh, P. Kyle, R. Esser, B. A. Bartel, N. Dunbar, B. Johns, J. B. Johnson, R. Karstens, C. Kurnik, M. McGowan, S. McNamara, C. Meertens, B. Pauley, M. Richmond, and M. Ruiz. Real-time data received from Mount Erebus volcano, Antarctica. *Eos*, 85(10):97–104, Mar. 2004. doi: 200410.1029/2004EO100001.
- S. J.-B. Bauguitte, N. Brough, M. M. Frey, A. E. Jones, D. J. Maxfield, H. K. Roscoe, M. C. Rose, and E. W. Wolff. A network of autonomous surface ozone monitors in Antarctica: technical description and first results. *Atmospheric Measurement Techniques*, 4(4):645–658, Apr. 2011. ISSN 1867-8548. doi: 10.5194/amt-4-645-2011.
- G. Bluth, J. Shannon, I. Watson, A. Prata, and V. Realmuto. Development of an ultra-violet digital camera for volcanic SO₂ imaging. *Journal of Volcanology and Geothermal Research*, 161(1–2):47–56, Mar. 2007. ISSN 0377-0273. doi: 10.1016/j.jvolgeores.2006.11.004.
- M. L. Boas. Error Propagation Equation. In *Mathematical Methods in the Physical Sciences*, pages 734–735. Wiley, 2nd edition, Apr. 1983a. ISBN 0471044091.
- M. L. Boas. *Mathematical Methods in the Physical Sciences*. Wiley, 2nd edition, Apr. 1983b. ISBN 0471044091.

- M. Boichu, C. Oppenheimer, V. Tsanev, and P. R. Kyle. High temporal resolution SO₂ flux measurements at Erebus volcano, Antarctica. *Journal of Volcanology and Geothermal Research*, 190(3-4):325–336, 2010. ISSN 0377-0273. doi: 10.1016/j.jvolgeores.2009.11.020.
- E. Bouche, S. Vergnolle, T. Staudacher, A. Nercessian, J.-C. Delmont, M. Frogneux, F. Cartault, and A. Le Pichon. The role of large bubbles detected from acoustic measurements on the dynamics of Erta 'Ale lava lake (Ethiopia). *Earth and Planetary Science Letters*, 295(1–2):37–48, June 2010. ISSN 0012-821X. doi: 10.1016/j.epsl.2010.03.020.
- G. Bradski. The OpenCV Library. *Dr. Dobb's Journal of Software Tools*, 25(11): 120, 122–125, Nov. 2000. ISSN 1044-789X.
- G. Bradski and A. Kaehler. *Learning OpenCV: Computer Vision with the OpenCV Library*. O'Reilly Media, 1st edition, Sept. 2008. ISBN 0596516134.
- A. Burgisser, C. Oppenheimer, M. Alletti, P. R. Kyle, B. Scaillet, and M. R. Carroll. Backward tracking of gas chemistry measurements at Erebus volcano. *Geochemistry, Geophysics, Geosystems*, 13(11), 2012. ISSN 1525-2027. doi: 10.1029/2012GC004243.
- J. Burrows, A. Richter, A. Dehn, B. Deters, S. Himmelmann, S. Voigt, and J. Orphal. Atmospheric Remote-Sensing Reference Data from GOME: 2. Temperature-Dependent Absorption Cross Sections of O₃ in the 231-794 nm Range. *Journal of Quantitative Spectroscopy and Radiative Transfer*, 61(4):509–517, Mar. 1999. ISSN 0022-4073. doi: 10.1016/S0022-4073(98)00037-5.
- M. R. Burton, C. Oppenheimer, L. A. Horrocks, and P. W. Francis. Remote sensing of CO₂ and H₂O emission rates from Masaya volcano, Nicaragua. *Geology*, 28(10):915, 2000. ISSN 0091-7613. doi: 10.1130/0091-7613(2000)28<915:RSOAH>2.0.CO;2.
- J. Calkins, C. Oppenheimer, and P. Kyle. Ground-based thermal imaging of lava lakes at Erebus volcano, Antarctica. *Journal of Volcanology and Geothermal Research*, 177(3):695–704, 2008. ISSN 0377-0273. doi: DOI:10.1016/j.jvolgeores.2008.02.002. Volcanology of Erebus volcano, Antarctica.
- R. Champion, M. Martinez-Cruz, T. Lecocq, C. Caudron, J. Pacheco, G. Pinardi, C. Hermans, S. Carn, and A. Bernard. Space- and ground-based measurements of sulphur dioxide emissions from Turrialba Volcano (Costa Rica). *Bulletin of*

- Volcanology*, 74(7):1757–1770, June 2012. ISSN 0258-8900, 1432-0819. doi: 10.1007/s00445-012-0631-z.
- M. Cassidy, P. D. Cole, K. Hicks, N. Varley, N. Peters, and A. Lerner. Rapid and slow: Varying magma ascent rates provide the mechanism for small Vulcanian eruptions. *Earth and Planetary Science Letters (in review)*, 2014.
- K. Chance and R. Kurucz. An improved high-resolution solar reference spectrum for earth’s atmosphere measurements in the ultraviolet, visible, and near infrared. *Journal of Quantitative Spectroscopy and Radiative Transfer*, 111(9):1289–1295, June 2010. ISSN 0022-4073. doi: 10.1016/j.jqsrt.2010.01.036.
- T. Corpetti, E. Memin, and P. Perez. Dense estimation of fluid flows. *IEEE Transactions on Pattern Analysis and Machine Intelligence*, 24(3):365–380, Mar. 2002. ISSN 0162-8828. doi: 10.1109/34.990137.
- M. P. Dalton, I. M. Watson, P. A. Nadeau, C. Werner, W. Morrow, and J. M. Shannon. Assessment of the UV camera sulfur dioxide retrieval for point source plumes. *Journal of Volcanology and Geothermal Research*, 188(4):358–366, Dec. 2009. ISSN 0377-0273. doi: 10.1016/j.jvolgeores.2009.09.013.
- A. G. Davies, J. Calkins, L. Scharenbroich, R. G. Vaughan, R. Wright, P. Kyle, R. Castano, S. Chien, and D. Tran. Multi-instrument remote and in situ observations of the Erebus Volcano (Antarctica) lava lake in 2005: A comparison with the Pele lava lake on the jovian moon Io. *Journal of Volcanology and Geothermal Research*, 177(3):705–724, Nov. 2008. ISSN 0377-0273. doi: 16/j.jvolgeores.2008.02.010.
- E. De Lauro, S. De Martino, M. Falanga, and M. Palo. Modelling the macroscopic behavior of Strombolian explosions at Erebus volcano. *Physics of the Earth and Planetary Interiors*, pages 174–186, 2009. ISSN 0031-9201. doi: 10.1016/j.pepi.2009.05.003.
- R. Dibble, P. Kyle, and C. Rowe. Video and seismic observations of Strombolian eruptions at Erebus volcano, Antarctica. *Journal of Volcanology and Geothermal Research*, 177(3):619–634, Nov. 2008. ISSN 0377-0273. doi: 10.1016/j.jvolgeores.2008.07.020.
- T. Divoux, E. Bertin, V. Vidal, and J. C. Géminard. Intermittent outgassing through a non-Newtonian fluid. *Physical Review E*, 79(5):56204, 2009.
- R. Dunn. *wxpython: wxwindows for python*. <http://www.wxpython.org>. 2003.

- M. Edmonds, R. A. Herd, B. Galle, and C. M. Oppenheimer. Automated, high time-resolution measurements of SO₂ flux at Soufrière Hills Volcano, Montserrat. *Bulletin of Volcanology*, 65(8):578–586, Nov. 2003. ISSN 0258-8900, 1432-0819. doi: 10.1007/s00445-003-0286-x.
- G. Farneböck. Two-Frame Motion Estimation Based on Polynomial Expansion. In J. Bigun and T. Gustavsson, editors, *Image Analysis*, number 2749 in Lecture Notes in Computer Science, pages 363–370. Springer Berlin Heidelberg, Jan. 2003. ISBN 978-3-540-40601-3, 978-3-540-45103-7. URL http://link.springer.com/chapter/10.1007/3-540-45103-X_50.
- P. Francis, C. Oppenheimer, and D. Stevenson. Endogenous growth of persistently active volcanoes. *Nature*, 366(6455):554–557, Dec. 1993. doi: 10.1038/366554a0.
- B. Galle, C. Oppenheimer, A. Geyer, A. J. McGonigle, M. Edmonds, and L. Horrocks. A miniaturised ultraviolet spectrometer for remote sensing of SO₂ fluxes: a new tool for volcano surveillance. *Journal of Volcanology and Geothermal Research*, 119(1–4):241–254, Jan. 2003. ISSN 0377-0273. doi: 10.1016/S0377-0273(02)00356-6.
- A. Geiger, P. Lenz, C. Stiller, and R. Urtasun. The KITTI Vision Benchmark Suite, 2014. URL http://www.cvlibs.net/datasets/kitti/eval_stereo_flow.php?benchmark=flow.
- A. Gerst, M. Hort, R. C. Aster, J. B. Johnson, and P. R. Kyle. The first second of volcanic eruptions from the Erebus volcano lava lake, Antarctica - energies, pressures, seismology, and infrasound. *Journal of Geophysical Research: Solid Earth*, 118(7):3318–3340, 2013. ISSN 2169-9356. doi: 10.1002/jgrb.50234.
- W. F. Giggenbach, P. R. Kyle, and G. L. Lyon. Present volcanic activity on Mount Erebus, Ross Island, Antarctica. *Geology*, 1(3):135–136, Nov. 1973.
- Gnome. GNOME Office / Gnumeric - Welcome to Gnumeric!, 2013. URL <https://projects.gnome.org/gnumeric/>.
- R. Hegger and H. Kantz. Improved false nearest neighbor method to detect determinism in time series data. *Physical Review E*, 60(4):4970–4973, Oct. 1999. doi: 10.1103/PhysRevE.60.4970.
- R. Hegger, H. Kantz, and T. Schreiber. Practical implementation of nonlinear time series methods: The TISEAN package. arXiv e-print [chao-dyn/9810005](https://arxiv.org/abs/chao-dyn/9810005), Sept. 1998. URL <http://arxiv.org/abs/chao-dyn/9810005>. CHAOS 9 (1999) 413.

- M. Herzog and H.-F. Graf. Applying the three-dimensional model ATHAM to volcanic plumes: Dynamic of large co-ignimbrite eruptions and associated injection heights for volcanic gases. *Geophysical Research Letters*, 37(19):L19807, Oct. 2010. ISSN 1944-8007. doi: 10.1029/2010GL044986.
- M. Herzog, H.-F. Graf, C. Textor, and J. M. Oberhuber. The effect of phase changes of water on the development of volcanic plumes. *Journal of Volcanology and Geothermal Research*, 87(1–4):55–74, Dec. 1998. ISSN 0377-0273. doi: 10.1016/S0377-0273(98)00100-0.
- M. Herzog, J. M. Oberhuber, and H.-F. Graf. A Prognostic Turbulence Scheme for the Nonhydrostatic Plume Model ATHAM. *Journal of the Atmospheric Sciences*, 60(22):2783–2796, Nov. 2003. ISSN 0022-4928, 1520-0469. doi: 10.1175/1520-0469(2003)060<2783:APTSFT>2.0.CO;2.
- A. P. Holland, I. M. Watson, J. C. Phillips, L. Caricchi, and M. P. Dalton. Degassing processes during lava dome growth: Insights from Santiaguito lava dome, Guatemala. *Journal of Volcanology and Geothermal Research*, 202(1–2):153–166, Apr. 2011. ISSN 0377-0273. doi: 10.1016/j.jvolgeores.2011.02.004.
- L. A. Horrocks, C. Oppenheimer, M. R. Burton, H. J. Duffell, N. M. Davies, N. A. Martin, and W. Bell. Open-path Fourier transform infrared spectroscopy of SO₂: An empirical error budget analysis, with implications for volcano monitoring. *Journal of Geophysical Research: Atmospheres*, 106(D21):27647–27659, Nov. 2001. ISSN 2156-2202. doi: 10.1029/2001JD000343.
- J. D. Hunter. Matplotlib: A 2D graphics environment. *Computing In Science & Engineering*, 9(3):90–95, 2007.
- H. E. Huppert and M. A. Hallworth. Bi-directional flows in constrained systems. *Journal of Fluid Mechanics*, 578(1):95–112, 2007. doi: 10.1017/S0022112007004661.
- K. Iacovino. *An unexpected journey: Experimental insights into magma and volatile transport beneath Erebus volcano, Antarctica*. Ph.d. thesis, University of Cambridge, 2014.
- K. Iacovino, N. Peters, and C. Oppenheimer. Toward a unified method for the quantification of volatiles in magmas via FTIR. Florence, Italy, 2013. doi: 10.1180/minmag.2013.077.5.9. URL www.minersoc.org.

- K. Iacovino, C. Oppenheimer, B. Scaillet, and P. Kyle. Erebus volcano as an archetype for CO₂-dominated rift volcanism: Experimental constraints on the magma plumbing of Ross Island, Antarctic. *Journal of Petrology (in review)*, 2014.
- T. Ilanko, C. Oppenheimer, A. Burgisser, and P. Kyle. Cyclic degassing of Erebus volcano, Antarctica. *Bulletin of Volcanology (in review)*, 2014.
- M. R. James, H. Pinkerton, and S. Robson. Image-based measurement of flux variation in distal regions of active lava flows. *Geochemistry, Geophysics, Geosystems*, 8(3):Q03006, Mar. 2007. ISSN 1525-2027. doi: 10.1029/2006GC001448.
- E. Jones, T. Oliphant, and P. Peterson. SciPy: open source scientific tools for Python, 2001. URL <http://www.scipy.org/>.
- K. R. Jones, J. B. Johnson, R. Aster, P. R. Kyle, and W. McIntosh. Infrasonic tracking of large bubble bursts and ash venting at Erebus volcano, Antarctica. *Journal of Volcanology and Geothermal Research*, 177(3):661–672, Nov. 2008. ISSN 0377-0273. doi: 10.1016/j.jvolgeores.2008.02.001.
- L. Jones. *Terrestrial Laser Scanning (TLS) Observations of Erebus Volcano, Antarctica: Insights into the Near-Surface Magmatic System*. MSc thesis, New Mexico Institute of Mining and Technology, 2013. URL http://www.ees.nmt.edu/outside/alumni/papers/2013t_jones_lk.pdf.
- L. K. Jones, P. R. KYLE, J. Frechette, M. H. Okal, and C. Oppenheimer. Terrestrial Laser Scanning observations of geomorphic changes and lava lake levels at Erebus volcano, Antarctica. *Journal of Volcanology and Geothermal Research (in review)*, 2014.
- H. Kantz and T. Schreiber. *Nonlinear Time Series Analysis*. Cambridge University Press, 2nd edition, Nov. 2003. ISBN 0521529026.
- E. P. Kantzas, A. McGonigle, G. Tamburello, A. Aiuppa, and R. G. Bryant. Protocols for UV camera volcanic SO₂ measurements. *Journal of Volcanology and Geothermal Research*, 194(1–3):55–60, July 2010. ISSN 0377-0273. doi: 10.1016/j.jvolgeores.2010.05.003.
- P. J. Kelly, P. R. Kyle, N. W. Dunbar, and K. W. Sims. Geochemistry and mineralogy of the phonolite lava lake, Erebus volcano, Antarctica: 1972-2004 and comparison with older lavas. *Journal of Volcanology and Geothermal Research*, 177(3):589–605, Nov. 2008. ISSN 0377-0273. doi: 10.1016/j.jvolgeores.2007.11.025.

- M. B. Kennel, R. Brown, and H. D. I. Abarbanel. Determining embedding dimension for phase-space reconstruction using a geometrical construction. *Physical Review A*, 45(6):3403–3411, Mar. 1992. doi: 10.1103/PhysRevA.45.3403.
- C. Kern, F. Kick, P. Lübcke, L. Vogel, M. Wöhrbach, and U. Platt. Theoretical description of functionality, applications, and limitations of SO₂ cameras for the remote sensing of volcanic plumes. *Atmospheric Measurement Techniques Discussions*, 3(1):531–578, Feb. 2010. ISSN 1867-8610. doi: 10.5194/amtd-3-531-2010.
- C. Kern, C. A. Werner, M. P. Doukas, T. Elias, P. J. Kelly, and A. J. Sutton. Imaging volcanic SO₂ plumes with UV cameras. In *EGU General Assembly Conference Abstracts*, volume 14, page 12596, Vienna, Apr. 2012. EGU. URL <http://adsabs.harvard.edu/abs/2012EGUGA...1412596K>.
- C. Kern, C. Werner, T. Elias, A. J. Sutton, and P. Lübcke. Applying UV cameras for SO₂ detection to distant or optically thick volcanic plumes. *Journal of Volcanology and Geothermal Research*, 262:80–89, July 2013. ISSN 0377-0273. doi: 10.1016/j.jvolgeores.2013.06.009.
- N. Kingsbury. Complex wavelets for shift invariant analysis and filtering of signals. *Applied and Computational Harmonic Analysis*, 10(3):234–253, 2001. ISSN 1063-5203. doi: DOI:10.1006/acha.2000.0343.
- H. Knox. *Eruptive characteristics and glacial earthquake investigation on Erebus volcano, Antarctica*. Ph.d. thesis, New Mexico Institute of Mining and Technology, 2012. URL <http://www.ees.nmt.edu/outside/alumni/thesis.php>.
- S. G. Kraus. *DOASIS, A Framework Design for DOAS*. Ph.d. thesis, University of Mannheim, 2006.
- P. R. Kyle, K. Meeker, and D. Finnegan. Emission rates of sulfur dioxide, trace gases and metals from Mount Erebus, Antarctica. *Geophysical Research Letters*, 17(12):PP. 2125–2128, Nov. 1990. doi: 199010.1029/GL017i012p02125.
- A. La Spina, G. Salerno, and M. Burton. Recent SO₂ camera and OP-FTIR field measurements in Mexico and Guatemala. In *EGU General Assembly Conference Abstracts*, volume 15, page 10478, Apr. 2013. URL <http://adsabs.harvard.edu/abs/2013EGUGA...1510478L>.
- J. Lawrence, M. Ashley, and J. Storey. A remote, autonomous laboratory for Antarctica with hybrid power generation. *Aust. Journal Elec. Electronics Engineering*, 2(1):1–12, 2004.

- E. Lev, M. Spiegelman, R. J. Wysocki, and J. A. Karson. Investigating lava flow rheology using video analysis and numerical flow models. *Journal of Volcanology and Geothermal Research*, 247–248:62–73, Dec. 2012. ISSN 0377-0273. doi: 10.1016/j.jvolgeores.2012.08.002.
- P. Lübcke, N. Bobrowski, S. Illing, C. Kern, J. M. Alvarez Nieves, L. Vogel, J. Zielcke, H. Delgado Granados, and U. Platt. On the absolute calibration of SO₂ cameras. *Atmos. Meas. Tech.*, 6(3):677–696, Mar. 2013. ISSN 1867-8548. doi: 10.5194/amt-6-677-2013.
- J. Magarey and N. Kingsbury. Motion estimation using a complex-valued wavelet transform. *Signal Processing, IEEE Transactions on*, 46(4):1069–1084, Apr. 1998. ISSN 1053-587X. doi: 10.1109/78.668557.
- T. Mather, A. Allen, B. Davison, D. Pyle, C. Oppenheimer, and A. McGonigle. Nitric acid from volcanoes. *Earth and Planetary Science Letters*, 218(1–2):17–30, Jan. 2004a. ISSN 0012-821X. doi: 10.1016/S0012-821X(03)00640-X.
- T. A. Mather, V. I. Tsanev, D. M. Pyle, A. J. S. McGonigle, C. Oppenheimer, and A. G. Allen. Characterization and evolution of tropospheric plumes from Lascar and Villarrica volcanoes, Chile. *Journal of Geophysical Research: Atmospheres*, 109(D21):n/a–n/a, 2004b. ISSN 2156-2202. doi: 10.1029/2004JD004934.
- A. J. McGonigle. Measurement of volcanic SO₂ fluxes with differential optical absorption spectroscopy. *Journal of Volcanology and Geothermal Research*, 162(3–4): 111–122, May 2007. ISSN 0377-0273. doi: 10.1016/j.jvolgeores.2007.02.001.
- A. J. S. McGonigle. Walking traverse and scanning DOAS measurements of volcanic gas emission rates. *Geophysical Research Letters*, 29(20), 2002. ISSN 0094-8276. doi: 10.1029/2002GL015827.
- A. J. S. McGonigle, S. Inguaggiato, A. Aiuppa, A. R. Hayes, and C. Oppenheimer. Accurate measurement of volcanic SO₂ flux: Determination of plume transport speed and integrated SO₂ concentration with a single device. *Geochemistry, Geophysics, Geosystems*, 6(2):n/a–n/a, 2005. ISSN 1525-2027. doi: 10.1029/2004GC000845.
- A. J. S. McGonigle, A. Aiuppa, M. Ripepe, E. P. Kantzas, and G. Tamburello. Spectroscopic capture of 1 Hz volcanic SO₂ fluxes and integration with volcano geophysical data. *Geophysical Research Letters*, 36(21):n/a–n/a, 2009. ISSN 1944-8007. doi: 10.1029/2009GL040494.

- I. Molina, A. Burgisser, and C. Oppenheimer. Numerical simulations of convection in crystal-bearing magmas: A case study of the magmatic system at Erebus, Antarctica. *Journal of Geophysical Research: Solid Earth*, 117(B7), 2012. ISSN 2156-2202. doi: 10.1029/2011JB008760.
- T. Mori and M. Burton. The SO₂ camera: A simple, fast and cheap method for ground-based imaging of SO₂ in volcanic plumes. *Geophysical Research Letters*, 33(24):L24804, Dec. 2006. ISSN 0094-8276. doi: 10.1029/2006GL027916.
- T. Mori and M. Burton. Quantification of the gas mass emitted during single explosions on Stromboli with the SO₂ imaging camera. *Journal of Volcanology and Geothermal Research*, 188(4):395–400, Dec. 2009. ISSN 0377-0273. doi: 10.1016/j.jvolgeores.2009.10.005.
- Y. Moussallam, C. Oppenheimer, A. Aiuppa, G. Giudice, M. Moussallam, and P. Kyle. Hydrogen emissions from Erebus volcano, Antarctica. *Bulletin of Volcanology*, 74(9):2109–2120, Aug. 2012. ISSN 0258-8900, 1432-0819. doi: 10.1007/s00445-012-0649-2.
- Y. Moussallam, C. Oppenheimer, B. Scaillet, F. Gaillard, P. Kyle, N. Peters, M. Hartley, K. Berlo, and A. Donovan. Tracking the changing oxidation state of Erebus magmas, from mantle to surface, driven by magma ascent and degassing. *Earth and Planetary Science Letters*, 393:200–209, May 2014a. ISSN 0012-821X. doi: 10.1016/j.epsl.2014.02.055.
- Y. Moussallam, N. Peters, C. Ramírez, C. Oppenheimer, A. Aiuppa, and G. Giudice. Characterisation of the magmatic signature in gas emissions from Turrialba volcano, Costa Rica. *Solid Earth Discussions*, 6(2):2293–2320, Aug. 2014b. ISSN 1869-9537. doi: 10.5194/sed-6-2293-2014.
- P. A. Nadeau, J. L. Palma, and G. P. Waite. Linking volcanic tremor, degassing, and eruption dynamics via SO₂ imaging. *Geophysical Research Letters*, 38(1): L01304, Jan. 2011. ISSN 0094-8276. doi: 10.1029/2010GL045820.
- J. M. Oberhuber, M. Herzog, H.-F. Graf, and K. Schwanke. Volcanic plume simulation on large scales. *Journal of Volcanology and Geothermal Research*, 87(1–4): 29–53, Dec. 1998. ISSN 0377-0273. doi: 10.1016/S0377-0273(98)00099-7.
- C. Oppenheimer and P. R. Kyle. Probing the magma plumbing of Erebus volcano, Antarctica, by open-path FTIR spectroscopy of gas emissions. *Journal of Volcanology and Geothermal Research*, 177(3):743–754, Nov. 2008. ISSN 0377-0273. doi: 10.1016/j.jvolgeores.2007.08.022.

- C. Oppenheimer, A. J. S. McGonigle, P. Allard, M. J. Wooster, and V. Tsanev. Sulfur, heat, and magma budget of Erta 'Ale lava lake, Ethiopia. *Geology*, 32(6): 509–512, Jan. 2004. ISSN 0091-7613, 1943-2682. doi: 10.1130/G20281.1.
- C. Oppenheimer, A. S. Lomakina, P. R. Kyle, N. G. Kingsbury, and M. Boichu. Pulsatory magma supply to a phonolite lava lake. *Earth and Planetary Science Letters*, 284(3-4):392–398, 2009. ISSN 0012-821X. doi: 10.1016/j.epsl.2009.04.043.
- C. Oppenheimer, R. Moretti, P. R. Kyle, A. Eschenbacher, J. B. Lowenstern, R. L. Hervig, and N. W. Dunbar. Mantle to surface degassing of alkalic magmas at Erebus volcano, Antarctica. *Earth and Planetary Science Letters*, 306(3–4):261–271, June 2011. ISSN 0012-821X. doi: 10.1016/j.epsl.2011.04.005.
- T. R. Orr and J. C. Rea. Time-lapse camera observations of gas piston activity at Pu'u 'Ō'ō, Kīlauea volcano, Hawai'i. *Bulletin of Volcanology*, 74(10):2353–2362, Oct. 2012. ISSN 0258-8900, 1432-0819. doi: 10.1007/s00445-012-0667-0.
- E. Pacaud. Aravis - GNOME Live!, Jan. 2011. URL <http://live.gnome.org/Aravis>.
- M. R. Patrick, T. Orr, D. Wilson, D. Dow, and R. Freeman. Cyclic spattering, seismic tremor, and surface fluctuation within a perched lava channel, Kīlauea Volcano. *Bulletin of Volcanology*, 73(6):639–653, Aug. 2011. ISSN 0258-8900, 1432-0819. doi: 10.1007/s00445-010-0431-2.
- M. R. Patrick, T. Orr, L. Antolik, L. Lee, and K. Kamibayashi. Continuous monitoring of Hawaiian volcanoes with thermal cameras. *Journal of Applied Volcanology*, 3(1):1, 2014. ISSN 2191-5040. doi: 10.1186/2191-5040-3-1.
- T. D. Pering, G. Tamburello, A. J. S. McGonigle, A. Aiuppa, A. Cannata, G. Giudice, and D. Patanè. High time resolution fluctuations in volcanic carbon dioxide degassing from Mount Etna. *Journal of Volcanology and Geothermal Research*, 270:115–121, Jan. 2014. ISSN 0377-0273. doi: 10.1016/j.jvolgeores.2013.11.014.
- N. Peters. AvoPlot: An extensible scientific plotting tool based on matplotlib. *Journal of Open Research Software*, 2(1), Feb. 2014. ISSN 2049-9647. doi: 10.5334/jors.ai.
- N. Peters, A. Hoffmann, T. Barnie, M. Herzog, and C. Oppenheimer. Use of motion estimation algorithms for improved flux measurements using SO₂ cameras. *Journal of Volcanology and Geothermal Research*, 2014a. ISSN 0377-0273. doi: 10.1016/j.jvolgeores.2014.08.031.

- N. Peters, C. Oppenheimer, D. R. Killingsworth, J. Frechette, and P. Kyle. Correlation of cycles in Lava Lake motion and degassing at Erebus Volcano, Antarctica. *Geochemistry, Geophysics, Geosystems*, 15(8):3244–3257, Aug. 2014b. ISSN 15252027. doi: 10.1002/2014GC005399.
- N. Peters, C. Oppenheimer, and P. Kyle. Autonomous thermal camera system for monitoring the active lava lake at Erebus volcano, Antarctica. *Geoscientific Instrumentation, Methods and Data Systems*, 3(1):13–20, Feb. 2014c. ISSN 2193-0864. doi: 10.5194/gi-3-13-2014.
- N. Peters, C. Oppenheimer, P. Kyle, and N. Kingsbury. Decadal persistence of cycles in lava lake motion at Erebus volcano, Antarctica. *Earth and Planetary Science Letters*, 395:1–12, June 2014d. ISSN 0012-821X. doi: 10.1016/j.epsl.2014.03.032.
- U. Platt and J. Stutz. Differential Absorption Spectroscopy. In *Differential Optical Absorption Spectroscopy*, pages 135–174. Springer Berlin Heidelberg, Berlin, Heidelberg, 2008. ISBN 978-3-540-21193-8, 978-3-540-75776-4. URL http://link.springer.com/content/pdf/10.1007/978-3-540-75776-4_6.
- R. Polikar. The Wavelet Tutorial, Oct. 2010. URL <http://users.rowan.edu/~polikar/WAVELETS/WTtutorial.html>.
- N. Rappin and R. Dunn. *wxPython In Action*. Manning Publication Co., 2006.
- M. Richter and T. Schreiber. Phase space embedding of electrocardiograms. *Physical Review E*, 58(5):6392–6398, Nov. 1998. doi: 10.1103/PhysRevE.58.6392.
- M. Ripepe, A. J. L. Harris, and R. Carniel. Thermal, seismic and infrasonic evidences of variable degassing rates at Stromboli volcano. *Journal of Volcanology and Geothermal Research*, 118(3–4):285–297, Nov. 2002. ISSN 0377-0273. doi: 10.1016/S0377-0273(02)00298-6.
- G. Salerno, M. Burton, C. Oppenheimer, T. Caltabiano, D. Randazzo, N. Bruno, and V. Longo. Three-years of SO₂ flux measurements of Mt. Etna using an automated UV scanner array: Comparison with conventional traverses and uncertainties in flux retrieval. *Journal of Volcanology and Geothermal Research*, 183(1–2):76–83, May 2009. ISSN 0377-0273. doi: 10.1016/j.jvolgeores.2009.02.013.
- J. Sanders. *Veusz - A Scientific Plotting Package*, 2013. URL <http://home.gna.org/veusz/>.

- G. Sawyer, G. Salerno, J. Le Blond, R. Martin, L. Spampinato, T. Roberts, T. Mather, M. Witt, V. Tsanev, and C. Oppenheimer. Gas and aerosol emissions from Villarrica volcano, Chile. *Journal of Volcanology and Geothermal Research*, 203(1–2):62–75, June 2011. ISSN 0377-0273. doi: 10.1016/j.jvolgeores.2011.04.003.
- G. M. Sawyer and M. R. Burton. Effects of a volcanic plume on thermal imaging data. *Geophysical Research Letters*, 33:4 PP., July 2006. doi: 200610.1029/2005GL025320.
- T. Schreiber and A. Schmitz. Surrogate time series. arXiv e-print chao-dyn/9909037, Sept. 1999. URL <http://arxiv.org/abs/chao-dyn/9909037>. *Physica D* 142 (2000) 346-382.
- H. Shinohara. A new technique to estimate volcanic gas composition: plume measurements with a portable multi-sensor system. *Journal of Volcanology and Geothermal Research*, 143(4):319–333, May 2005. ISSN 0377-0273. doi: 10.1016/j.jvolgeores.2004.12.004.
- H. Shinohara and J. B. Witter. Volcanic gases emitted during mild Strombolian activity of Villarrica volcano, Chile. *Geophysical Research Letters*, 32(20):n/a–n/a, 2005. ISSN 1944-8007. doi: 10.1029/2005GL024131.
- J. Smekens, M. R. Burton, A. B. Clarke, A. Harijoko, H. Wibowo, and G. Sawyer. High frequency SO₂ flux measurements at Semeru volcano, Indonesia, using the SO₂ camera. *AGU Fall Meeting Abstracts*, -1:2882, Dec. 2013.
- L. Spampinato, S. Calvari, C. Oppenheimer, and E. Boschi. Volcano surveillance using infrared cameras. *Earth-Science Reviews*, 106(1–2):63–91, May 2011. ISSN 0012-8252. doi: 10.1016/j.earscirev.2011.01.003.
- D. Sweeney, P. R. Kyle, and C. Oppenheimer. Sulfur dioxide emissions and degassing behavior of Erebus volcano, Antarctica. *Journal of Volcanology and Geothermal Research*, 177(3):725–733, Nov. 2008. ISSN 0377-0273. doi: 10.1016/j.jvolgeores.2008.01.024.
- G. Tamburello, E. Kantzas, A. McGonigle, A. Aiuppa, and G. Giudice. UV camera measurements of fumarole field degassing (La Fossa crater, Vulcano Island). *Journal of Volcanology and Geothermal Research*, 199(1–2):47–52, Jan. 2011. ISSN 0377-0273. doi: 10.1016/j.jvolgeores.2010.10.004.

- G. Tamburello, A. Aiuppa, E. Kantzas, A. McGonigle, and M. Ripepe. Passive vs. active degassing modes at an open-vent volcano (Stromboli, Italy). *Earth and Planetary Science Letters*, 359–360:106–116, Dec. 2012. ISSN 0012-821X. doi: 10.1016/j.epsl.2012.09.050.
- G. Tamburello, A. Aiuppa, A. J. S. McGonigle, P. Allard, A. Cannata, G. Giudice, E. P. Kantzas, and T. D. Pering. Periodic volcanic degassing behavior: The Mount Etna example. *Geophysical Research Letters*, 40(18):4818–4822, 2013. ISSN 1944-8007. doi: 10.1002/grl.50924.
- H. Tazieff. Permanent lava lakes: observed facts and induced mechanisms. *Journal of Volcanology and Geothermal Research*, 63(1–2):3–11, Oct. 1994. ISSN 0377-0273. doi: 10.1016/0377-0273(94)90015-9.
- C. Textor, H. F. Graf, M. Herzog, J. M. Oberhuber, W. I. Rose, and G. G. J. Ernst. Volcanic particle aggregation in explosive eruption columns. Part II: Numerical experiments. *Journal of Volcanology and Geothermal Research*, 150(4):378–394, Feb. 2006a. ISSN 0377-0273. doi: 10.1016/j.jvolgeores.2005.09.008.
- C. Textor, H. F. Graf, M. Herzog, J. M. Oberhuber, W. I. Rose, and G. G. J. Ernst. Volcanic particle aggregation in explosive eruption columns. Part I: Parameterization of the microphysics of hydrometeors and ash. *Journal of Volcanology and Geothermal Research*, 150(4):359–377, Feb. 2006b. ISSN 0377-0273. doi: 10.1016/j.jvolgeores.2005.09.007.
- R. I. Tilling. Fluctuations in surface height of active lava lakes during 1972–1974 Mauna Ulu Eruption, Kilauea Volcano, Hawaii. *Journal of Geophysical Research: Solid Earth*, 92(B13):13721–13730, 1987. ISSN 2156-2202. doi: 10.1029/JB092iB13p13721.
- A. R. Van Eaton, M. Herzog, C. J. N. Wilson, and J. McGregor. Ascent dynamics of large phreatomagmatic eruption clouds: The role of microphysics. *Journal of Geophysical Research: Solid Earth*, 117(B3):B03203, Mar. 2012. ISSN 2156-2202. doi: 10.1029/2011JB008892.
- G. van Rossum. Python, 2013. URL <http://www.python.org>.
- A. C. Vandaele, P. C. Simon, J. M. Guilmot, M. Carleer, and R. Colin. SO₂ absorption cross section measurement in the UV using a Fourier transform spectrometer. *Journal of Geophysical Research: Atmospheres*, 99(D12):25599–25605, 1994. ISSN 2156-2202. doi: 10.1029/94JD02187.

- G. Ward and A. Baxter. Distributing Python Modules — Python v2.7.5 documentation, 2013. URL <http://docs.python.org/2/distutils/>.
- F. Witham and E. W. Llewelin. Stability of lava lakes. *Journal of Volcanology and Geothermal Research*, 158(3-4):321–332, Nov. 2006. ISSN 0377-0273. doi: 10.1016/j.jvolgeores.2006.07.004.
- F. Witham, A. W. Woods, and C. Gladstone. An analogue experimental model of depth fluctuations in lava lakes. *Bulletin of Volcanology*, 69(1):51–56, Apr. 2006. ISSN 0258-8900. doi: 10.1007/s00445-006-0055-8.
- J. B. Witter, V. C. Kress, P. Delmelle, and J. Stix. Volatile degassing, petrology, and magma dynamics of the Villarrica Lava Lake, Southern Chile. *Journal of Volcanology and Geothermal Research*, 134(4):303–337, July 2004. ISSN 0377-0273. doi: 10.1016/j.jvolgeores.2004.03.002.
- R. Wright and E. Pilger. Satellite observations reveal little inter-annual variability in the radiant flux from the Mount Erebus lava lake. *Journal of Volcanology and Geothermal Research*, 177(3):687–694, Nov. 2008. ISSN 0377-0273. doi: 10.1016/j.jvolgeores.2008.03.005.
- T. Wright. Vispect, 2008. URL <http://vispect.sourceforge.net/>.
- D. Zandomenighi, R. Aster, P. Kyle, A. Barclay, J. Chaput, and H. Knox. Internal structure of Erebus volcano, Antarctica imaged by high-resolution active-source seismic tomography and coda interferometry. *Journal of Geophysical Research: Solid Earth*, 118(3):1067–1078, 2013. ISSN 2169-9356. doi: 10.1002/jgrb.50073.